Modelling and stabilization of coil deposition in intracranial aneurysm treatment

J.P.T. van der Staaij

Master of Science Thesis

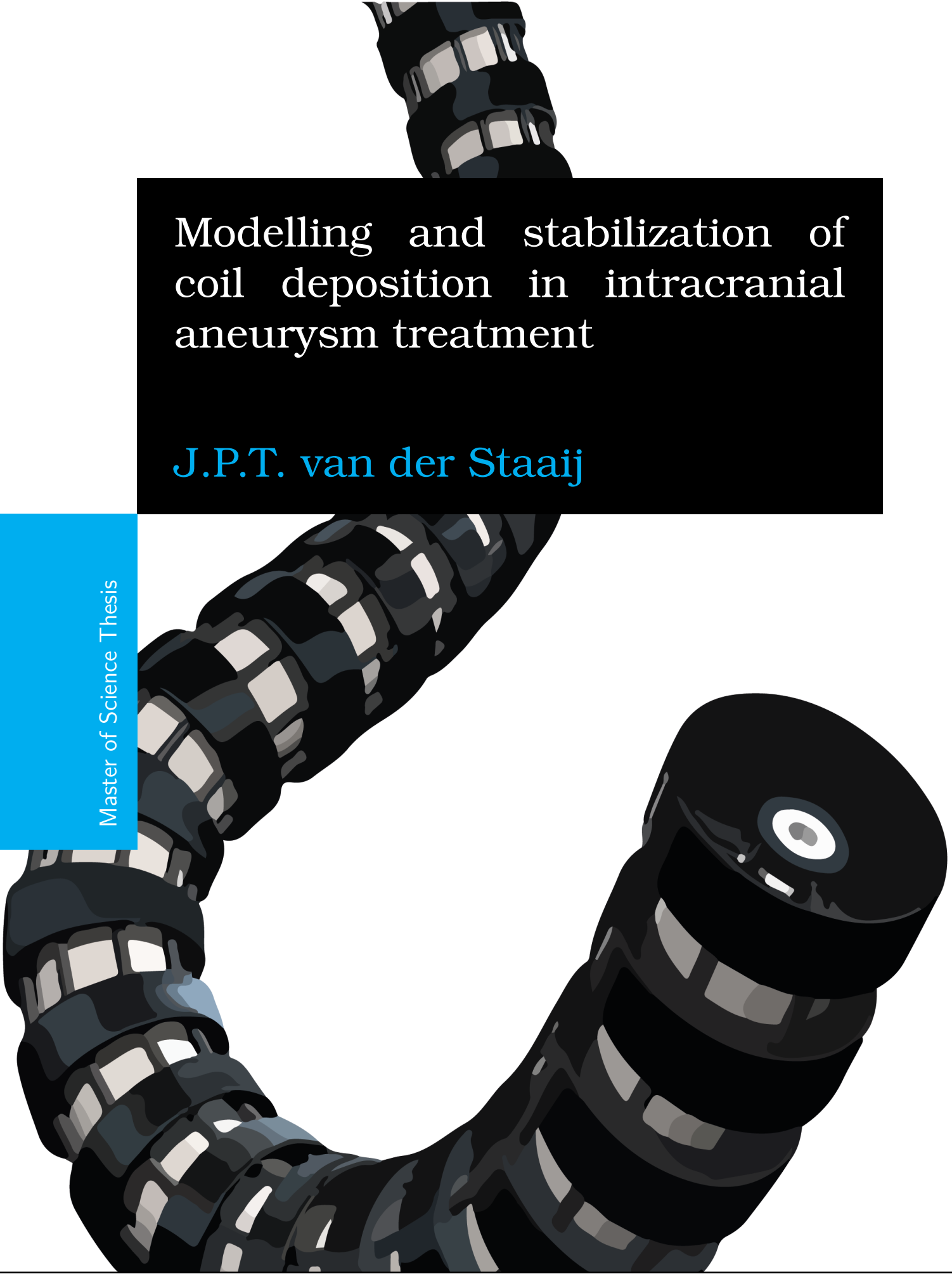

TU Delft Delft University of Technology

Cognitive Robotics
Delft Center for Systems and Control

Modelling and stabilization of coil deposition in intracranial aneurysm treatment

Master of Science Thesis

For the degree of Master of Science in Systems and Control and Master of Science in Robotics at Delft University of Technology

J.P.T. van der Staaij

December 1, 2022

Faculty of Mechanical, Maritime and Materials Engineering (3mE) · Delft University of Technology

Delft University of Technology
Department of
Delft Center for Systems and Control (dcsc)

The undersigned hereby certify that they have read and recommend to the Faculty of Mechanical, Maritime and Materials Engineering (3mE) for acceptance a thesis entitled

Modelling and stabilization of coil deposition in intracranial aneurysm treatment

by

J.P.T. van der Staaij

in partial fulfillment of the requirements for the degree of

Master of Science Systems and Control.

Dated: December 1, 2022

Supervisors:

Dr.ir. M. Jafarian

Dr.ir. A. Sakes

Readers:

Dr.ir. T. van den Boom

Dr.ir. C. Della Santina

Dr.ir. J.C.F. de Winter

Delft University of Technology
Department of
Cognitive Robotics (cor)

The undersigned hereby certify that they have read and recommend to the Faculty of Mechanical, Maritime and Materials Engineering (3mE) for acceptance a thesis entitled

Modelling and stabilization of coil deposition in intracranial aneurysm treatment

by

J.P.T. van der Staaij

in partial fulfillment of the requirements for the degree of

Master of Science Robotics.

Dated: December 1, 2022

Supervisors:

Dr.ir. M. Jafarian

Dr.ir. A. Sakes

Readers:

Dr.ir. T. van den Boom

Dr.ir. C. Della Santina

Dr.ir. J.C.F. de Winter

Abstract

An Intracranial Aneurysm (IA) is a bulge in the cerebral vasculature. The rupture of an aneurysm results in a brain bleed. As a consequence, most patients become severely handicapped or may even die. Preventive treatment with endovascular coiling is controversial due to the high risk of complications. These complications are partly caused by the current uncontrolled delivery of coils to the aneurysm. While recent developments in microcatheter design allow for improved positioning, no method has been devised to model and control the tension applied by the coil on the aneurysm wall throughout a coiling procedure. This thesis aims to come up with a method to improve the safety of aneurysm treatment.

This thesis presents a new way to dynamically model an endovascular coil and its interaction with a microcatheter and the aneurysm wall throughout a coil deployment procedure. The main advantage of this model is its low computational complexity allowing real-time control computation. A control architecture is presented that enables regulation of the contact force between the coil and the aneurysm wall while obeying the constraints imposed by the equipment and the environment. The presented architecture comprises an augmented energy-shaping controller working in parallel with a constraint preservation controller.

This thesis shows that this control architecture asymptotically stabilizes the aneurysm wall tension at the desired value throughout the coil deployment procedure.

This work provides a basis for modelling and control in future experimental validations. Therefore, this work is a promising first step in the modelling and control of robotic systems for neurovascular interventions and a step forward in the preventive treatment of intracranial aneurysms.

Table of Contents

Acknowledgements

The writing of this Master's thesis would not have been so easy without the help from so many directions. I would like to thank my supervisor Matin for the long discussions where she pushed me to truncate the problem and focus on the explainability of my work. I also want to thank my supervisor Aimée who underscored the importance of preserving the link between my simulations and the actual medical intervention. I would like to thank interventional cardiologist Robbert de Winter and his team from the Amsterdam University Medical Center for discussing the current problems in minimally invasive heart surgery. Moreover, I want to thank Pieter Jan van Doormaal for facilitating the discussion on intracranial aneurysm treatment with experts from the Erasmus University Medical Center (Erasmus MC). I want to thank neurologist Bob Roozenbeek (Erasmus MC) for pointing out the importance of wider preventive treatment for intracranial aneurysms and I want to thank interventional neuroradiologist Pieter Jan van Doormaal (Erasmus MC) for providing a deeper insight into the complications mechanisms related to endovascular coiling procedures. I also want to thank Bram and Ruben for the many coffee breaks which were relaxing while sometimes leading to new insights in my thesis and I want to thank Niels for his support and the design of the thesis cover. Lastly, I want to thank Julia for supporting me throughout this thesis, believing in me, and always improving my work.

Delft, University of Technology — J.P.T. van der Staaij
December 1, 2022

"You will always regret your last coil."

— *Pieter Jan van Doormaal*, interventional neuroradiologist

Erasmus University Medical Center, Rotterdam, The Netherlands

Chapter 1

Introduction

This thesis aims to reduce the risk of complications in intracranial aneurysm treatment by stabilizing coil deposition of a soft steerable catheter. This chapter starts by giving a clinical background on intracranial aneurysms. This background, in combination with expert clinical opinion from the Erasmus University Medical Center (Erasmus MC) and recent advances in the design of medical devices [1], forms the motivation for this thesis. The thesis objective is synthesized in Section 1-3 and the main thesis contributions are underlined in Section 1-4.

1-1 Clinical background

This section provides a clinical background on intracranial aneurysms. This entails their preferred medical procedure, state-of-the-art medical devices and related periprocedural complications.

1-1-1 Intracranial aneurysms

An Intracranial Aneurysm (IA) is a localized bulge (3-10 mm) in the cerebral vasculature found in 3% of the worldwide adult population [2, 3]. While the cause is often unclear, high blood pressure and a weak vessel wall are risk factors for aneurysm formation [2]. In most cases (90%) the aneurysm resembles a sac-like outpouching in the blood vessel as illustrated in Figure 1-1b [4]. This outpouching is named the aneurysm dome or sac while the gateway to the neighbouring vessel is called the aneurysm neck. Aneurysms usually form at the bifurcation of two arteries where blood pressure on the vessel wall is at its maximum [5, 6]. Depending on size and location, aneurysms can result in neurological symptoms or headaches [2], however, their presentation is often asymptomatic. In those cases, the aneurysm is either accidentally found on a brain scan or detected only after rupture.

The rupture of an intracranial aneurysm results in a Subarachnoid Haemorrhage (SAH), i.e. brain bleed. Although only 0.25% of aneurysms rupture and bleed [2], the consequences of rupture are severe. It has been reported that 50% of patients do not survive an SAH and 25% of patients will be severely handicapped. Only a few patients continue life without physical

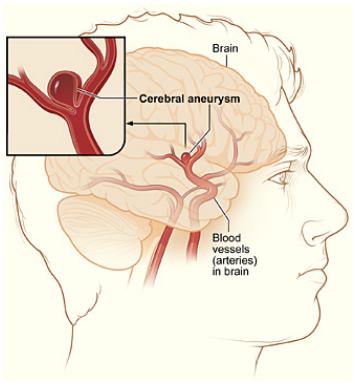

(a) Overview of a cerebral aneurysm from [7].

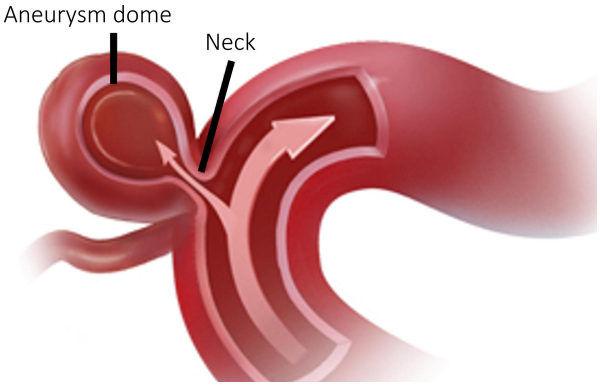

(b) Saccular aneurysm at bifurcation, edited from [8].

Figure 1-1: Illustration of an unruptured intracranial aneurysm.

consequences [9, 10]. When the haemorrhage is limited, the aneurysm can close autonomously due to thrombus formation at the bleeding site. However, this aneurysm is prone to rerupture within 30 days in 20% of the cases [9, 10]. Hence, medical procedures have been devised to reduce the risk of aneurysm (re)rupture.

Medical procedures for aneurysm treatment aim to block the blood flow to the aneurysm in order to induce thrombus formation within the aneurysm sac. Thereafter, fibrous tissue forms in the aneurysm sac causing the aneurysm to shrink within the months to follow [11, 12]. The two most frequently employed procedures, surgical clipping and endovascular coiling, are illustrated in Figure 1-2. During surgical clipping, a spring-like clip is permanently placed on the aneurysm neck through open surgery, while endovascular coiling comprises a minimally invasive procedure where the aneurysm is approached from more easily accessible blood vessels [8, 12]. Due to complex vasculature, some aneurysms can only be reached using an open surgical procedure. However, when endovascular coiling is feasible, the International Study of Unruptured Intracranial Aneurysms (ISUIA) has favoured coiling over clipping based on a complication rate of 7% for coiling compared to 21% for clipping [13]. Therefore, this thesis limits its scope to endovascular coiling procedures for intracranial aneurysm treatment.

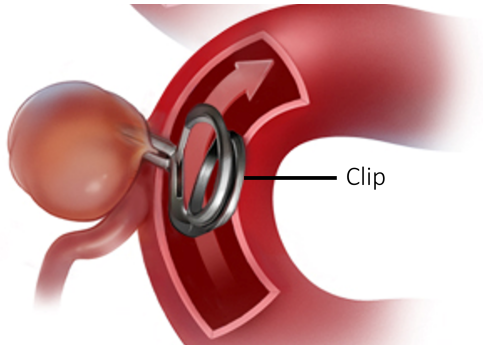

(a) Clipped aneurysm

(b) Coiled aneurysm

Figure 1-2: Illustration of the medical procedures for intracranial aneurysm treatment.

1-1-2 Endovascular coiling

Endovascular coiling or endovascular embolization is a minimally invasive procedure where a microcatheter is used to fill the aneurysm with platinum wires, i.e. coils. The deployment of multiple coils inside the aneurysm sac reduces the blood flow velocity and induces thrombus formation. The goal of the coiling procedure is to pack the coil mass densely and evenly into the aneurysm sac to achieve minimal residual blood flow [5].

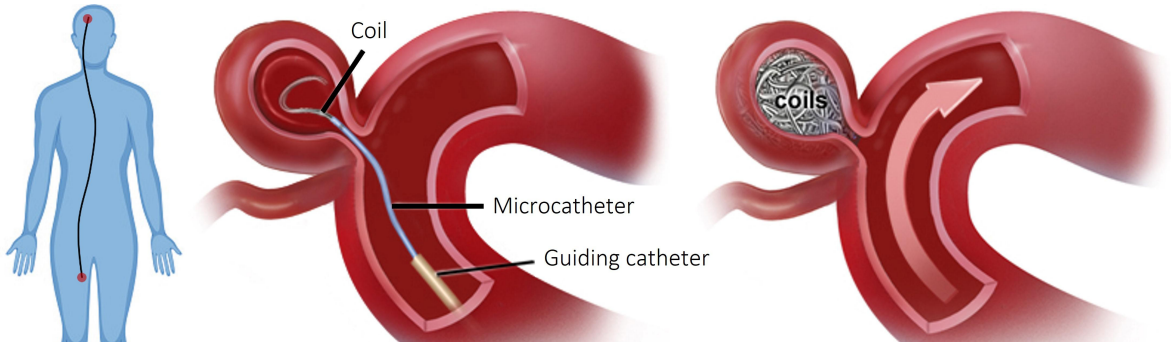

Figure 1-3: Illustration of a coiling procedure, edited from [8].

Coiling procedure

This paragraph describes the typical workflow of a coiling procedure. The interventional neuroradiologist (operator) accesses the patient's vasculature through the femoral artery in the groin as illustrated in Figure 1-3. A steerable guidewire, placed inside a microcatheter's lumen, is used to endovascularly navigate the microcatheter under X-ray guidance to the treatment site (Figure 1-4b). The simultaneous injection of contrast dye shows nearby vasculature, serving as a vascular roadmap, i.e. angiogram, for the operator. Upon reaching the aneurysm, the guidewire is removed from the microcatheter and replaced by a straightened platinum coil [10, 12]. As the coils reduce the blood flow in the aneurysm, the coil packing density can be inferred from the absence of contrast fluid on the angiogram. Hence, successful coiling of the aneurysm in Figure 1-4 makes it disappear on the post-coiling angiogram in Figure 1-4c [5].

(a) Pre-coiling angiogram of an unruptured intracranial aneurysm.

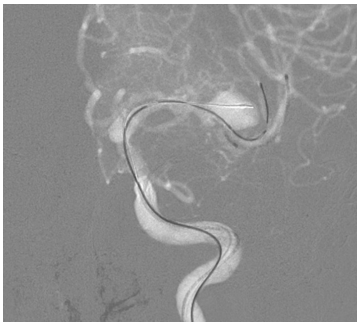

(b) Microcatheter navigated under X-ray guidance.

(c) Post-coiling angiogram showing blockage from blood flow to the aneurysm.

Figure 1-4: Medical imaging at different stages of a coiling procedure, edited from [5].

Coils are advanced in the catheter's inner lumen using a pushing mechanism attached to the coil. If desired, the operator can pull back the coil before detachment to put it in a better position [14]. Figure 1-5 shows an electrolytic detachment mechanism to release the coil from the pusher mechanism into the aneurysm. After deployment, retrieving the coil is nearly impossible [11].

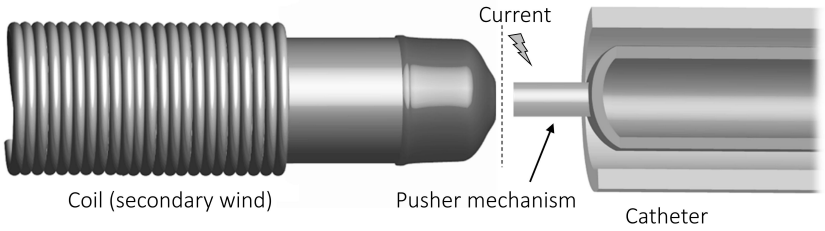

Figure 1-5: Electrolytic coil detachment mechanism, edited from [15].

Endovascular coils

The endovascular coil, illustrated in Figure 1-6, is composed of three structures. The primary structure is the platinum wire, i.e. stock wire, which has a diameter between 45-75 μm and mostly determines the coil's stiffness. The stock wire is wound around a metal rod into a second structure with a diameter between 250-380 μm [16]. This is what is called the coil and determines the diameter of the microcatheter's lumen. To maximize coil distribution and clot formation in the aneurysm sac, the coils are manufactured in a tertiary shape. Upon being deposited in the aneurysm sac, the coil will unravel and reform to its tertiary structure [16, 17]. Figure 1-7 shows commonly used tertiary coil structures, i.e spherically and helically

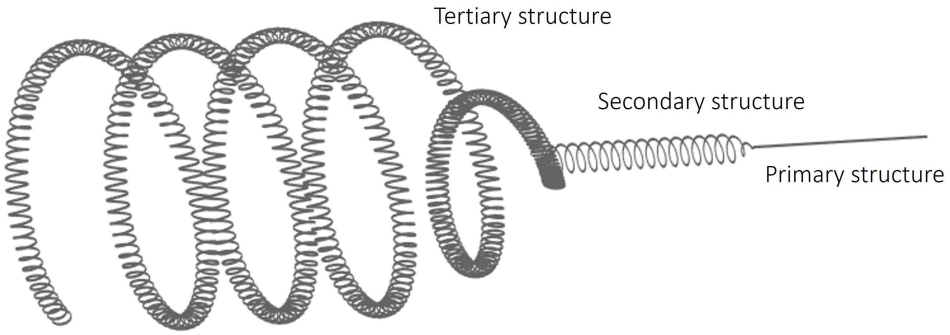

Figure 1-6: Endovascular coil structure for a helical coil.

shaped. The coil structure is picked to optimally fill the aneurysm. A larger framing coil (10-20 cm) is usually selected to support the aneurysm dome and cover the aneurysm neck to prevent future coils from easily moving out of the aneurysm. Then softer, smaller-sized filling coils (2-5 cm) are used for packing the internal volume of the aneurysm [5, 17, 18]. By straightening the coil, elastic potential energy is stored in the coil [17]. The tendency that the coil wants to return to its original structure is used to optimally fill the aneurysm. However, when such a coil cannot fully return to its tertiary structure it can apply significant pressure on the aneurysm wall as a result of its stored elastic energy.

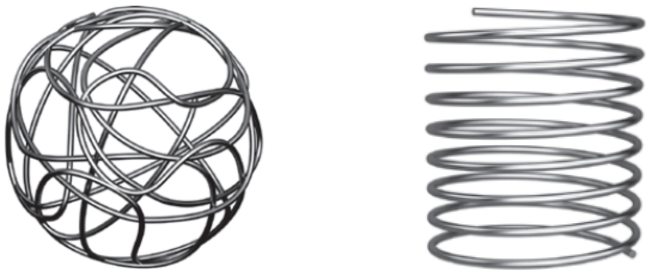

(a) Spherical coil **(b)** Helical coil

Figure 1-7: Commonly used tertiary structures for endovascular coils.

State-of-the-art microcatheters

Various microcatheters, with a diameter under 1 mm, have been designed for coiling procedures. The tip of such a microcatheter is steered using a guidewire. This enables navigation through the brain vasculature. A standard guide wire has a diameter of 0.014 inches (360μm) and is placed inside the catheter's lumen. Usually, these guide wires have a preshaped tip curve and are manually steered by rotating the wire around its longitudinal axis. Recent research by the Massachusetts Institute of Technology (MIT) [19] has presented the first telerobotically controlled magnetic guidewire for neurovascular interventions. This robotically steered guidewire allows for safer and quicker access to hard-to-reach aneurysms in the brain vasculature. However, this guidewire still needs to be removed from the catheter lumen to inject endovascular coils. Due to guidewire removal, the microcatheter loses its steerability, therefore complicating the accurate administration of coils to the target location [12, 1]. Recent research at the University of California San Diego (UCSD) by Gopesh et al. [1] has therefore presented the first soft robotic steerable microcatheter, specifically designed for the endovascular treatment of cerebral aneurysms. The proposed device is manually hydraulically steered via four saline-filled channels. Pressurizing one of the channels causes deflection of the tip in the opposite direction. Using this actuation mechanism, the operator can steer the microcatheter tip to the centre of the aneurysm dome with almost no time delay and can lock its orientation. An illustration of the steerable microcatheter tip has been depicted in figure Figure 1-8.

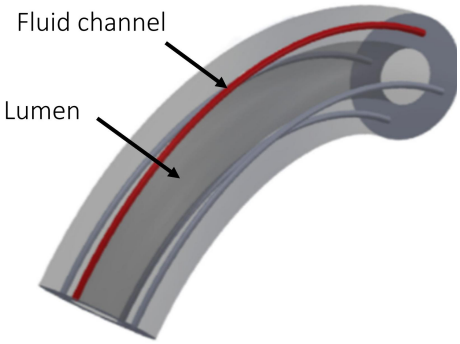

Figure 1-8: Hydraulically steered catheter tip designed at UCSD by Gopesh et al. [1].

Gopesh et al. [20] has mentioned in their research that this steerable device improves the dexterity of the catheter tip, enabling the operator to make a 180-degree turn from the parent

artery into the aneurysm without the catheter 'kicking' out of the aneurysm. Moreover, it has been presented that this catheter inhibits the waving catheter tip motion which disturbs the catheter tip position during coil deployment.

1-1-3 Periprocedural complications

While the treatment of a ruptured intracranial aneurysm is a matter of life and death, preventive treatment of Unruptured Intracranial Aneurysms (UIA) is controversial. A tradeoff has to be made between the risk of spontaneous rupture and the risk of procedural complications [2]. Treating all UIA is not cost-effective, nor clinically the best option [21]. Reducing intraprocedural complications would enable preventive treatment of UIA and therefore would reduce SAH incidence. To give an insight into the current challenges of the coiling procedure for intracranial aneurysm treatment, this section elaborates on periprocedural complications associated with endovascular coiling. Generally, two types of complications could occur during aneurysm treatment; Intraprocedural Aneurysm Rupture (IAR) and a Thromboembolic Event (TE).

Intraprocedural aneurysm ruptures (IARs)

An intraprocedural aneurysm rupture arises in 1-5% of endovascular procedures and increases the mortality risk by four times [22]. Endovascular procedures are either performed to prevent unruptured aneurysms from rupturing or to prevent rerupture of a previously ruptured aneurysm. IARs are more frequent in previously ruptured aneurysms as a result of an already weakened vessel wall. Perforation can be induced by a guidewire, microcatheter or coil [22]. Park et al. [23] has conducted a meta-analysis of studies over the period 2011-2017 stating an IAR incidence of 5.52% in treatment for previously ruptured intracranial aneurysms and 1.36% for unruptured aneurysms. Especially a small aneurysm size (<3-5 mm) and a complex aneurysm location (anterior communicating artery) are risk factors for IAR and would benefit from improved microcatheter steerability. The following summation states the mechanisms of rupture as mentioned in the literature:

1. The deposition of coils results in a swinging motion of the micro-catheter tip inside the aneurysm sac. The tip moving back and forth can damage the aneurysm dome and induce aneurysm rupture. This mechanism is more evident during the initial coil positioning as it stabilizes with subsequent coils in place [24].

2. The deployment of a coil in the aneurysm sac creates tension between the coil and the aneurysm wall. When coils do not have enough space to unravel, the tension on the aneurysm wall increases. An excessive tension on aneurysm wall induces aneurysm rupture [24].

3. During the coiling procedure, the microcatheter's workspace decreases and thus the catheter is more likely to kick out of the aneurysm sac to the neighbouring artery. The reinsertion of the catheter creates forward pressure on the aneurysm wall though the coil mesh. This impulse can induce rupture [22].

4. To insert coils, the guidewire should first be removed from the microcatheter. This operation can relieve accumulated elastic energy stored in the catheter's body causing a forward jumping motion. This jump can puncture the vessel or aneurysm wall [22].

5. The microcatheter and the coils can direct the blood flow towards weak spots in the aneurysm dome which can rupture the aneurysm wall [22].

Thromboembolic events (TEs)

A thromboembolic event is defined as a partial or complete occlusion of arteries in the distal vascular territory of the aneurysm's parent artery. This blood occlusion induces a cerebral infarction, i.e. stroke. TEs are associated with a higher morbidity than IARs and occur in 2-15% of procedures [22]. The main mechanisms leading to a TE are stated below:

1. Coils can partly move out of the aneurysm sac. This is called a coil prolapse. Coil prolapse can be the result of coil misplacement or kick out of the catheter to the neighbouring vessel during the deployment of a coil. Blood clots can form on this coil and move to distal vasculature possibly inducing a TE [24].

2. Coils can get separated from the aneurysm and migrate to the distal vasculature. This can be a result of detachment failures, displacement or stretching of coils [24]. Coil migration has been reported in 4-6% of the procedures and can induce a TE [16].

3. Blood clots possibly form on the coil mesh while the procedure is in progress. In larger aneurysms, the residual blood is higher and larger blood clots will form. The formed thrombi can escape the aneurysm sac and induce a TE [22].

4. Due to contact with the catheter and vessel wall, the blood vessel can contract. This so-called vasospasm deteriorates the blood flow. Slower blood flow induces blood clot formation on the guidewire or microcatheter [22, 24].

Aneurysm recanalization

Aneurysm recanalization is the process where blood (re)accesses the aneurysm sac after the coiling procedure. Recanalization is caused by compaction of the coil mesh and is likely to

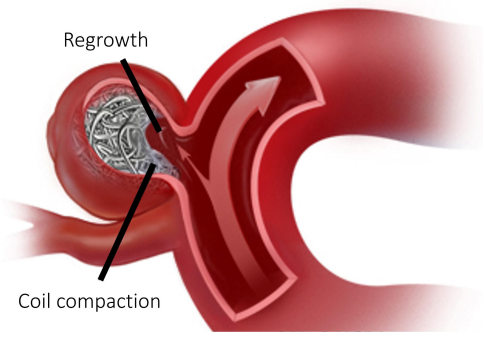

Figure 1-9: Illustration of aneurysm recanalization due to coil compaction in a coiled aneurysm, edited from [12].

happen when the achieved coil packing is not dense enough (Figure 1-9). While recanalization is not a peri- but postprocedural event, it is a common complication in endovascular coiling (20%), and thus worth mentioning. During the coiling procedure, the operator does not know the actual coil density or the aneurysm wall tension. Based on intuition, the procedure is interrupted to prevent intraprocedural aneurysm rupture [11, 13]. The modelling of the contact forces between the coil and the aneurysm wall could reduce post-procedural recanalization while preventing the aneurysm wall from rupturing.

Complication trade-off

Section 1-1-3 has provided an overview of the literature on common complication mechanisms during endovascular coiling procedures. Thromboembolic events are associated with a higher morbidity than intraprocedural aneurysm ruptures. To prevent the risk of TEs, anticoagulants, i.e. heparin, are administered before the procedure to inhibit blood clot formation. However, inhibition of coagulation increases the severity of a brain bleed after aneurysm rupture (Figure 1-10) [22]. The current challenge is to reduce the risk of intraprocedural aneurysm rupture during administration of anticoagulants. This could be accomplished by modelling contact forces between the coil and the aneurysm wall and improving the control over the catheter tip movement during coil deployment.

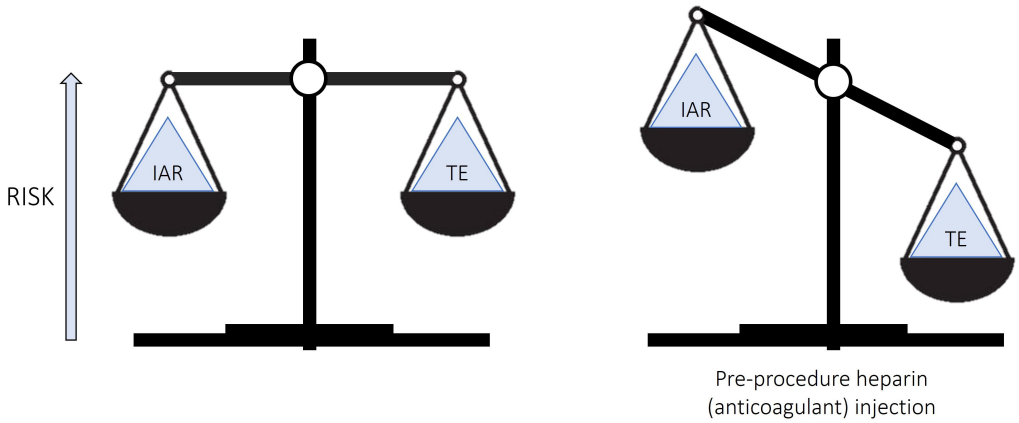

Figure 1-10: Trade-off in prevention of thromboembolic events and intraprocedural aneurysm rupture.

1-2 Thesis motivation

To validate the clinical relevance of this thesis, intraprocedural aneurysm rupture mechanisms from Section 1-1-3 have been discussed with interventional neuroradiologist Pieter Jan van Doormaal and neurologist Bob Roozenbeek from the Erasmus MC Rotterdam The Netherlands. First, this section elaborates on the most relevant rupture mechanism; coil-induced aneurysm rupture. Next, the research gap that motivates this thesis is based on expert clinical opinion from the Erasmus MC combined with the literature research on coil-induced aneurysm rupture, state-of-the-art microcatheter design, and state-of-the-art modelling and control for coils and microcatheters.

1-2-1 Coil-induced aneurysm rupture

The deployment of a coil in the aneurysm dome results in tension building up between the coil and the aneurysm wall. Excessive tension on the aneurysm wall induces aneurysm rupture. The increase in tension depends on the catheter position in the aneurysm dome. A recent study by Oishi et al. [25] has presented a realistic hydrogel aneurysm model to evaluate the effect of the catheter tip placement on the coil contact force and the catheter movement. It has been shown that a catheter positioned deeply in the aneurysm dome and therefore close to the aneurysm wall allows little space for the coil to deploy (Figure 1-11a), resulting in increased wall tension. This study has also presented that the reaction force from the aneurysm wall is partly transferred to the catheter tip, i.e. the tip's deflection increases when coils are deployed closer to the aneurysm wall (Figure 1-11b). When a catheter lies along the aneurysm wall during coil deployment, its restricted movement leads to an increase in tension between the catheter and the aneurysm wall. Thus, a catheter tip placed closely to the aneurysm wall or lying along the aneurysm wall results in an increased tension on the aneurysm wall. The study by Oishi et al. [25] has concluded that the catheter tip should be placed at the level of the aneurysm neck to maximize the distance from the aneurysm wall.

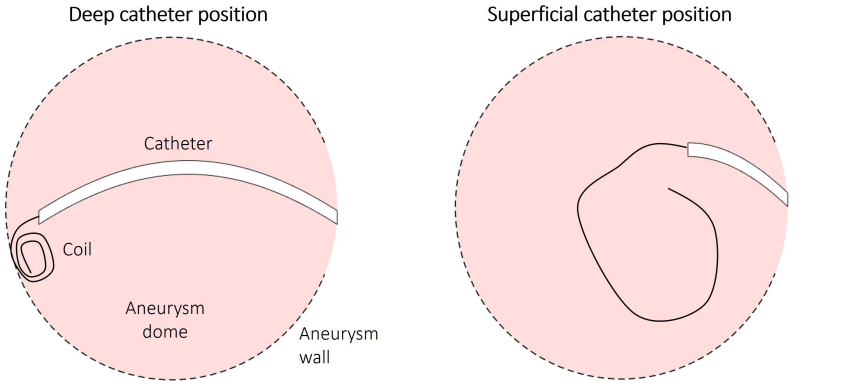

(a) Expansion of the coil structure based on the catheter's position during deployment.

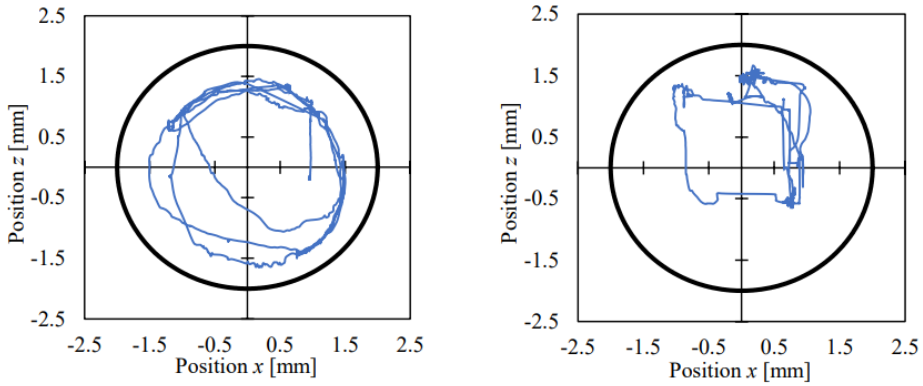

(b) Deviations of the catheter tip based on the catheter's position in Figure 1-11a, edited from [25].

Figure 1-11: Showing the relation between the insertion depth of the catheter and the deviation of it's tip upon deployment of a coil in the aneurysm dome.

1-2-2 Research gap

Although the study by Oishi et al. [25] has concluded that the catheter tip should be placed at the level of the aneurysm neck, clinical experts offer another perspective in this discussion. The interventional neuroradiologist Pieter Jan van Doormaal of the Erasmus MC has indicated that the catheter tip is often positioned deeper in the aneurysm dome to prevent the catheter from kicking out of the aneurysm. Kick-out requires reinsertion in the aneurysm sac. When the aneurysm is already partly filled, reinsertion is a complex manoeuvre that can induce aneurysm rupture (Section 1-1-3). Pieter Jan van Doormaal has pointed out that, to prevent intraprocedural aneurysm rupture, operators make use of the fact that the soft microcatheter moves in the same direction as the coil-wall reaction force, and thus relieves pressure from the aneurysm wall. This causes a waving motion, i.e. *paint-brushing*. During coil deployment, the operator slowly retracts the microcatheter. While this solution prevents the aneurysm from rupturing, its result is an uncontrolled way of coil deployment where kick-out of the catheter tip from the aneurysm sac can still occur. This problem asks for a new controlled and safe way to deploy coils in the aneurysm.

As discussed in Section 1-1-2, the first and only steerable microcatheter for intracranial aneurysm treatment, developed at UCSD by Gopesh et al. [1] (Figure 1-8), enables improved positioning of the catheter tip within the aneurysm dome. As of now, this microcatheter tip can only be manually positioned in the middle of the aneurysm dome and locked in its movement. Locking the catheter movement without knowledge of contact forces is dangerous, as the catheter loses its soft characteristics which would normally prevent rapid tension increase and rupture of the aneurysm wall. The presented tip by Gopesh et al. [1] would benefit from the modelling of these contact forces and control strategies for coil deployment procedures.

State-of-the-art literature on modelling of endovascular coils has mostly focused on the prediction of the coil's deployment trajectory in the aneurysm sac [17, 26, 27]. These methods either predict the trajectory of the coil in real time using geometric modelling, which does not take applied forces into account [17, 27], or employ exact finite element modelling, which is computationally expensive and requires offline computation [26]. As of now, no model exists that allows for the real-time modelling and control of the coil's contact forces with the aneurysm wall and the steerable catheter tip.

The controllable element connected to this endovascular coil model is the steerable catheter tip. The tip's motion should be controlled to stabilize the output of the system, i.e. the contact force between the coil and the aneurysm wall. Literature describes a catheter as a soft robot which can exactly be represented as a continuum robot, i.e. having an infinite dimensional space [28]. State-of-the-art literature on modelling of continuum robots has shown that through discretization of these structures, one can reveal the similarity between rigid and soft robots [28, 29]. Therefore, control structures developed for rigid robots have been adapted for the control of soft robots [29]. Since the motion of the soft robot is dominated by elastic effects, control efforts have focused on trying to shape the soft robot's potential energy using passivity-based control to achieve the desired robot configuration [29, 30, 31]. Passivity-based control should be adapted to the specific case where the controlled object, i.e. the catheter, is connected to another soft object, i.e. the endovascular coil. This endovascular coil has time-varying properties as it grows in the aneurysm and is placed between the catheter tip and the aneurysm wall. Moreover, the control strategy should be extended such that it allows

for the preservation of constraints which ensure the safety and the feasibility of the coiling procedure.

In conclusion, as of now, the field of robotic systems for neurovascular interventions is new and not a single system has been FDA-approved [19]. To the best of our knowledge, no research has been done in real-time modelling and control of the aneurysm wall tension in endovascular coil deployment procedures. This research would allow for a computer-controller steerable microcatheter tip that regulates the tension between a coil and the aneurysm wall while preventing the catheter from kicking out of the aneurysm. This robotic system would improve safety of coiling procedures and enable wider preventive treatment of intracranial aneurysms.

1-2-3 Research questions

Given the conclusion of the previous section, several research questions can be formulated:

Q1: What model can describe the motion of an endovascular coil and its forces applied on the aneurysm wall and a steerable microcatheter tip?

Q2: How can the growth of a coil throughout a coiling procedure be incorporated in the model of (**Q1**)?

Q3: What control architecture enables regulation of the contact force between the aneurysm wall and an endovascular coil?

Q4: How can the control architecture in (**Q3**) be extended to maintain the desired contact force throughout a coiling procedure while obeying the constraints imposed by the equipment and the environment?

1-3 Thesis objective

This thesis proposes how to adapt theory on modelling and control of soft robots to reduce the risk of coil-induced aneurysm rupture during intracranial aneurysm treatment. Qualitatively stated, this thesis aims to control a microcatheter system such that the contact forces between the endovascular coil and the aneurysm wall stay below the yielding threshold of the aneurysm wall while the steerable catheter tip position is maintained within the aneurysm sac and away from the aneurysm walls. When this objective is achieved, one would prevent coil-induced aneurysm rupture and catheter kick-out from the aneurysm sac. Mathematically stated and illustrated in Figure 1-12, the thesis objective is to regulate the aggregated contact force f between the coil and the aneurysm wall to the desired force $f^\star$, i.e.

$$\lim_{t\to\infty} f - f^\star = 0. \tag{1-1}$$

This regulation problem is subject to constraints, i.e.

$$\begin{aligned} f &\leq f_{max}, \\ (x_t, y_t) &\in X_{wall}, \\ (x_t, y_t) &\in X_{catheter}, \end{aligned} \tag{1-2}$$

where f_{max} is the yielding strength of the aneurysm wall, (x_t, y_t) is the tip position of the microcatheter, X_{wall} is the area or volume that evades catheter wall-collision and catheter kick-out and $X_{catheter}$ depicts the constraints imposed by the catheter's movement.

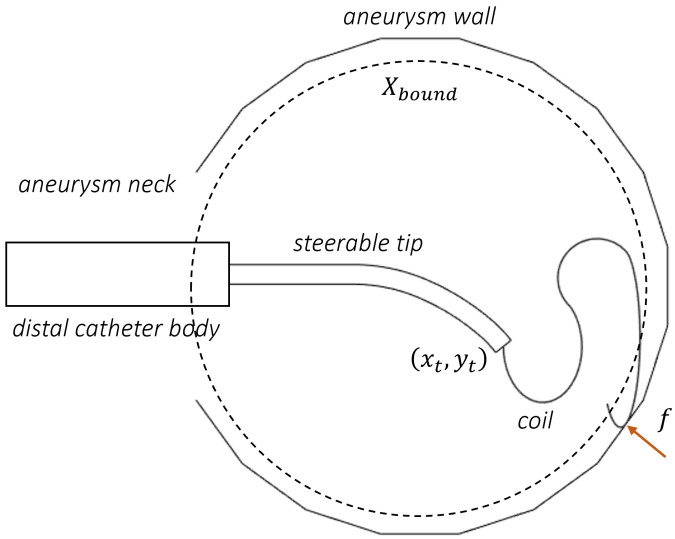

Figure 1-12: Illustration of the thesis objective.

By achieving the objective in Eqs. (1-1) and (1-2), this thesis has been the first attempt to dynamically model and control coil deployment in a real-time setting. The main contributions of this thesis are stated below and closely related to the research questions in Section 1-2-3:

1. A new way to dynamically model an endovascular coil and its interaction with the aneurysm wall and a steerable microcatheter tip (**Q1**).
2. A new way to dynamically model a coil deployment procedure through estimation and incorporation of coil growth parameters (**Q2**).
3. A proposed control architecture which enables indirect regulation of the contact force between the aneurysm wall and an endovascular coil. This entails the design of an augmented energy-shaping joint controller (**Q3**).
4. A proposed control architecture which enables asymptotic stabilization of the contact force between the coil and the aneurysm wall throughout a coil deployment procedure while obeying the constraints imposed by the equipment and the environment. This entails the design of a constraint preservation controller that maintains the desired catheter tip position on a derived constraint surface, and thus preserves the feasibility of the presented force-regulating energy-shaping controller (**Q4**).

1-4 Thesis outline

The thesis is structured as follows. Chapter 2 presents the modelling coil deployment procedure through modelling and interconnection of soft catheter dynamics, soft coil dynamics and coil growth dynamics. Chapter 3 presents a control architecture to achieve the force

control objective in Eq. (1-1) in a setting where no extra coil material is added to the system. Chapter 4 presents a control architecture such that the objective in Eq. (1-1) is achieved throughout a coil deployment procedure while adhering to the constraints stated in Eq. (1-2). Chapter 5 concludes this thesis and discusses future research directions.

Chapter 2

Modelling coil deployment dynamics

This chapter presents a new way to dynamically model an endovascular coil and its interaction with a microcatheter and the aneurysm wall throughout a coil deployment procedure. The main advantage of this model is its low computational complexity allowing real-time control computation. Section 2-1 presents a dynamic microcatheter model based on state-of-the-art research. Section 2-2 proposes a new dynamic endovascular coil model by exploiting the coil's basic mechanic properties. Section 2-3 interconnects these systems and presents a new way to incorporate coil growth during the coil deployment procedure. Section 2-4 discusses the modelling assumptions and their limitations.

2-1 Catheter model

This section presents a dynamic model for a steerable intracranial microcatheter and discusses how to sense its configuration. A catheter is an inherently flexible structure that does not contain any rigid links or joints. This allows for smaller construction, increased range of motion and more softness than their rigid counterparts [32]. A continuum robot is an equivalent modelling representation where the number of virtual joints approaches infinity, resulting in continuous tangents along the catheter length [33]. While the degree of freedom is large, the number of kinematic inputs to control the catheter shape is typically small. A medical catheter is thus considered to be a hyperredundant continuum robot [32].

2-1-1 Actuation mechanism

To allow for optimal catheter control with minimal actuation, the catheter tip section is controlled while the larger proximal catheter body is assumed to passively follow the vascular trajectory. Actuation mechanisms for microcatheters should be extrinsic, which means that the actual driving force is placed at the catheter base outside of the patient. This allows for improved miniaturization over intrinsic actuation, e.g. micromotors. Multiple extrinsic actuation mechanisms have been proposed to steer continuum robots such as tendons, bellows, memory alloys, magnets and concentric tubes [28, 34, 35]. Tendon-driven actuation and pneumatic actuation are the most suitable choices for intracranial microcatheter control.

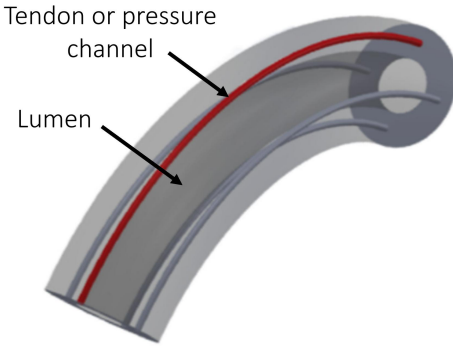

Figure 2-1: Steerable microcatheter tip, edited from [1]. Tendon-driven: tip bends to the channel of the strained tendon. Pressure-driven: tip bends to the opposite side of the inflated channel.

These designs allow for an inner lumen to guide endovascular coils, fast actuation, and span a large workspace which is useful in a partially unknown environment [1, 33]. A typical single-section, pneumatically or tendon-driven catheter is illustrated in Figure 2-1. The steerable microcatheter design by the University of California San Diego (UCSD), as introduced in Section 1-1-2, uses pneumatic actuation. However, this thesis limits its scope to the modelling and control of tendon-driven continuum robots. Tendon-driven robots have been used in multiple catheter designs and their actuation mechanism can be intuitively modelled [28]. By increasing the number of tendons, the steerable tip section can be separated into multiple steerable segments, however, this poses a trade-off between increased dexterity and an increased catheter diameter. While tendon-driven catheters have not yet been miniaturized down to 1 mm, i.e. the required diameter to move through intracranial vasculature, this is expected to be accomplished in the near future.

2-1-2 Modelling frameworks

Catheters have often been modelled in a quasi-static fashion [33]. This is due to 1) the low mass of the surgical continuum manipulator resulting in modal frequencies that are far higher than the frequency of relevant surgical motions, and 2) the actuator forces that are usually dominated by elastic energy storage and friction rather than inertial effects. Thus, kinematic and static models have often thought to be suitable alternatives [33]. However, this thesis

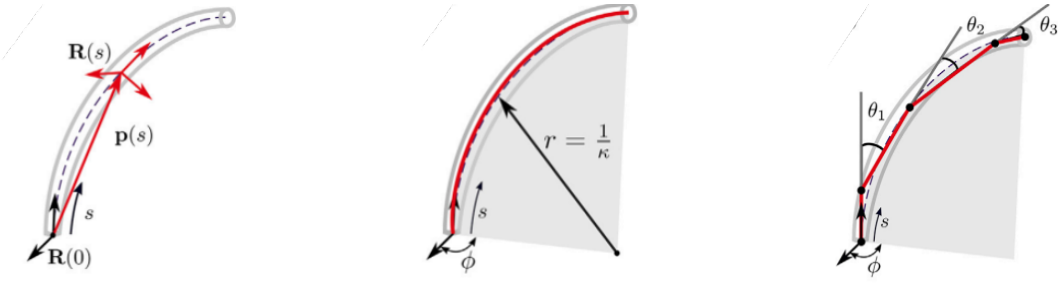

$\mathbf{X}(s) = [\mathbf{u}(s), \mathbf{v}(s)]$ **(a)** Variable curvature

$\mathbf{X}_\mu = [\kappa, \phi]$ **(b)** Constant curvature

$\mathbf{X}_\mu = [\phi, \theta_1, \theta_2, \theta_3]$ **(c)** Pseudo-rigid body

Figure 2-2: Continuum robot kinematics representations, edited from [28].

aims to capture and control the dynamic relationship between the catheter and coil. This motion is faster than the conventional surgical motion [20], and thus this thesis discards static models and focuses on dynamic modelling approaches.

In the modelling of continuum manipulators, a distinction can be made between lumped and distributed backbone parameterization. In distributed parameterization (Figure 2-2a) the manipulator's curve is represented by a rotational frame $R(s)$ and position $p(s)$ which are continuous functions of the distance s along the curve length ℓ [28]. These functions develop along ℓ according to a set of differential equations, i.e.

$$\begin{aligned} \frac{dR(s)}{ds} &= R(s)\hat{u}(s), \\ \frac{dp(s)}{ds} &= R(s)v(s), \end{aligned} \tag{2-1}$$

where the strain vectors, $u(s)$ and $v(s)$, are analogous to angular and linear velocity but are expressed in the spatial domain instead of the time domain. A classical distributed parameter model, i.e. the Cosserat model, requires solving six spatial partial differential equations at each time step. This limits its real-time applicability. It has been argued that the improvement in accuracy attained by such a complex model is not significant enough considering the required computational cost [36]. A more suitable alternative is lumped parameterization, where the backbone pose is represented by a finite set of parameters. The order of discretization determines both the accuracy and computational complexity of the model. While the constant curvature model (Figure 2-2b) describes a manipulator with a single curvature, the pseudo-rigid body representation (Figure 2-2c) is a more versatile and popular discretization strategy that will be further discussed in the following section.

2-1-3 Pseudo-rigid body model

It has been shown that a low-order discretized model can still provide a good approximation of elastic structures [33]. The Pseudo-rigid Body (PRB) model is a subclass that describes a flexible structure as rigid body structures coupled by elastic elements. More specifically, the PRB nR models represent an initially straight cantilever beam as $n+1$ rigid links in series connected by n revolute joints [37]. These joints are accompanied by three rotational springs to account for the beam's flexibility. Figure 2-3 shows a three-dimensional view of the PRB 3R representation by Su et al. [37]. This representation is a popular choice as it combines low-order discretization with high accuracy on the end coordinates, i.e. the tip position, of the catheter. The following sections derive the equations of motion for the general PRB nR robot representation. The steerable catheter tip is assumed to undergo minimal torsion, and thus bends in a single plane [38]. The dynamical model is therefore described in 2D.

Rigid body dynamics

A general two-dimensional PRB nR structure has been illustrated in Figure 2-4. Its corresponding variables have been depicted in Table 2-1. Hamiltonian or Lagrangian mechanics are commonly used to represent the equations of motion for PRB nR robots. This thesis follows the Lagrangian approach. More specifically, it adapts a vector representation of the

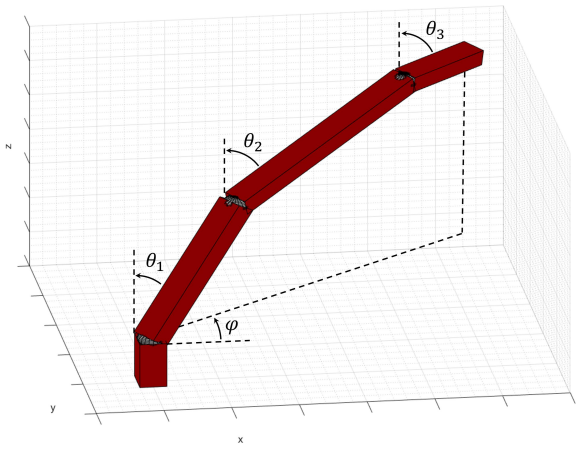

Figure 2-3: Three-dimensional illustration of a pseudo-rigid body 3R robot.

Lagrange equations of motion by Vallery and Schwab [39]. In this method, the principle of virtual work is used to directly relate Newton's laws to the equations of motion without the need for deriving energy equations. The derivation starts with the virtual power expression for an unconstrained system consisting of n rigid bodies, that is

$$\delta P = \delta\dot{\xi}_i(F_i - M_{ii}\ddot{\xi}_i), \quad i = 1...n, \tag{2-2}$$

where $\xi_i = (x_i, y_i, \phi_i)$ are the coordinates of the Centre of Mass (CoM) of the i^{th} rigid body, $F_i = (F_x, F_y, M)$ are the applied forces on this CoM and $M_{ii} = \text{diag}(\mu_i, \mu_i, I_i)$ is the diagonal mass matrix of the i^{th} body with mass μ_i and inertia I_i.

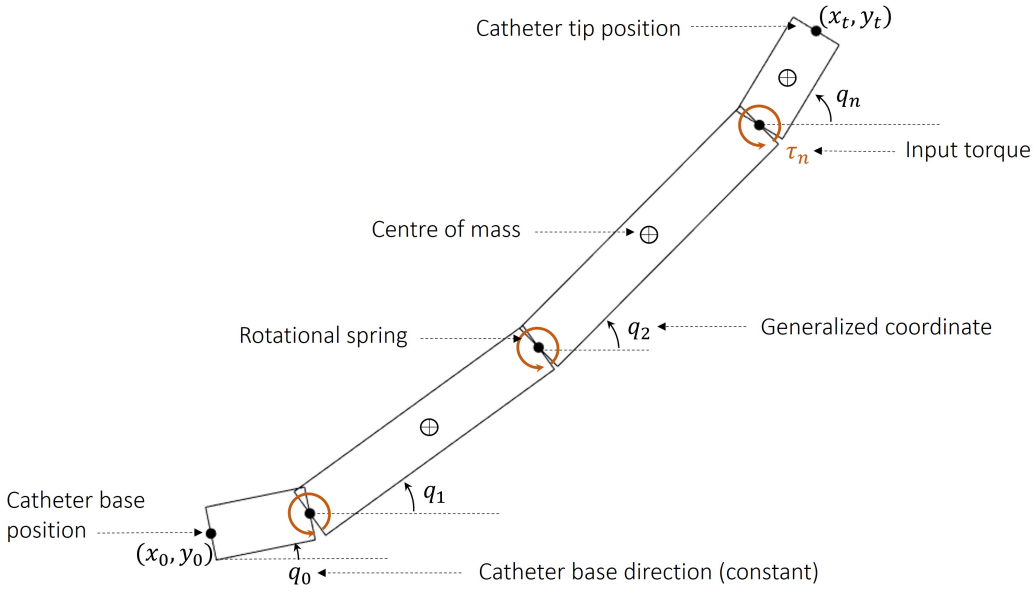

Figure 2-4: Two-dimensional illustration of a pseudo-rigid body nR robot.

A system is in dynamic equilibrium if $\delta P = 0$ is true for all virtual velocities $\delta\dot{x}$ that comply with the kinematic body constraints. These kinematic constraints can be incorporated by

writing the CoM coordinates of the rigid bodies in a set of generalized, i.e. the minimum number of, coordinates $q \in \mathbb{R}^n$ using mapping $\xi = T(q)$. In the case of the PRB nR system, this mapping can be found by multiplication of homogeneous transformation matrices, i.e.

$$\underbrace{\begin{bmatrix}\xi_1\\ \xi_2\\ \vdots\\ \xi_n\end{bmatrix}}_{\xi} = \underbrace{\begin{bmatrix}G_1H_0\\ G_2H_1H_0\\ \vdots\\ G_n...H_1H_0\end{bmatrix}\begin{bmatrix}0\\0\\1\end{bmatrix}}_{T(q)}, \tag{2-3}$$

with,

$$H_i = \begin{bmatrix}\cos\Delta q_i & -\sin\Delta q_i & \ell_i\cos\Delta q_i\\ \sin\Delta q_i & \cos\Delta q_i & \ell_i\sin\Delta q_i\\ 0 & 0 & 1\end{bmatrix}, \quad G_i = \begin{bmatrix}\cos\Delta q_i & -\sin\Delta q_i & \ell_i/2\cos\Delta q_i\\ \sin\Delta q_i & \cos\Delta q_i & \ell_i/2\sin\Delta q_i\\ 0 & 0 & q_i\end{bmatrix}, \tag{2-4}$$

where $\Delta q_i = q_i - q_{i-1}$ is the relative joint angle between the $(i-1)^{\text{th}}$ and i^{th} rigid body and q_i is the joint angle of the i^{th} rigid body defined counterclockwise with respect to the global x-axis. The catheter base angle q_0 is assumed constant and uncontrollable. The discussion in Section 2-4 elaborates on this modelling choice. Note that, in a coiling procedure, the operator can push and pull the catheter along direction q_0. This adds an extra degree of freedom to the system which will be introduced in Chapter 4. Given the mapping $T(q)$ in Eq. (2-3), the velocities $\dot{\xi}$ and accelerations $\ddot{\xi}$ of the rigid body CoM coordinates can be written in terms of generalized coordinates q and its derivatives $\dot{q}$ and $\ddot{q}$) by taking the first and second time derivative of $T(q)$, i.e.

$$\dot{\xi} = \underbrace{\frac{\partial T(q)}{\partial q}}_{T_q}\dot{q} \quad \text{and} \quad \ddot{\xi}_i = \frac{\partial T(q)}{\partial q}\ddot{q} + \underbrace{\frac{\partial^2 T(q)}{\partial q^2}}_{T_{qq}}\dot{q}\dot{q}. \tag{2-5}$$

By combining Eq. (2-2), Eq. (2-3) and Eq. (2-5), one can formulate the dynamic equilibrium for a kinematically constrained rigid body system expressed in generalized coordinates, that is

$$F - M\ddot{\xi} = T_q^T\left[F - M(T_q\ddot{q} + T_{qq}\dot{q}\dot{q})\right] + Q(u) = 0, \tag{2-6}$$

where $Q(u)$ is a projection of the input tendon torques u on the generalized coordinates, i.e. joint angles. When the catheter is wired such that each joint can individually be actuated by a tendon, these so-called generalized torques are equivalent to the input of the system, i.e. $Q(u) = I_n u$ where I_n is a $n \times n$ identity matrix.

Pseud-rigid body dynamics

The next step is to transform the rigid body system in Eq. (2-6) into a pseudo-rigid body system. Flexibility is introduced by placing passive elements, i.e. torsional springs between the rigid body structures. These springs are commonly assumed to bend according to Euler-Bernoulli law [38, 40], which means that the applied torque τ_i is linearly related to bending angle Δq_i through stiffness k_i, i.e.

$$\tau_i = k_i\Delta q_i, \tag{2-7}$$

where $\Delta q_i := (q_i - q_{i-1})$ is the relative bending angle and k_i is the beam stiffness defined as

$$k_i = \kappa_i \frac{EI}{L}, \tag{2-8}$$

where E, I, L are respectively the Young's modulus, the moment of inertia and the length of the steerable catheter tip. The characteristic stiffness κ is a constant vector that can be chosen based on the number of links in the PRB system and has been optimized for various PRB systems [37]. According to Schwab and Vallery [39], these passive elements generate the following generalized spring force,

$$Kq + c = \left(\frac{\partial \Delta q}{\partial q}\right)^T \text{diag}(k_1, ..., k_n)\Delta q, \tag{2-9}$$

where K is symmetric positive definite and c is a constant. To simulate the natural behaviour of the elastic body subject to viscous friction, a damping term is commonly added parallel to the joint springs. By replacing Δq in Eq. (2-9) by $\Delta \dot{q}$, this results in the classical Rayleigh

Variable	**Description**	**Function**
State parameters		
q	Joint angles	q
$\dot{q}$	Joint velocities	$\dot{q}$
y	State vector	$[q^T, \dot{q}^T]^T$
$\dot{y}$	State derivative	$[\dot{q}^T, \ddot{q}^T]^T$
q_0	Angle of catheter base	q_0
ξ_i	Centre of mass vector	$[x_1, y_1, \varphi_1]^T$
$[x_t, y_t]^T$	Tip coordinates, Eq. (2-4)	$h(q) := H_n ... H_1 H_0$
PRB model parameters		
γ	Characteristic length	$\sum_{i=0}^{n} \gamma_i = 1$
κ	Characteristic stiffness	$\sum_{i=0}^{n} \frac{1}{\kappa_i} = 1$
Catheter properties		
L	Length	L
ℓ_i	Link length	$\gamma_i L$
m	Mass	m
μ_i	Link mass	$\gamma_i m$
E	Young's modulus	E
I	Moment of inertia	$mL^2/12$
I_i	Link moment of inertia	$\mu_i \ell_i^2/12$
k_i	Joint stiffness	$\kappa_i EI/L$
d_i	Spring damping coefficient	d_i
Other parameters		
g	Gravitational acceleration	g

Table 2-1: Required variables to describe the pseudo-rigid body model in Eq. (2-13).

dissipation function stated by Lord Rayleigh in 1873, i.e.

$$D\dot{q} = \left(\frac{\partial \Delta\dot{q}}{\partial \dot{q}}\right)^T \text{diag}(d_1, ..., d_n)\Delta\dot{q}, \tag{2-10}$$

where d_i is the i^{th} joint damping coefficient. By adding Eq. (2-9) and Eq. (2-10) to the set of equations in Eq. (2-6), the equations of motion for the PRB nR model follow as

$$M(q)\ddot{q} + C(q,\dot{q})\dot{q} + Kq + c + D\dot{q} + g(q) = Q(u), \tag{2-11}$$

where the system matrices are defined as

$$M(q) := T_q^T M T_q, \quad C(q,\dot{q}) := T_q^T M T_q \dot{q}, \quad g(q) := T_q q^T F. \tag{2-12}$$

Joint angles and velocities can be computed through explicit numeric integration by writing

$$f(y) = \frac{d}{dt}\begin{bmatrix} q \\ \dot{q} \end{bmatrix} = \begin{bmatrix} \dot{q} \\ M(q)^{-1}\left[Q(u) - C(q,\dot{q})\dot{q} - Kq - c - D\dot{q} - g(q)\right] \end{bmatrix}, \text{ with } y = \begin{bmatrix} q \\ \dot{q} \end{bmatrix}, \tag{2-13}$$

and adapting a higher order, e.g. fourth order, Runge-Kutta integration scheme to ensure numerical stability, i.e.

$$\begin{array}{rcl} k_1 & = & f(y), \\ k_2 & = & f(y + k_1\frac{\Delta t}{2}), \\ k_3 & = & f(y + k_2\frac{\Delta t}{2}), \\ k_4 & = & f(y + k_3\Delta t), \\ y & = & y + \frac{1}{6}(k_1 + 2k_2 + 2k_3 + k_4)\Delta t, \end{array} \tag{2-14}$$

where Δt is the time step for integration.

Model properties

The Euler Lagrange system in Eq. (2-11) contains various useful properties. These properties will be exploited in the following chapters to design a contact force controller and prove its stability.

Property 2.1 The matrix $M(q)$ is positive definite and symmetric [39].

Property 2.2 The matrix $C(q,\dot{q})$ is defined such that [41]

$$\dot{M}(q) = C(q,\dot{q}) + C^T(q,\dot{q}). \tag{2-15}$$

Property 2.3 There exists a positive constant k_g such that the Jacobian of the generalized gravity torque $g(q)$ is bounded by

$$k_g \geq \left|\left|\frac{\partial g(q)}{\partial q}\right|\right| \quad \forall q \in \mathbb{R}^n, \tag{2-16}$$

which is always true for a robot which solely consists of rotational joints [41, 31]. It can be verified that this upper bound can be found by evaluating the gravitational Hessian,

$$k_g = n\left(\max_{i,j,q}\frac{\partial g_i(q)}{\partial q_j}\right) = n\left(\max_{i,j}\frac{\partial g_i(\frac{\pi}{2})}{\partial q_j}\right). \tag{2-17}$$

Property 2.4 If the system in Eq. (2-11) is fully actuated, i.e. $Q(u) = I_n u$, then the system defines a passive map $u \mapsto \dot{q}$ [31]. A notion of passivity is given in Appendix B-2.

2-2 Endovascular coil model

This section aims to model the coil's behaviour when subjected to forces from the microcatheter and the aneurysm wall. First, a research gap is formulated in the literature on coil modelling techniques. Thereafter, a new real-time feasible dynamic model for an endovascular coil is proposed by exploiting the coil's basic mechanic properties.

It has been discussed in Section 1-1-2 that endovascular coils are manufactured in a tertiary shape, e.g. helical or spherical, based on the aneurysm's geometry. By straightening these coils, i.e. to be guided through the microcatheter's lumen, elastic potential energy is stored in the coil [17]. When a coil cannot fully return to its tertiary structure during deployment, tension increases between the coil and the aneurysm wall as a result of the coil's stored elastic energy. To regulate this tension with a steerable microcatheter, a dynamic coil model is desired. In contrast to the vast body of literature on the dynamic modelling of medical catheters, little research has been done on the dynamic modelling of coil deployment. Finite element modelling (FEM) has been used to accurately model the physical properties of the coil and the full mechanics of the coil deployment procedure [26]. However, FEM carries a computational burden prohibiting itself from being used in a clinical workflow [17, 27]. This is why pure geometric algorithms are often used for simulating coil packing, omitting mechanics modelling [27]. Recently, Patel et al. [27] has developed an algorithm to guess a coil's trajectory after collision with the aneurysm wall or other coils. While geometric modelling is a possibility, it disregards the effect of coil deployment on wall tension and catheter tip movement. This is why this thesis takes a simplified modelling approach based on the prominent mechanical property of the coil; its elasticity. Sarayi et al. [17] has presented a simplified way to model the secondary structure of a coil by considering the coil as a series of equal-length linear stretching springs. These linear springs are connected with nodes functioning as torsional springs to allow for coil bending. Figure 2-5a illustrates this discretization strategy

(a) Helical endovascular coil represented as a series of linear springs connected by rotational springs, according to [17].

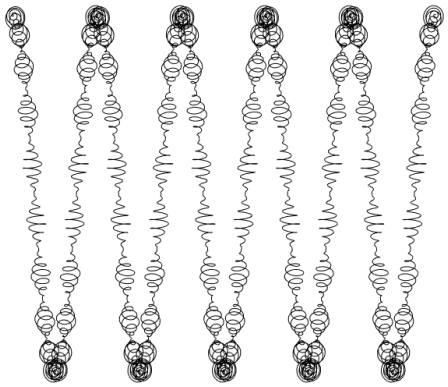

(b) Projection Figure 2-5a on XY plane, showcasing the spring structure in longitudinal direction.

Figure 2-5: Mechanics representation of endovascular coil.

applied on a helical-shaped coil. While the approach by Sarayi et al. [17] is an efficient way to describe coil mechanics, the system still contains many degrees of freedom and contact points with the environment. The computation of a control strategy for Figure 2-5a to reduce contact forces is a hard problem, especially in real time. Moreover, the model by Sarayi et al. [17] assumes a static catheter tip position while this thesis aims to model its dynamic interaction with the endovascular coil. To perform real-time control on coil-aneurysm reaction forces, a simpler low-order dynamic coil model is required.

2-2-1 Mass-spring-damper model

This section presents a new way to dynamically model an endovascular coil and its interaction with a static microcatheter and the aneurysm wall. Figure 2-5b shows the projection of the tertiary helical structure in Figure 2-5a on the XY plane. It can be observed that this projection resembles a spring that can be compressed or elongated along its length. Given this observation, this thesis proposes to lump the individual coil components in Figure 2-5b together in a single point mass, i.e. m_c, that interacts through springs and dampers with the aneurysm wall and catheter body (Figure 2-6). The aneurysm's stiffness and damping constants are defined by k_e and d_e respectively. The stiffness and damping constants of the coil with respect to the catheter are defined by k_c and d_c. In this section, the catheter is represented with a constant force F working on the coil system. First, the coil's equations of motion are derived with respect to the catheter tip. Thereafter, this system is extended with a compliant contact model to reflect the interaction with the coil and the aneurysm wall.

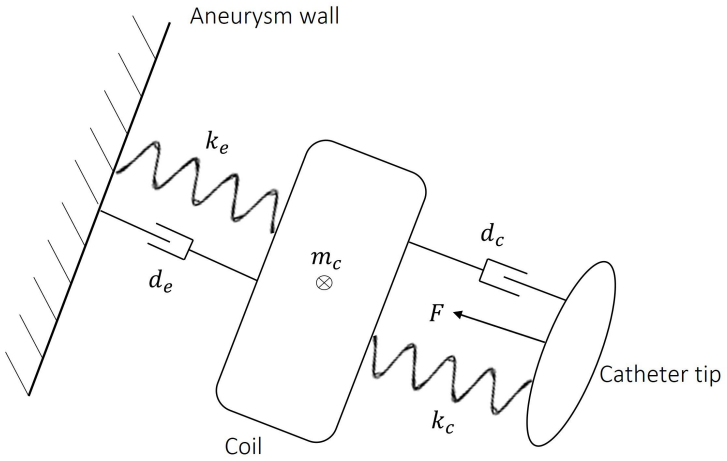

Figure 2-6: Endovascular coil structure in Figure 2-5b lumped together in a point mass (m_c) connected by springs (k) and dampers (d) to the aneurysm wall and the steerable catheter tip.

Coil-catheter interaction

Figure 2-7 shows the coordinates and measures corresponding to Figure 2-6. Three points of interest are the contact point in the environment (x_e, y_e), the CoM of the coil's helical structure (x_c, y_c) and the end position of the steerable catheter tip (x_t, y_t). When the coil can move freely through space, its degrees of freedom are represented by its position, i.e. (x_c, y_c). However, the assumption is made that the coil's mass is constrained to move on the line

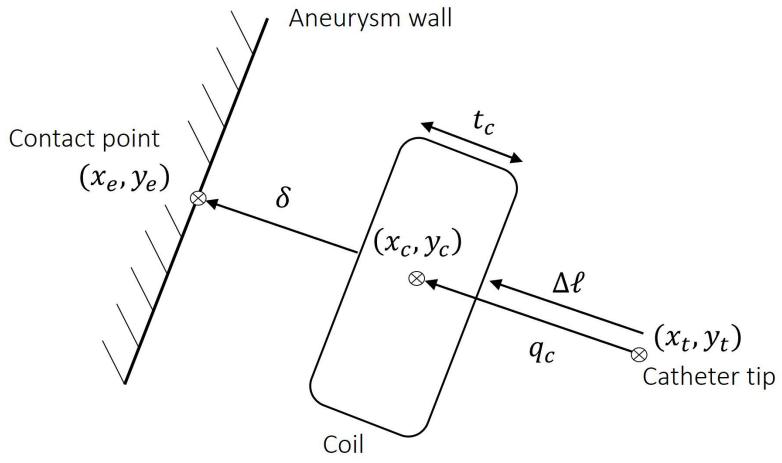

Figure 2-7: Coordinates and distance vectors corresponding to Figure 2-6.

between the catheter tip and the contact plane, and thus transferring catheter tip forces to the contact point and vice versa. It has already been discussed in Section 1-2 and Section 2-2 that this modelling assumption reflects reality. The constrained coil position is expressed as

$$\begin{bmatrix} x_c \\ y_c \end{bmatrix} = \begin{bmatrix} x_t \\ y_t \end{bmatrix} + q_c \frac{\begin{bmatrix} x_e \\ y_e \end{bmatrix} - \begin{bmatrix} x_t \\ y_t \end{bmatrix}}{\left\| \begin{bmatrix} x_e \\ y_e \end{bmatrix} - \begin{bmatrix} x_t \\ y_t \end{bmatrix} \right\|}, \tag{2-18}$$

where q_c is a generalized coordinate constrained to move on the line between the catheter tip position (x_t, y_t) and the known contact point (x_e, y_e). The catheter tip position (x_t, y_t) can be computed through forward kinematics of the PRB model as described in Table 2-1. With the assumption that the spring interconnection between the catheter and the coil is linear, its spring energy $\mathcal{E}_{c,s}(q_c)$ is defined as

$$\mathcal{E}_{c,s}(q_c) = \frac{1}{2} k_c \Big(\underbrace{q_c - \frac{t_c}{2}}_{\Delta\ell} \Big)^2, \tag{2-19}$$

where $k_c, \Delta\ell, t_c$ are respectively the coil's stiffness coefficient, the spring elongation, i.e. the distance between the catheter tip and the spring attachment point on the coil, and the coil's helix length, serving as a coil growth parameter during coil deployment. Note that, by the definition in Eq. (2-19), the spring in Figure 2-5 is in elongated state. A compressive force on the coil implies a negative value for $\Delta\ell$, i.e. the catheter tip is placed partly inside the coil structure (Figure 2-8). For visualization purposes, one can add an offset $\Delta\ell_0$ to elongation $\Delta\ell$. This does not change system dynamics. Also note that, by increasing t_c and keeping (x_t, y_t) fixed, $\Delta\ell$ increases, and thus results in a larger compressive force on the aneurysm wall. The incorporation of coil growth with t_c is described in more detail in Section 2-3-1. The generalized coil-catheter spring force $F_{c,s}(q_c)$ can be derived from the spring energy defined in Eq. (2-19), i.e.

$$F_{c,s}(q_c) = \frac{\partial \mathcal{E}_{c,s}(q_c)}{\partial q_c} = k_c \left(q_c - \frac{t_c}{2} \right). \tag{2-20}$$

The generalized coil-catheter damping force $F_{c,d}(\dot{q_c})$ is defined according to a Rayleigh dissipation function representing viscous friction, that is

$$F_{c,d}(\dot{q_c}) = d_c \dot{q_c}, \tag{2-21}$$

where d_c is the coil's damping coefficient. Given that a static catheter tip exerts force F on point (x_t, y_t), the dynamics of the coil system can be derived following the same Langrangian vector approach as for the steerable catheter tip in Section 2-1-3, i.e.

$$M(q_c)\ddot{q_c} + k_c(q_c - \frac{t_c}{2}) + d_c\dot{q_c} = F, \tag{2-22}$$

where the system matrices are defined as

$$T_{q_c} = \frac{\partial\left(\begin{bmatrix} x_c \\ y_c \end{bmatrix}\right)}{\partial q_c} = \frac{\begin{bmatrix} x_e \\ y_e \end{bmatrix} - \begin{bmatrix} x_t \\ y_t \end{bmatrix}}{\left\| \begin{bmatrix} x_e \\ y_e \end{bmatrix} - \begin{bmatrix} x_t \\ y_t \end{bmatrix} \right\|} \quad \text{and} \quad M(q_c) := T_{q_c}^T m_c T_{q_c}. \tag{2-23}$$

The coil's gravitational forces are assumed negligible, hence are omitted for simplicity.

Coil-wall interaction

The previous section has proposed an interconnection between the coil and the catheter tip. The next step is to introduce contact between the coil and the aneurysm wall. The literature describes two types of contact models; rigid contact models and compliant contact models [42]. Rigid or non-smooth contact models assume an instantaneous contact process. The bodies in contact are considered to be rigid solids, i.e. experience negligible deformations. This is not the case for a coil interacting with the aneurysm wall, as both bodies are not infinitely stiff and contact is maintained for an indefinite timespan. In contrast to rigid contact models, penalty or compliant methods have been proposed. Most compliant models consist of an elastic component, i.e. the spring, and an energy dissipation component, i.e. the damper [42]. In this thesis, the use of a damper between the coil and the aneurysm wall is omitted, as it simplifies the derivation of the generalized contact force. Dissipation of energy still takes place through the damper between the catheter and the coil. It is then proposed to use Hooke's contact model to model contact force $F_e(\delta)$, that is

$$F_e(\delta) = \begin{cases} k_e\delta & \delta \leq 0 \\ 0 & \delta > 0 \end{cases}, \tag{2-24}$$

where k_e and δ are the aneurysm wall stiffness and the relative indentation between the wall and the coil. When the distance between the two bodies is positive, no contact occurs, whereas a negative value of δ indicates contact between the bodies. A coil in contact with the aneurysm wall has been illustrated in Figure 2-8. The aneurysm wall is portrayed as a soft structure allowing indentation. The wall's indentation δ is defined as

$$\delta = \left\| \begin{bmatrix} x_e \\ y_e \end{bmatrix} - \begin{bmatrix} x_t \\ y_t \end{bmatrix} \right\| - \delta_{max} - q_c - \frac{t_c}{2}, \tag{2-25}$$

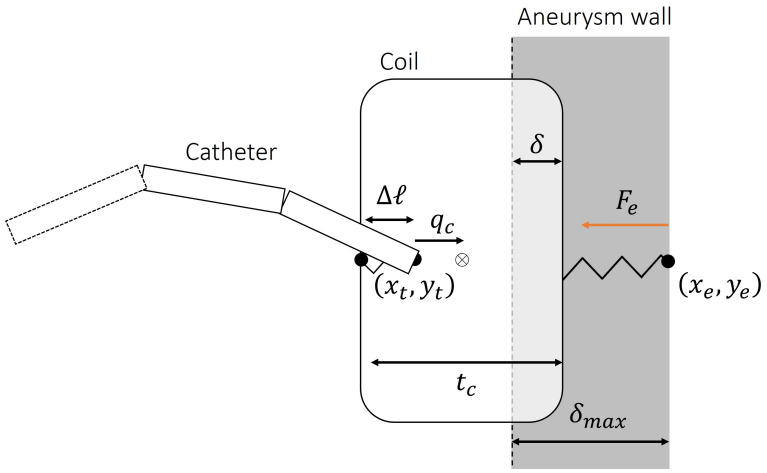

Figure 2-8: Illustration of an endovascular coil in contact with the aneurysm wall. The relative indentation between these two bodies is indicated with δ.

where $\delta_{max} := F_{e,max}/k_e$ is the indentation depth that would yield the aneurysm wall. The yield stress $F_{e,max}$ of the aneurysm has been estimated by Cebral et al. [43], presenting ultimate stress values between 0.63-2.16 MPa for eight resected intracranial aneurysms. It has been shown that tissue stiffness k_e of structures similar to intracranial aneurysms can be found with Magnetic Resonance Elastography [44]. Note that (x_e, y_e) is a point located inside the aneurysm wall. Appendix B-3 discusses how this point can be determined from a 3D aneurysm reconstruction generated prior to treatment. Given a stiff catheter exerting force F, the dynamics of the coil system in Eq. (2-22) can be extended with the generalized contact force in Eq. (2-24), that is

$$M(q_c)\ddot{q}_c + k_c\left(q_c - \frac{t_c}{2}\right) + d_c\dot{q}_c + k_e\delta = F. \tag{2-26}$$

The next step is to combine the equations of motion for a steerable microcatheter tip, as defined in Eq. (2-11), with the coil dynamics derived in this section.

2-3 Coil deployment model

Section 2-1 has presented the Euler Lagrange equations of motion for a steerable microcatheter tip modelled according to the PRB framework. Section 2-2 has presented a new way to dynamically model an endovascular coil and its interaction with a static microcatheter and the aneurysm wall. This section presents how to interconnect these two models and proposes how to model a coil deployment procedure by introducing quasi-static coil growth parameters.

2-3-1 System model without coil growth

This section states a system of equations that interconnects the derived catheter and coil models. This system considers constant coil properties, i.e. no coil growth takes place. To

derive the interconnected system, a single transformation matrix $T(\psi)$ should be defined, that is,

$$T(\psi) = \begin{bmatrix} T(q)^T & x_c & y_c \end{bmatrix}^T, \text{ with } \psi := \begin{bmatrix} q^T & q_c \end{bmatrix}, \tag{2-27}$$

where $T(q)$ and (x_c, y_c) have been respectively defined in Eqs. (2-3) and (2-18) and ψ is the extended generalized coordinate vector joining the catheter angles q and the coil displacement q_c. By following the Lagrangian vector approach once more, the resulting system dynamic equations interconnect Eq. (2-11) and Eq. (2-26) as

$$M(\psi)\begin{bmatrix}\ddot{q}\\ \ddot{q}_c\end{bmatrix} + C(\psi,\dot{\psi})\begin{bmatrix}\dot{q}\\ \dot{q}_c\end{bmatrix} + \begin{bmatrix} Kq \\ k_c(q_c - \frac{t_c}{2})\end{bmatrix} + k_e\delta\begin{bmatrix}\partial\delta/\partial q\\ 1\end{bmatrix} + \begin{bmatrix} D\dot{q}\\ d_c\dot{q}_c\end{bmatrix} + \begin{bmatrix} g(q)\\ 0\end{bmatrix} = \begin{bmatrix} Q(u)\\ 0\end{bmatrix}, \tag{2-28}$$

where the new system matrices are defined as

$$M(\psi) := T_\psi^T \begin{bmatrix} M & 0\\ 0 & m_c\end{bmatrix} T_\psi, \quad C(\psi,\dot{\psi}) := T_\psi^T \begin{bmatrix} M & 0\\ 0 & m_c\end{bmatrix} T_{\psi\psi}\dot{\psi}, \tag{2-29}$$

and where the Jacobian and Hessian of the transformation matrix $T(\psi)$ are defined as

$$T_\psi := \frac{\partial T(\psi)}{\partial \psi}\dot{\psi}, \quad T_{\psi\psi} := \frac{\partial^2 T(\psi)}{\partial \psi^2}. \tag{2-30}$$

The resulting set of equations in Eq. (2-28) can be written in explicit form as

$$f(\psi,\dot{\psi}) = \frac{d}{dt}\begin{bmatrix} q\\ q_c\\ \dot{q}\\ \dot{q}_c\end{bmatrix} = \begin{bmatrix} \dot{q}\\ \dot{q}_c\\ M(\psi)^{-1}\left[\begin{bmatrix} Q(u)\\ 0\end{bmatrix} - C(\psi,\dot{\psi})\begin{bmatrix}\dot{q}\\ \dot{q}_c\end{bmatrix} - \begin{bmatrix} Kq + D\dot{q} + g(q)\\ k_c(q_c - \frac{t_c}{2}) + d_c\dot{q}_c\end{bmatrix} - k_e\delta\begin{bmatrix}\partial\delta/\partial q\\ 1\end{bmatrix}\right]\end{bmatrix}. \tag{2-31}$$

where $\psi := [q^T \quad q_c]$ and $\dot{\psi} := [\dot{q}^T \quad \dot{q}_c]$ are the state vector defined in Eq. (2-27) and its time derivative. Note that, when no contact takes place between the coil and the aneurysm wall, the indentation δ is positive and the term $k_e\delta[(\partial\delta/\partial q)^T \quad 1]^T$ does not appear in Eq. (2-31). Also note that the model properties for Euler Lagrange systems, as stated in Section 2-1-3, are still preserved for the new system in Eq. (2-31). The described set of equations in Eq. (2-31) has modelled a case where no coil growth takes place. The next section proposes to extend the system in Eq. (2-28) to the real case where coil deployment takes place, and thus coil growth dynamics should be incorporated.

2-3-2 Coil growth model

This section presents the system dynamics for an endovascular coil with variable properties, i.e. coil growth or deployment takes place. It can be reasoned that coil deployment entails the increase of the coil's mass (m_c) and size (t_c) over time. A larger coil would change the static equilibrium of the system while a heavier coil would change its inertial properties. Note that the growth parameter t_c has already been used in the definition of the coil's elastic energy in Eq. (2-19). Figure 2-9 illustrates that the growth of parameter t_c results in both the deflection of the catheter's tip position (x_t, y_t) as well as an increase of the indentation (δ) between the coil and the aneurysm wall. This indentation causes an increase of the aneurysm wall tension

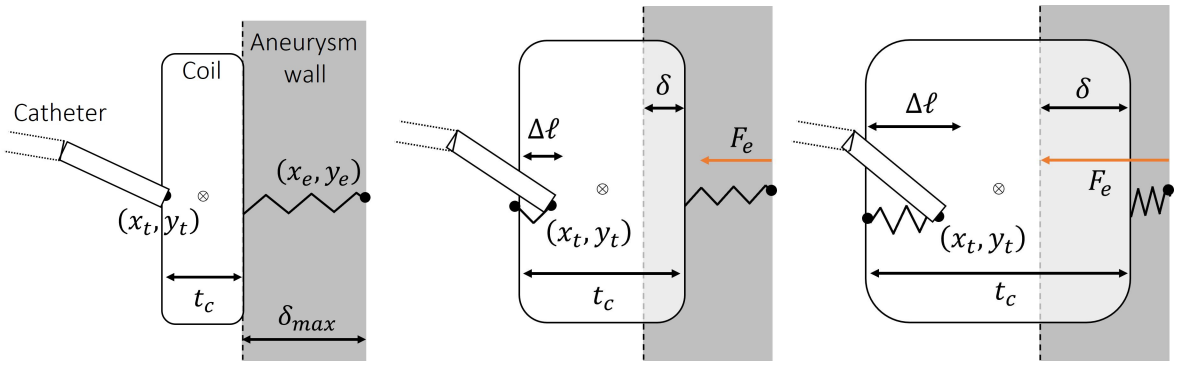

(a) No indentation & contact force. **(b)** Low indentation & contact force. **(c)** High indentation & contact force.

Figure 2-9: Illustration of three coil deployment stages. Growth of the coil's size (t_c) results in an increased deflection of the catheter tip position (x_t, y_t) and increased indentation (δ) between the aneurysm wall and the coil.

until the aneurysm wall yields. This growth of the coil in can be dynamically captured by the following set of equations, that is

$$\frac{d}{dt}\left(\begin{bmatrix} y \\ m_c \\ t_c \end{bmatrix}\right) = \begin{bmatrix} f(y, m_c, t_c) \\ r_m \\ r_t \end{bmatrix}, \text{ with } y^T := [\psi^T \quad \dot{\psi}^T], \tag{2-32}$$

where $f(y)$ denotes the coil-catheter-wall dynamics as defined in Eq. (2-31) and r_m and r_t respectively denote the rate of change of the coil's mass (m_c) and the rate of change of the coil's size (t_c). This thesis makes the assumption that the growth rates r_m and r_t are sufficiently slow such that the dynamic effect of m_c and r_t on system $f(y)$ is negligible. By the concept of perturbation theory, one can introduce a small parameter ϵ such that

$$dt := \epsilon dv, \tag{2-33}$$

where dv is a sufficiently slower time scale than dt such that the variables $[m_c \quad r_t]$ can be considered in quasi-steady state with respect to y [45]. Following this strategy, the system in Eq. (2-32) can be decoupled in two dynamic subsystems, that are

$$\begin{aligned} \frac{d}{dt} y &= f(y, \bar{m}_c, \bar{t}_c), \\ \epsilon \frac{d}{dv}\left(\begin{bmatrix} m_c \\ t_c \end{bmatrix}\right) &= \begin{bmatrix} r_m \\ r_t \end{bmatrix}, \end{aligned} \tag{2-34}$$

where the quasi-steady states $[\bar{m}_c \quad \bar{t}_c]$ emerge from the slower growth dynamics and are considered to be constant in faster developing system $f(y)$ without affecting its dynamics.

The growth rates r_t and r_m can be derived given the properties of the coil and the geometry of the aneurysm. The rate of change r_m for the coil mass m_c follows from

$$r_m = \rho_c \tau_{in}, \tag{2-35}$$

where ρ_c and τ_{in} are the coil's mass density per unit length and the coil's injection velocity through the catheter lumen. The growth rate r_t of the coil's size t_c can not directly be related

to the coil's injection velocity (τ_{in}) but also depends on the geometry of the aneurysm. To derive the growth rate r_t, this thesis proposes to adapt a geometric coil deployment algorithm from literature, as touched upon in Section 2-2 [27]. While this geometric algorithm does not provide any information on contact forces, it can give a solid estimate of the trajectory of a deployed coil. The adapted geometric coil algorithm is described in Algorithm 2 in Appendix A-1. This algorithm predicts the trajectory of an endovascular coil with a helical tertiary shape by resolving collisions with the aneurysm wall and itself. The resulting predicted trajectory in a saccular, i.e. convex, aneurysm geometry, is illustrated in Figure 2-10. Given this predicted trajectory, the rate of change (r_t) of the coil's size (t_c) can be described along the length of the aneurysm sac. Figure 2-11 shows the growth rate (r_t) for the injection velocity $\tau_{in} = 5$ mm/s. It can be observed from this figure that the coil growth rate along the length of the aneurysm sac increases when the aneurysm's diameter decreases. Given the geometry of the aneurysm, which can be extracted before the procedure through 3D reconstruction angiography, the presented coil deployment algorithm provides a map between coil injection rate τ_{in} and growth rate r_t.

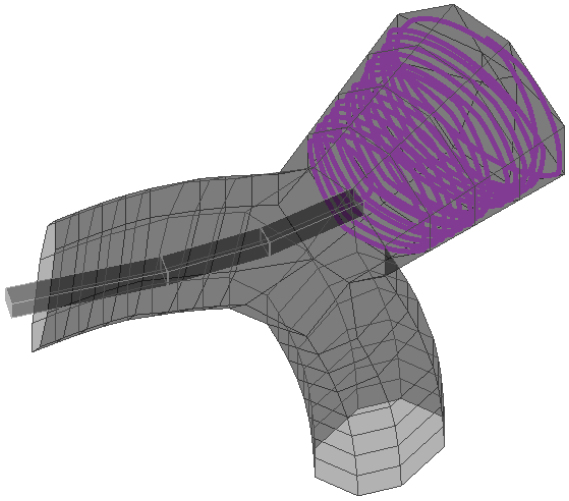

Figure 2-10: 3D illustration of a coiled intracranial aneurysm using the geometric coil modelling approach described in Appendix A-1.

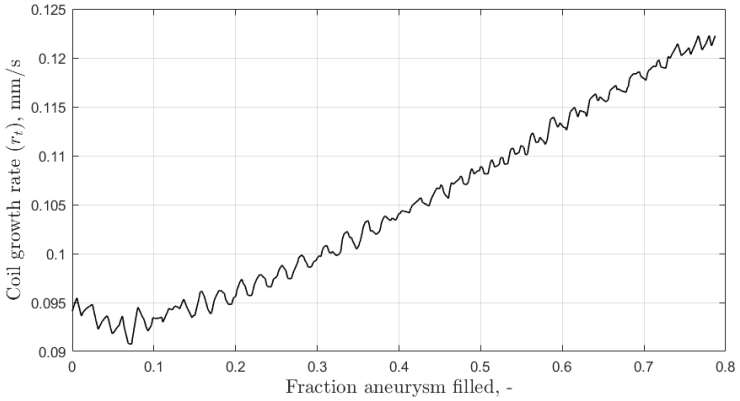

Figure 2-11: Growth rate in longitudinal direction of the coil's helical structure depicted Figure 2-10 in millimeters per second for a constant injection rate $\tau_{in} = 5$ mm/s.

2-4 Discussion

To summarize, this chapter has presented a new dynamic coil deployment model for intracranial aneurysm treatment. The main advantage of this model is its low computational complexity allowing real-time control computation. Section 2-1 has derived the Lagrangian equations of motion for a tendon-driven steerable catheter tip based on the PRB nR representation. It has been explained in Section 2-2 that endovascular coil models from literature are either highly computationally expensive or do not take applied forces into account. Section 2-2 has therefore presented a new way to dynamically model an endovascular coil by exploiting the coil's structure and elasticity and deriving its interaction with a microcatheter and the aneurysm wall. Section 2-3 has combined the catheter and coil model and has proposed to extend this system with the coil's mass (m_c) and size (t_c) as quasi-static growth parameters. This has yielded two decoupled systems in Eq. (2-34) that resemble a coil deployment procedure. The computation of the coil's helix growth rate r_t has been presented by adapting a geometric deployment algorithm from literature [27]. Various simplifying assumptions have been made throughout this chapter. In the following paragraphs, these modelling choices are disucssed in more detail.

To start with, the assumption has been made that the steerable microcatheter tip bends in a single plane, and thus modelling in two dimensions is sufficient. This is a viable assumption for structures with a large length-to-diameter ratio. In this case, bending moments, that work on the catheter tip, are so much larger than torsional effects that the latter can be neglected [38, 28]. To minimize torsional effects, it is required that the contact force vector from the aneurysm wall lies along the bending plane of the microcatheter tip. Before starting the coil deployment procedure, the operator can manually adjust the catheter's roll around the constant angle q_0, and thus can control the bending plane angle (φ) illustrated in Figure 2-3. The catheter's bending plane can then be aligned with the orthogonal vector pointing from the contact point (x_e, y_e) to achieve in-plane bending. It should be noted that (out-of-plane) disturbances have been neglected in the derived system model. While viscous friction has been incorporated in the catheter and coil models, detailed blood flow effects have been omitted. It can be assumed that blood flow disturbance is minimal inside the aneurysm sac [18]. Furthermore, the reaction force of the coil leaving the tip of the catheter could have effects on the catheter's motion. The effect of this force is unknown and has not been considered in this thesis.

Throughout this thesis, it is assumed that the direction q_0 of the base of the steerable microcatheter tip (Figure 2-4) is constant. The interventional neuroradiologist navigates the catheter through the brain vasculature. Upon reaching the aneurysm, the catheter's base orientation (q_0) is determined by the geometry of the neighbouring vessel [18]. The angle q_0 cannot actively be controlled by the operator. Moreover, it is assumed that the deviations of q_0, due to applied forces on the catheter tip, are negligible in comparison to the changes in the joint angles ($q_{1:n}$) of the steerable microcatheter tip.

Regarding the modelling of the coil, it should also be noted that the presented coil deployment model applies to helically shaped coils. This only slightly limits applicability, as most saccular aneurysms can be filled with helically shaped coils [18]. It should also be noted that the coil's stiffness k_c is assumed not to change over time. This excludes the possibility that the blood will already clot during the procedure, hence stiffening the coil structure. Lastly, it should be

noted that this thesis focuses on the contact forces working along the length of the helical coil structure and neglects radial forces exerted on the walls of the aneurysm. When appropriately sized coils are chosen, these forces are not supposed to yield the aneurysm wall.

At the end of this chapter, it has been proposed to estimate the growth rate (r_t) of the coil size (t_c) by exploiting the aneurysm's geometry. Throughout this thesis, a constant growth rate (r_t) is taken to make sure that coil deployment simulations are unambiguous. However, Section 2-3-2 serves as a proof of concept that a variable growth rate can easily be computed and incorporated.

In the remainder of this thesis, a control architecture is presented that enables regulation of the contact force between the coil and the aneurysm wall. Chapter 3 discusses the controller design for the case where no new coil is injected into the aneurysm. Chapter 4 extends this design to the actual situation where coil deployment takes place and where constraints imposed by the equipment and the environment should be obeyed.

Chapter 3

Contact force control

This chapter aims to regulate the contact force between an endovascular coil and the aneurysm wall. Key assumptions in this chapter are that no coil growth takes place and that the base position and orientation of the catheter are fixed in space. Based on the derived model in Chapter 2, Section 3-1 describes the system equations for a fully actuated catheter with two degrees of freedom. Section 3-2 presents this chapter's control objective for which a control architecture, comprising an augmented energy-shaping controller, is proposed in Section 3-3. Numeric proof is presented through simulations in Section 3-4. Methodology and results are discussed in Section 3-5.

3-1 Model description

This section presents the dynamic model for the system setting illustrated in Figure 3-1. The environment is modelled as a conically shaped aneurysm for which a helically shaped filling coil is the obvious choice. The steerable microcatheter is modelled as a Pseudo-rigid Body (PRB) 2R robot model based on Section 2-1-3. This model choice, consisting of three rigid links connected by two revolute joints and two rotational springs, allows for inverse calculation from the tip position (x_t, y_t) to the joints angles $q := (q_1, q_2)$. This property is shown to be useful in Section 3-2. The system is described by the generalized coordinate vector $\psi := (q_1, q_2, q_c)$, where q_c is the distance from the point (x_t, y_t) to the coil's centre of mass (x_c, y_c) along the line to the wall contact point (x_e, y_e). According to Eq. (2-27), the system's centres of mass ξ can be fully described with the generalized coordinate vector ψ, that is

$$\xi = T(\psi) = \begin{bmatrix} x_0 + \cos q_0 \ell + \cos q_1 \frac{\ell}{2} \\ y_0 + \sin q_0 \ell + \sin q_1 \frac{\ell}{2} \\ q_1 \\ x_0 + (\cos q_0 + \cos q_1)\ell + \cos q_2 \frac{\ell}{2} \\ y_0 + (\sin q_0 + \sin q_1)\ell + \sin q_2 \frac{\ell}{2} \\ q_2 \\ x_t + q_c(x_e - x_t)/\left|\left|(x_e, y_e) - (x_t, y_t)\right|\right| \\ y_t + q_c(y_e - y_t)/\left|\left|(x_e, y_e) - (x_t, y_t)\right|\right| \end{bmatrix}, \text{ with } \xi = \begin{bmatrix} x_1 \\ y_1 \\ \varphi_1 \\ x_2 \\ y_2 \\ \varphi_2 \\ x_c \\ y_c \end{bmatrix}, \tag{3-1}$$

where identical link lengths ℓ and masses m are chosen to compactly represent the derived equations and system matrices. The base position (x_0, y_0) and direction q_0 of the steerable microcatheter tip are considered constant in this chapter. As discussed in Appendix B-3, their values can be measured using X-ray segmentation at the start of the procedure. Lastly, the coil's centre of mass (x_c, y_c) has been derived in Eq. (2-18), and the catheter's tip position (x_t, y_t) is described with the map $h(q)$ as

$$\begin{bmatrix} x_t \\ y_t \end{bmatrix} = h(q) = \begin{bmatrix} x_0 + (\cos q_0 + \cos q_1 + \cos q_2)\ell \\ y_0 + (\sin q_0 + \sin q_1 + \sin q_2)\ell \end{bmatrix}. \tag{3-2}$$

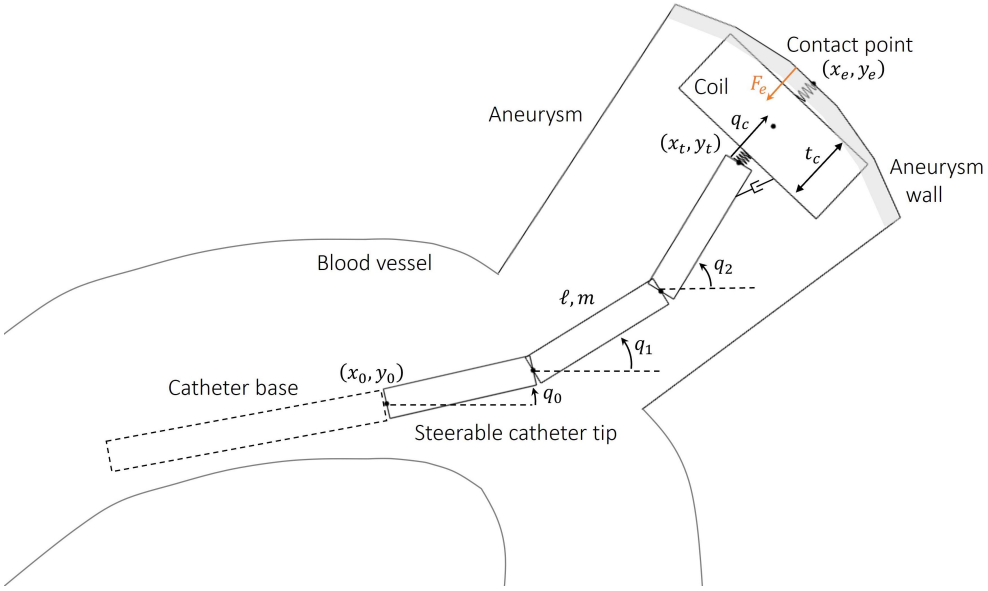

Figure 3-1: Catheter-coil-aneurysm system with constant (x_0, y_0), q_0 and t_c.

This chapter assumes that the steerable catheter tip consists of two tendon-driven bending sections whose bending torques can be independently actuated at their virtual joints, i.e. $Q = [\tau_1 \quad \tau_2]^T$. The discussion in Section 3-5 elaborates on this modelling choice. The equations of motion, corresponding to Figure 3-1, follow from Eq. (2-28), that is

$$M(\psi)\begin{bmatrix} \ddot{q} \\ \ddot{q}_c \end{bmatrix} + C(\psi, \dot{\psi})\begin{bmatrix} \dot{q} \\ \dot{q}_c \end{bmatrix} + \begin{bmatrix} K_\Delta & 0 \\ 0 & k_c \end{bmatrix}\begin{bmatrix} q \\ q_c - \frac{t_c}{2} \end{bmatrix} + k_e\delta\begin{bmatrix} \partial\delta/\partial q \\ 1 \end{bmatrix} + \begin{bmatrix} D_\Delta & 0 \\ 0 & d_c \end{bmatrix}\begin{bmatrix} \dot{q} \\ \dot{q}_c \end{bmatrix} + \begin{bmatrix} g(q) \\ 0 \end{bmatrix} = \begin{bmatrix} Q \\ 0 \end{bmatrix}, \tag{3-3}$$

where the system matrices are defined as

$$M(\psi) := \left(\frac{\partial T_\psi(\psi)}{\partial \psi}\right)^T M \frac{\partial T_\psi(\psi)}{\partial \psi}, \quad C(\psi, \dot{\psi}) := \left(\frac{\partial T_\psi(\psi)}{\partial \psi}\right)^T M \frac{\partial^2 T_\psi(\psi)}{\partial \psi^2}\dot{\psi}, \tag{3-4}$$

$$M = \begin{bmatrix} I_2 m & 0 \\ 0 & m_c \end{bmatrix}, \quad K_\Delta = \begin{bmatrix} 2k & -k \\ k & -k \end{bmatrix}, \quad \beta(q_0) = \begin{bmatrix} -kq_0 \\ 0 \end{bmatrix}, \quad D_\Delta = \begin{bmatrix} 2d & -d \\ d & -d \end{bmatrix}, \tag{3-5}$$

where K_Δ and D_Δ are stiffness and damping matrices for the rotational catheter springs, k_c and d_c are the stiffness and damping coefficient of the coil with respect to the catheter, k_e is the stiffness of the aneurysm wall and δ is the indentation depth of the coil in the aneurysm wall as defined in Eq. (2-25).

3-2 Control objective

This section defines the chapter's force regulation objective and shows equivalence and uniqueness of control objectives for the catheter's tip position (x_t, y_t) and the catheter's joint angles (q_1, q_2).

3-2-1 Contact force objective

The goal is to regulate the states $\psi = (q_1, q_2, q_c)^T$ of the dynamic system in Eq. (3-3) such that the contact force (F_e) between the coil and the aneurysm wall, i.e.

$$F_e = \begin{cases} k_e\delta & \delta \leq 0 \\ 0 & \delta > 0 \end{cases}, \tag{3-6}$$

asymptotically converges to a predefined desired contact force $(F_e^\star)$, where δ and k_e are respectively the indentation between the coil and the aneurysm wall, as defined in Eq. (2-25), and the stiffness of the aneurysm wall. As discussed in Section 2-2-1, an estimate can be found for the maximum force $(F_{e,max})$ and its related indentation depth (δ_{max}) that would yield the aneurysm wall. The reference force $(F_e^\star)$ is chosen by the operator with a safe margin below $F_{e,max}$. The regulatory control problem for F_e is then denoted as

$$\lim_{t\to\infty} \tilde{F}_e = 0, \quad \text{with} \quad \tilde{F}_e := F_e^\star - F_e. \tag{3-7}$$

It is impossible to measure the tension on the aneurysm wall. While force sensors have been designed for medical equipment, these sensors are too bulky and would block the coil from being deployed in the aneurysm [46]. Therefore, this thesis derives control objectives that are unique and equivalent to the force regulation objective in Eq. (3-7). This derivation is based on the the contact illustration in Figure 3-2.

3-2-2 Tip position objective

First, it can be noted from Figure 3-2 that the two coil-attached springs are loaded in the same direction, and thus can be considered as a single spring with a compression $\Delta L := \delta + \Delta\ell$. The desired reference force $(F_e^\star)$ can then uniquely be defined by the desired compression, i.e.

$$\Delta L^\star = F_e^\star \left(\frac{1}{k_e} + \frac{1}{k_c}\right) \quad \text{with} \quad \Delta L^\star = \delta^\star + \Delta\ell^\star, \tag{3-8}$$

where k_c and k_e are the coil's and aneurysm's stiffness coefficients. Given that the contact force F_e is controlled orthogonal to the contact plane (Figure 3-2), the desired compression $\Delta L^\star$ can uniquely be described by the desired catheter tip position $(x_t^\star, y_t^\star)$, that is

$$\begin{bmatrix} x_t^\star \\ y_t{}^\star \end{bmatrix} = \begin{bmatrix} x_e \\ y_e \end{bmatrix} - (\Delta L^\star + t_c + \Delta\ell_0 + \delta_{max})\boldsymbol{n}_\perp, \quad \text{with} \quad \boldsymbol{n}_\perp = \begin{bmatrix} 0 & -1 \\ 1 & 0 \end{bmatrix} \boldsymbol{n}, \tag{3-9}$$

where $\boldsymbol{n}_\perp$ is a unit vector perpendicular to the contact plane vector $\boldsymbol{n}$ [47] and can be determined prior to the treatment using a 3D reconstruction angiogram (Figure B-1). The

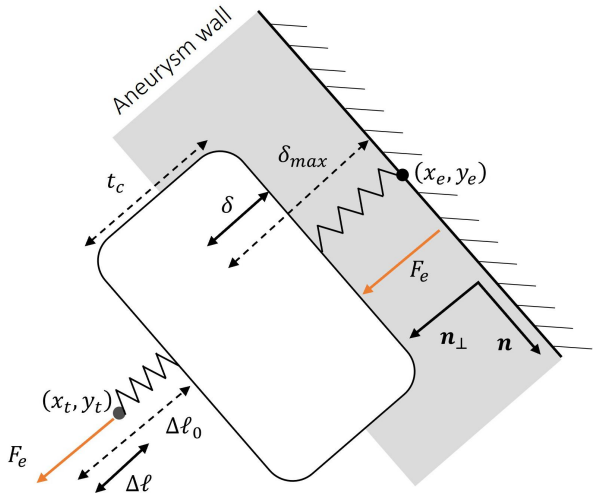

Figure 3-2: Illustration of contact force propagation from aneurysm wall to catheter tip.

parameter $\Delta\ell_0$ is the base length of the spring between the coil and the catheter and is introduced for ease of illustration. Parameter δ_{max} is the depth of contact point (x_e, y_e) in the aneurysm wall and corresponds to the maximum allowable force $(F_{e,max})$. Parameter t_c is the size of the helical coil structure and is considered to be constant in this chapter as coil growth is assumed not to take place. Given Eq. (3-9), the control objective in Eq. (3-7) is equivalent to

$$\lim_{t\to\infty} \tilde{x} = 0, \quad \text{with} \quad \tilde{x} := \begin{bmatrix} x_t^\star \\ y_t^\star \end{bmatrix} - \begin{bmatrix} x_t \\ y_t \end{bmatrix}. \tag{3-10}$$

3-2-3 Joint objective

It is then noted that, given that there exists a unique inverse mapping $h^{-1}(x)$ from (x_t, y_t) to (q_1, q_2), the desired joints angles $(q_1^\star, q_2^\star)$ can be uniquely defined by $(x_t^\star, y_t^\star)$. This yields the following objective,

$$\lim_{t\to\infty} \tilde{q} = 0, \quad \text{with} \quad \tilde{q} := h^{-1}\left(\begin{bmatrix} x_t^\star \\ y_t^\star \end{bmatrix}\right) - \begin{bmatrix} q_1 \\ q_2 \end{bmatrix}, \tag{3-11}$$

which is equivalent to the objectives in Eq. (3-10) and Eq. (3-7). It can be verified that the mapping $h^{-1}(x)$ is the unique inverse of mapping $h(q)$ in Eq. (3-2) by using basic geometry [48], i.e.

$$h^{-1}\left(\begin{bmatrix} x_t \\ y_t \end{bmatrix}\right) = \begin{bmatrix} q_1 \\ q_1 + \Delta q \end{bmatrix} \tag{3-12}$$

where the angles q_1 and Δq are defined as

$$\begin{aligned} \Delta q &= \text{sign}(d) \left| \arccos\left(\frac{\Delta x_t^2 + \Delta y_t^2}{2\ell^2} - 1 \right) \right|, \\ q_1 &= \arctan\left(\frac{\Delta y}{\Delta x}\right) - \arctan\left(\frac{\sin\Delta q}{1+\cos\Delta q}\right)\text{sign}(d), \end{aligned}$$

and the auxiliary variables $\Delta x, \Delta y$ and d defined as

$$\begin{aligned} \Delta x &= x_t^\star - \cos q_0 - x_0, \\ \Delta y &= y_t^\star - \sin q_0 - y_0, \\ d &= x_t^\star \sin q_0 - y_t^\star \cos q_0, \end{aligned}$$

where the variable d constrains the catheter to have a single bend and is defined to assure uniqueness of the mapping $h^{-1}(x)$. When $q_2 \geq q_1$, the catheter tip bends counterclockwise and with $q_2 \leq q_1$, the catheter tip makes a clockwise turn. The discussion in Section 3-5 elaborates on this modelling choice. To summarize, the control objectives are related as

$$\lim_{t\to\infty} \tilde{q} = 0 \implies \lim_{t\to\infty} (\tilde{x}_t, \tilde{y}_t) = 0 \implies \lim_{t\to\infty} \tilde{F}_e = 0. \tag{3-13}$$

Note that generalized coordinate q_c does not appear in these control objectives. According to the definition of $\Delta\ell$ in Eq. (2-19) and of ΔL in Eq. (3-8), the steady-state value $q_c{}^\star$ is uniquely defined as

$$q_c^\star = \frac{k_e}{k_e + k_c}\Delta L^\star + \frac{t_c}{2}. \tag{3-14}$$

Based on Eq. (3-13), a control architecture can be defined to regulate the contact force (F_e) between the coil and the aneurysm wall through regulation of the joint angles (q_1, q_2).

3-3 Controller design

This section presents a control architecture (Figure 3-3) that drives the contact force (F_e) between the coil and the aneurysm wall to the desired reference state $(F_e^\star)$ through regulation of joint angles (q_1, q_2) to $(q_1^\star, q_2^\star)$. This entails the design of an augmented energy shaping controller which closes the system loop by generating tendon torques (τ_1, τ_2). On the left of Figure 3-3, computations are depicted that are executed prior to treatment and stored in a local data store. This entails computation of $(x_t^\star, y_t^\star)$ as in Eq. (3-9), computation of $(q_1^\star, q_2^\star)$ as in Eq. (3-12) and measurement of q_0. The right side of Figure 3-3 represents the closed-loop system. Joint angles (q_1, q_2) are feedback signals measured using Fibre Bragg Grating (FBG) sensors. The wall contact force (F_e) is the output of the system. The following sections discuss the design of the augmented energy shaping controller and show that this controller asymptotically stabilizes the system at the desired equilibrium.

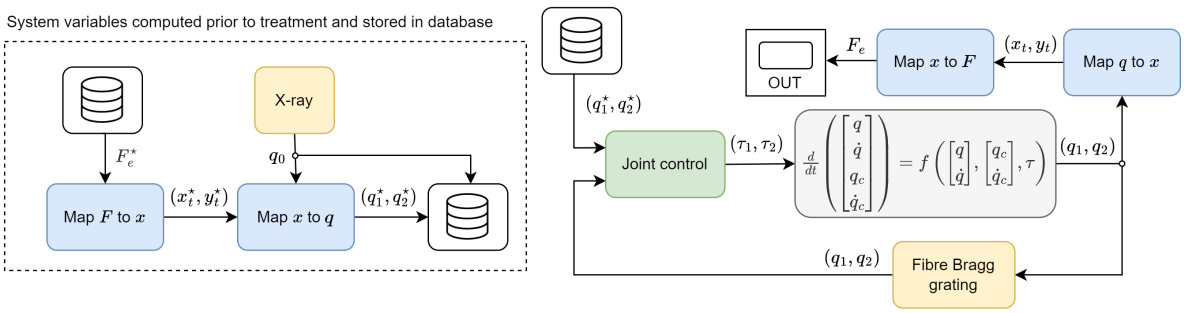

Figure 3-3: Control architecture for a non-developing coil system.

3-3-1 Free space joint control

This section discusses a controller that steers the catheter tip joint angles (q_1, q_2) to their desired setpoint $(q_1^\star, q_2^\star)$ given that the system is unforced, i.e. no contact takes place between the coil and the aneurysm wall. Exploiting the theory on passivity-based control in Appendix B-2, this can be achieved by placing the system equilibrium $(\bar{q}_1, \bar{q}_2)$ of Eq. (3-3) at the desired angles $(q_1^\star, q_2^\star)$. For a fully-actuated steerable microcatheter tip, this boils down to shaping the potential energy of the system, i.e. the catheter's elastic and gravitational energy [31]. Given the dynamics in Eq. (3-3) a movement in free space, the control input Q_{free} should take the following form, i.e.

$$Q_{free} = K_\Delta q^\star + \beta(q_0) + g(q^\star), \tag{3-15}$$

which is similar to a classical Proportional (P) controller with gravity pre-compensation [41]. The first two terms place the elastic energy of the catheter's rotational joints at the desired equilibrium $(q_1^\star, q_2^\star)$ while the term $g(q^\star)$ compensates for the gravitational energy of the system. Note that the gravitational energy is dominated with $g(q^\star)$ instead of cancelled with $g(q)$ to avoid robustness problems due to unmodelled dynamics or uncertainties [31, 45]. Note that, given a constant catheter base angle q_0 and position (x_0, y_0), Q_{free} is a feed-forward control gain that does not require online computation.

3-3-2 Contact joint control

The energy shaping controller in Eq. (3-15) considers the system to be unforced. This is not the case when contact is made between the coil and the environment. It is proposed in this thesis to design a control action such that a system in contact appears to be unforced. This is done by the computation and cancellation of the force vector exerted by the coil on the catheter tip. By combining Eq. (3-2) and Eq. (3-9), this force vector takes the following form,

$$\begin{bmatrix} f_x \\ f_y \end{bmatrix} = \frac{\Delta L}{(\Delta L + t_c + \Delta\ell_0 + \delta_{max})(\frac{1}{ke} + \frac{1}{kc})} \left(\begin{bmatrix} x_e \\ y_e \end{bmatrix} - h(q) \right). \tag{3-16}$$

This force vector can be projected on the microcatheter joints (q_1, q_2) using the system Jacobian $J(q)$, that is

$$Q_F = J(q)^T \begin{bmatrix} f_x \\ f_y \end{bmatrix}, \quad J(q) := \frac{\partial h(q)}{\partial q}, \tag{3-17}$$

with $h(q)$ defined in Eq. (3-2). It should be noted that one can safely reject these tip forces as it has been verified in Eq. (3-13) that joint positions $(q_1^\star, q_2^\star)$ will yield the desired contact force $F_e^\star$ between the coil and the aneurysm wall. While direct cancellation of terms should be avoided [31], this method seems to be a viable option when good estimates on the coil and aneurysm properties are available. The resulting control action, i.e.

$$Q = Q_F + Q_{free} = K_\Delta q^\star + \beta(q_0) + g(q^\star) + J(q)^T \begin{bmatrix} f_x \\ f_y \end{bmatrix}, \tag{3-18}$$

is a combined feedback and feed-forwardward controller. This controller is denoted in block diagram form in Figure 3-4 and corresponds to the joint control block in the control architecture (Figure 3-3). By combing the feedback action in Eq. (3-18) and the open loop system in

Eq. (2-31), the closed-loop dynamics take the following explicit form,

$$\begin{aligned}\dot{\tilde{\psi}} &= -\dot{\psi},\\ \ddot{\psi} &= -M(\psi)^{-1}\left(C(\psi,\dot{\psi})\dot{\psi} + \begin{bmatrix}-K_\Delta & 0 & 0\\ 0 & k_c & -k_e\end{bmatrix}\begin{bmatrix}\tilde{q}\\ \tilde{\Delta\ell}\\ \tilde{\delta}\end{bmatrix} + \begin{bmatrix}D_\Delta & 0\\ 0 & d_c\end{bmatrix}\begin{bmatrix}\dot{q}\\ \dot{q}_c\end{bmatrix} + \begin{bmatrix}g(q)-g(q^\star)\\ 0\end{bmatrix}\right),\end{aligned} \tag{3-19}$$

with $\tilde{\psi}$ and sort-like variables denoting error signals with respect to the reference values $\psi^\star$. The following section will show that $(\tilde{\psi},\dot{\psi}) = (0,0)$ is an asymptotically stable equilibrium of the closed-loop system in Eq. (3-19), i.e. the contact force between the coil and the aneurysm wall will asymptotically reach its desired value.

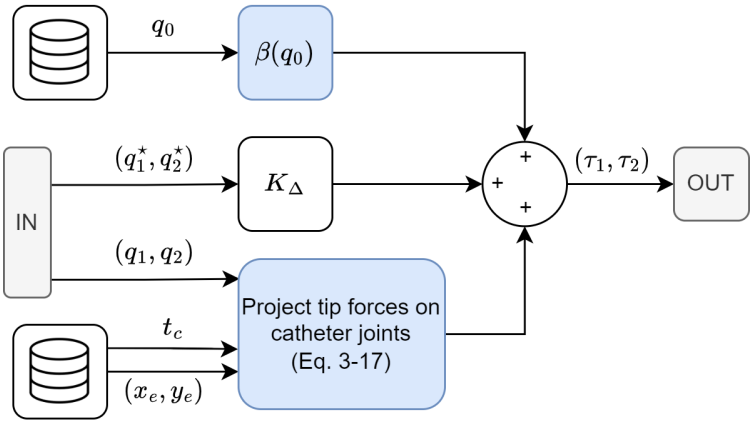

Figure 3-4: Joint control block diagram based on Eq. (3-18) and corresponding to Figure 3-3. The catheter base angle q_0, contact point (x_e, y_e) and the coil's helix length t_c are computed prior to treatment and stored in a local database.

3-3-3 Stability analysis

This section shows through stability analysis that the proposed controller in Eq. (3-18) asymptotically drives the joint angles (q_1, q_2) to their desired value $(q_1^\star, q_2^\star)$, given that no coil growth takes place. It has been shown in Section 3-2 that this objective is equivalent to guiding the contact force force (F_e) to its desired value $(F_e^\star)$. This section uses notions of Lyapunov stability and LaSalle's invariance principle as defined in Appendix B-1.

Theorem 3.1 Consider the system in Eq. (3-3), with the controller in Eq. (3-18). The catheter joint error in Eq. (3-11), the tip position error in Eq. (3-10) and the force error in Eq. (3-7) are globally asymptotically stable, that is

$$(||\tilde{q}|| \to 0 \wedge |\tilde{q_c}| \to 0) \implies ||\tilde{x}|| \to 0 \implies |\tilde{F_e}| \to 0, \quad as \quad t \to \infty, \tag{3-20}$$

provided that

$$\lambda_m\{K_\Delta\} \geq k_g \quad \text{and} \quad d, d_c > 0 \tag{3-21}$$

hold, where $\lambda_m\{.\}$ denotes the eigenvalue operator and k_g is defined in Property 3.4.

Proof 3.1 Take the following Lyapunov candidate, i.e.

$$V(\tilde{q},\dot{q},\tilde{q_c},\dot{q_c}) = \underbrace{\frac{1}{2}\dot{\psi}^T M(q)\dot{\psi}}_{\boldsymbol{A}} + \underbrace{\frac{1}{2}\tilde{q}^T K_\Delta \tilde{q} + G(q) - G(q^\star) + g(q^\star)^T\tilde{q}}_{\boldsymbol{B}} + \underbrace{\frac{1}{2}k_c\tilde{\Delta}\ell^2 + \frac{1}{2}k_e\tilde{\delta}^2}_{\boldsymbol{C}} \quad (3\text{-}22)$$

which should be proven to be continuously differentiable, radially unbounded, positive definite for all nonzero $(\psi,\dot{\psi})$ and equal to zero for $(\psi,\dot{\psi}) = (0,0)$. These properties are reviewed separately for underlined terms $\boldsymbol{A}$, $\boldsymbol{B}$ and $\boldsymbol{C}$.

- ***A.*** This quadratic term is continuously differentiable and zero for $(\psi,\dot{\psi}) = (0,0)$. According to Property 3.4, $M(q)$ is positive definite, hence term $\boldsymbol{A}$ is positive definite for $(\tilde{\psi},\dot{\psi}) \neq 0$ and radially unbounded.

- ***B.*** In this term, $G(q)$ denotes the gravitational energy and $g(q)$ denotes its partial derivative with respect to q. Both $g(q)$ and $G(q)$ are constructed from sinusoids, hence are continuously differentiable. It can be verified that $\boldsymbol{B}$ equals zero for $(\tilde{q},\dot{q}) = (0,0)$. To show positive definiteness, one needs to show that its Hessian, i.e.

$$\frac{\partial^2 B(\tilde{q})}{\partial q^2} = K_\Delta + \frac{\partial g(q)}{\partial q}, \quad (3\text{-}23)$$

  is positive definite [41]. With the assumption that K_Δ is positive definite, i.e. $k > 0$, one has the following condition,

$$\lambda_m\{K_\Delta\} > \left|\left|\frac{\partial g(q)}{\partial q}\right|\right|, \quad (3\text{-}24)$$

  which is satisfied, according to Property 3.4, when $\lambda_m\{K_\Delta\} > k_g$. This physically means that the catheter should be stiff enough to carry its own weight.

- ***C.*** These quadratic terms are clearly radially unbounded. It can be verified that term $\boldsymbol{C}$ is zero at $q_c = q_c{}^\star$ with q_c denoted as in Eq. (3-14). The terms in $\boldsymbol{C}$ are non-negative for $\psi \neq 0$. Note that the term $\tilde{\delta}^2$ is not continuously differentiable at $\delta = 0$, i.e. continuous differentiability is only assured when contact is sustained during the control action.

The time derivative of $V(\tilde{q},\dot{q},\tilde{q_c},\dot{q_c})$ takes the following form, i.e.

$$\begin{aligned}
\dot{V}(\tilde{q},\dot{q},\tilde{q_c},\dot{q_c}) &= \tfrac{1}{2}\ddot{\psi}^T M(q)\dot{\psi} + \tfrac{1}{2}\dot{\psi}^T\dot{M}(q)\dot{\psi} + \tfrac{1}{2}\dot{\psi}^T M(q)\ddot{\psi} + -\dot{q}^T K_\Delta\tilde{q} + \dot{q}^T g(q) - \dot{q}^T g(q^\star) \\
&\quad + \dot{q_c}^T\left[k_c\tilde{\Delta}\ell(q_c) - k_e\tilde{\delta}(q^\star,q_c)\right] \\
&= \tfrac{1}{2}\dot{\psi}^T(\dot{M} - C^T - C)\dot{\psi} - \dot{\psi}^T\left(\begin{bmatrix} -K_\Delta\tilde{q} \\ k_c\tilde{\Delta}\ell - k_e\tilde{\delta}\end{bmatrix} + \begin{bmatrix} D_\Delta\dot{q} \\ d_c k_c\end{bmatrix} + \begin{bmatrix} g(q) - g(q^\star) \\ 0\end{bmatrix}\right) \\
&\quad - \dot{q}^T K_\Delta\tilde{q} + \dot{q}^T g(q) - \dot{q}^T g(q^\star) + \dot{q_c}^T\left[k_c\tilde{\Delta}\ell(q_c) - k_e\tilde{\delta}(q^\star,q_c)\right] \\
&= -\dot{\psi}\begin{bmatrix} D_\Delta & 0 \\ 0 & d_c\end{bmatrix}\dot{\psi},
\end{aligned} \quad (3\text{-}25)$$

where Property 3.4 is employed to cancel term $M - C - C^T$. The function $\dot{V}(\tilde{q},\dot{q},\tilde{q_c},\dot{q_c})$ is negative semidefinite when $D_\Delta > 0$ and $d_c > 0$. Note from Eq. (3-4) that $D_\Delta > 0$ is satisfied

for all $d > 0$. By invoking Lyapunov's direct method, one can conclude that the origin of the state space, i.e. $(\tilde{\psi}, \dot{\psi}) = (0, 0)$, is a stable equilibrium of the closed-loop system denoted in Eq. (3-19). One can then exploit LaSalle's invariance principle to show that the set,

$$\Omega = \{\begin{bmatrix}\tilde{\psi}^T & \dot{\psi}^T\end{bmatrix}^T \in \mathbb{R}^{2n} : \dot{V}(\tilde{\psi}, \dot{\psi}) = 0\}, \tag{3-26}$$

consists only of the origin of the state space, i.e. $(\tilde{\psi}^T \dot{\psi}^T) = (0, 0)$. Hence, it is concluded that the origin is a globally asymptotically stable equilibrium of the closed-loop system in Eq. (3-19) [41].

3-4 Simulations

To validate the theoretic proof in Section 3-3-3, this section shows through numeric simulation that the joint control objective in Eq. (3-13) is achieved. This implies that the contact force F_e between an endovascular coil and the aneurysm wall is regulated at the desired value $F_e^\star$ given that no coil growth takes place, i.e. the coil has constant properties.

The environment has been simulated according to Figure 4-1 and control has been implemented according to the control architecture in Figure 3-3. The chosen system parameters are summarized in Table 3-1. The catheter parameters have been chosen based on simulation without a coil and aneurysm. Subsequently, the coil and aneurysm parameters have been chosen relative to these catheter parameters. Note from Table 3-1 that the condition $k > k_g$ is preserved to ensure the asymptotic stability of **Theorem 3.1**. The desired contact force between the coil and the aneurysm is chosen as half the maximum force, i.e. $F_e^\star := 0.5F_{e,max} = -0.1\text{N}$, with $F_{e,max}$ chosen based on the order of magnitude of the other system parameters in Table 3-1.

The relevant system outputs have been presented in Figures 3-5 to 3-7. It can be observed from Figure 3-5 that the contact force F_e has successfully been stabilized at its desired value $F_e^\star$. It can also be noted from Figures 3-6 and 3-7 that the relationship in Eq. (3-13) has been verified as auxiliary output variables (x_t, y_t) and (q_1, q_2) achieve their desired values. During stabilization, F_e does not reach its maximal force threshold $F_{e,max} = -0.2N$. Hence, the aneurysm wall did not yield.

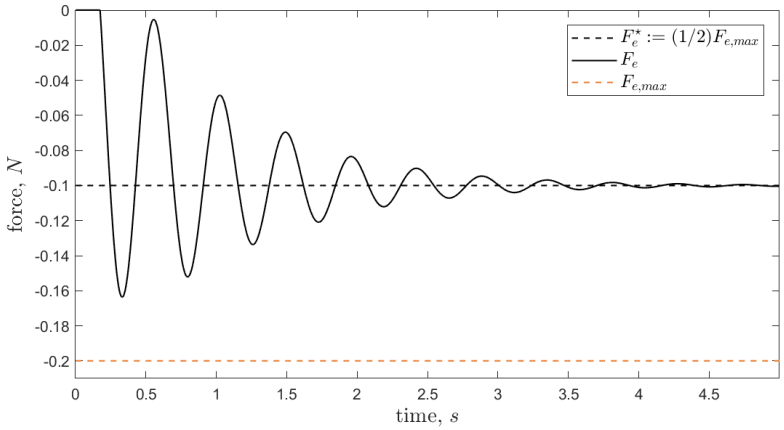

Figure 3-5: Contact force regulation in non-deployment case.

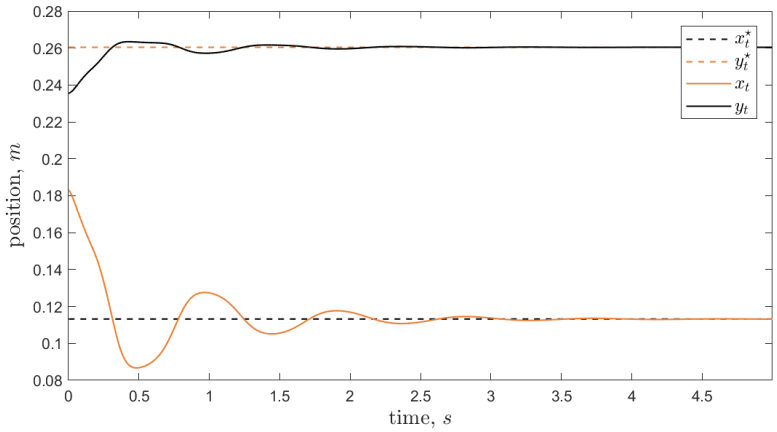

Figure 3-6: Catheter tip position regulation in non-deployment case.

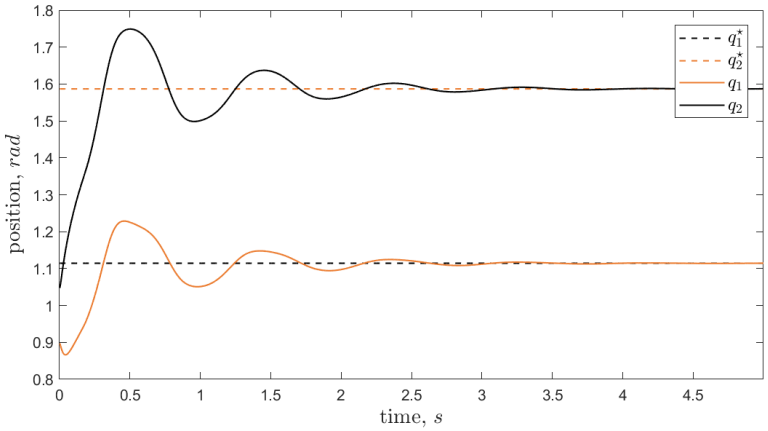

Figure 3-7: Catheter joint angle regulation in non-deployment case.

Variable	Description	Value	Unit
State parameters			
$q(0)$	Joint angles at $t = 0$	$(\frac{\pi}{3.5}, \quad \frac{\pi}{3})$	rad
$\dot{q}(0)$	Joint velocities at $t = 0$	$(0, \quad 0)$	rad/s
$q_c(0)$	Relative coil position at $t = 0$	$\Delta\ell_0 + \frac{t_c}{2}$	m
$\dot{q_c}(0)$	Coil velocity at $t = 0$	0	m/s
q_0	Catheter base angle	$\frac{\pi}{4}$	rad
(x_0, y_0)	Catheter base pose	0	m
Catheter properties			
γ	Characteristic lengths	$(\frac{1}{3}, \quad \frac{1}{3}, \quad \frac{1}{3})$	-
κ	Characteristic stiffness	$(2, \quad 2)$	-
L	Length	0.3	meter
m	Mass	0.04	kg
E	Young's modulus	50	kg/ms^2
k	Joint stiffness	$\frac{\kappa ELm}{12} (= 0.1)$	kg m/s^2
k_g	Supremum gravity Hessian	0.0981	-
d	Damping coefficient	$(4, \quad 4) \times 10^{-3}$	kg
Coil properties			
m_c	Mass	0.08	kg
t_c	Coil's helix length	0.05	meter
k_c	Catheter-coil stiffness	6	kg/s^2
d_c	Coil damping coefficient	0.2	kg/s
$\Delta\ell_0$	Catheter-coil rest length	0.025	m
δ_{max}	Maximal wall indentation	0.025	m
Aneurysm properties			
k_e	Wall stiffness	9	kg/s^2
(x_e, y_e)	Contact point	$(0.127, \quad 0.331)$	m
$\boldsymbol{n}$	Contact plane	$(0.981, \quad 0.195)$	-
Other parameters			
g	Gravitational acceleration	9.81	m/s^2
h	Integration time step	0.001	s
T	Simulation time	5	s
$F_e^\star$	Desired contact force	0.1	N

Table 3-1: Choice of parameters for regulation of the contact force between on a non-developing coil and the aneurysm wall.

3-5 Discussion

To conclude, this chapter has presented a control architecture (Figure 3-3) to guide the contact force (F_e) between a coil and the aneurysm wall to its desired equilibrium ($F_e^\star$) given that no coil growth takes place. It has been shown in Section 3-2 that the objective to guide the joint angles (q_1, q_2) to $(q_1^\star, q_2^\star)$ is unique and equivalent to guiding the contact force (F_e) to $F_e^\star$. Subsequently, an augmented energy-shaping joint controller has been designed in Section 3-3. It has been shown through stability analysis (Section 3-3-3) and numeric simulations (Section 3-4) that the proposed controller asymptotically stabilizes the aneurysm wall tension at the desired value. Throughout this chapter, various simplifying assumptions have been made. In the following paragraphs, these modelling choices are discussed in more detail.

To start with, it has been assumed in this chapter that part of the helical coil has already been deployed in the aneurysm, i.e. $t_c > \alpha$, where α is some positive number and t_c is the size of the coil. The reason for this is that a coil with a small length is presumably hard to control along a single direction. After multiple helical coil loops have been deployed, control can take place along the arising spring-like coil structure visualized in Figure 2-5. The first few coil loops should be manually deployed by the interventional neuroradiologist and are assumed not to apply excessive tension on the aneurysm wall. The operator can then activate the contact force stabilizer as described throughout this chapter.

To assure the uniqueness of the joint control objective in Eq. (3-11), it has been assumed that the catheter only makes a single bend, i.e. the relative joint angles share the same sign. Tendon-driven robots with multiple bending sections have been designed by attaching tendon ends at different fixation points along the length of the steerable section. Combined parallel and diagonal tendon wiring has been used to decouple the actuation between sections. It has, however, been shown that a single-bend catheter suffers less from section coupling [49]. Constraining the catheter to make a single bend, assures the necessary condition that the tendon torques τ_1 and τ_2 can be independently actuated.

Another discussion point is that the wall tension (F_e) in the chosen contact point (x_e, y_e) has been considered to be representable for all pressure points in the aneurysm. While this assumption can only be verified in an experiment, it is a legitimate assumption given the spring-like structure of the coil.

It should also be noted that it has been assumed that perfect sensor measurement are available for the base position (x_0, y_0) and direction q_0 using X-ray segmentation. Moreover, perfect measurements have been assumed for the joint angles (q_1, q_2) based on fibre Bragg grating sensing. Especially errors in measurements of (q_1, q_2) could deteriorate controller performance given that control action Q_F in Eq. (3-17) is based on the direct cancellation of terms. It is thus required that the system includes high-quality sensors and accurate processing software. It should be noted that small deviations in feedback signals would not necessarily result in rupture of the aneurysm wall given the safe margin between $F_e^\star$ and $F_{e,max}$.

Another point worth mentioning is that simulation parameters have mostly been chosen relative to each other, hence do not necessarily represent reality. Due to many necessary assumptions on catheter material, coil properties and patient variability, this thesis serves as a proof of concept instead of a perfect representation of reality.

Regarding the simulation, it can be noted that the contact force F_e in Figure 3-5 overshoots its target position $F_e^\star$ during stabilization. Overshoot can be limited by imposing constraints on catheter joint velocities.

Lastly, it has been assumed that the target tip position $(x_t^\star, y_t^\star)$ was a feasible target for a catheter with a fixed base position (x_0, y_0) and orientation q_0. The next chapter introduces constraints imposed by the aneurysm and the microcatheter. Moreover, the assumptions on constant coil parameters and a fixed base position (x_0, y_0) are relaxed. A control architecture is proposed to preserve the feasibility of the proposed contact force controller during coil deployment.

Chapter 4

Controlled coil deployment

This chapter aims to regulate of the contact force (F_e) between an endovascular coil and the aneurysm wall throughout a coil deployment procedure. In contrast to Chapter 3, coil growth takes place and the catheter's base can move freely along the constant direction q_0. This adds an extra degree of freedom to the system which requires recalculation of the reference positions $(x_t^\star, y_t^\star)$ and joint angles $(q_1^\star, q_2^\star)$ to sustain the desired contact force $(F_e^\star)$. To guarantee the procedure's safety and feasibility, the catheter and environmental constraints are defined in Section 4-2. A control objective is defined in Section 4-3 for which a control architecture is presented in Section 4-4. This comprises the design of an auxiliary controller which exploits the system's extra degree of freedom to preserve the feasibility of the contact force regulation objective in Chapter 3. Numeric proof is presented through simulations in Section 4-5. The methodology and results are discussed in Section 4-6.

4-1 Model description

This section presents the system model which is an extension of the system dynamics in Eq. (3-3). In the actual procedure, the operator can push and pull the catheter's body through the vasculature. It is assumed that the resulting tip movement is constrained to the constant direction q_0 (Figure 4-1). The discussion in Section 2-4 elaborates on this modelling choice. The pushing and pulling manoeuvre adds one degree of freedom, i.e. the displacement of the base of the steerable catheter tip (w) along the direction q_0 and with respect to the initial point (x_0, y_0). The system's centres of mass ξ are described with the map $T(\psi)$, that is

$$\xi = T(\psi) = \begin{bmatrix} x_0 + \cos q_0(\ell + \boldsymbol{w}) + \cos q_1 \frac{\ell}{2} \\ y_0 + \sin q_0(\ell + \boldsymbol{w}) + \sin q_1 \frac{\ell}{2} \\ q_1 \\ x_0 + \cos q_0(\ell + \boldsymbol{w}) + \cos q_1)\ell + \cos q_2 \frac{\ell}{2} \\ y_0 + \sin q_0(\ell + \boldsymbol{w}) + \sin q_1)\ell + \sin q_2 \frac{\ell}{2} \\ q_2 \\ x_t + q_c(x_e - x_t)/\left|\left|(x_e, y_e) - (x_t, y_t)\right|\right| \\ y_t + q_c(y_e - y_t)/\left|\left|(x_e, y_e) - (x_t, y_t)\right|\right| \end{bmatrix}, \text{ with } \begin{bmatrix} x_1 \\ y_1 \\ \varphi_1 \\ x_2 \\ y_2 \\ \varphi_2 \\ x_c \\ y_c \end{bmatrix}, \tag{4-1}$$

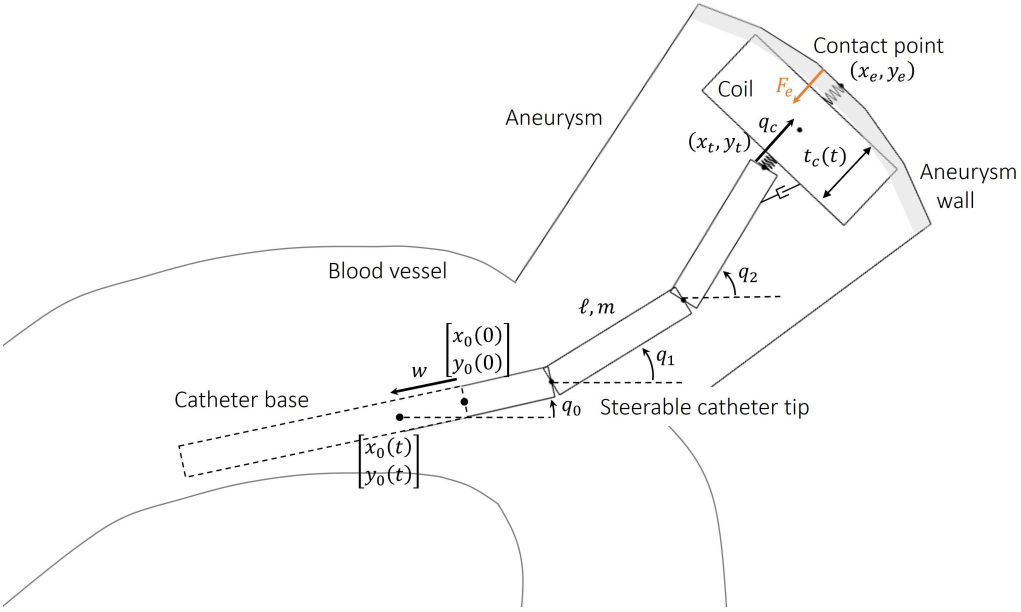

Figure 4-1: Extension of the catheter-coil-aneurysm system in Figure 3-1 with variable coil size $t_c(t)$ and the base displacement w defined with respect to $[x_0(0), y_0(0)]$.

where $\psi := (q_1, q_2, q_c)^T$ is the generalized coordinate vector and other parameters have been denoted in Table 3-1. Note that, unlike the joint angles (q_1, q_2) and the coil state (q_c), the base displacement (w) is not considered to be a generalized coordinate. It is assumed that its motion is slow and not greatly affected by the forces working on the tip of the microcatheter, i.e. its motion is considered static with respect to the fast motions of the catheter and coil. It is reasoned in Section 4-6 that slow catheter base velocities are actually desired. This modeling choice implies that system dynamics are equivalent to Chapter 3, that is

$$f(\psi, \dot{\psi}) = \frac{d}{dt}\begin{bmatrix} q \\ q_c \\ \dot{q} \\ \dot{q}_c \end{bmatrix} = \begin{bmatrix} \dot{q} \\ \dot{q}_c \\ M(\psi)^{-1}\left[\begin{bmatrix} Q \\ 0 \end{bmatrix} - C(\psi, \dot{\psi})\begin{bmatrix} \dot{q} \\ \dot{q}_c \end{bmatrix} - \begin{bmatrix} K_\Delta q + D_\Delta \dot{q} + g(q) \\ k_c(q_c - \frac{t_c}{2}) + d_c \dot{q}_c \end{bmatrix} - k_e \delta \begin{bmatrix} \partial\delta/\partial q \\ 1 \end{bmatrix}\right] \end{bmatrix}, \tag{4-2}$$

where the system matrices have been defined in Eqs. (3-4) and (3-5) but use the new system transform $T(\psi)$ in Eq. (4-1). The catheter's base displacement (w) is then introduced as a quasi-static variable which motion is considered to be solely affected by the pushing and pulling manoeuvre of the operator. This adds a new control input to the system, i.e. the force (τ_w) to push or pull the catheter. Note that the mapping from τ_w to some base velocity $\dot{w}$ is actuator specific. Therefore, this thesis assumes to have direct control over the catheter's base velocity $(\dot{w})$. By incorporating the quasi-static variable w in the coil growth model described in Eq. (2-34), the decoupled coil deployment dynamics follows as

$$\begin{aligned} \frac{d}{dt} y &= f(y, \bar{m}_c, \bar{t}_c, \bar{w}), \\ \epsilon \frac{d}{dv}\left(\begin{bmatrix} m_c \\ t_c \\ w \end{bmatrix}\right) &= \begin{bmatrix} r_m \\ r_t \\ \dot{w} \end{bmatrix}, \end{aligned} \tag{4-3}$$

where ϵ is small such that the coil-catheter-wall dynamics, i.e. $f(y)$ with $y := (\psi, \dot{\psi})$, develop on a faster time scale ($dt := \epsilon dv$) than the slow coil growth dynamics, and therefore can be decoupled. This implies that the coil's mass (m_c), the coil's size (t_c) and the catheter's base displacement (w) are considered to be quasi-static with respect to y. By brief inspection of Figure 4-1, it appears obvious that velocity ($\dot{w}$) should be appointed a negative value, when the coil's width grows with a positive rate (r_t), to sustain the contact force at its desired value ($F_e^\star$). However, it is non-trivial how $\dot{w}$ should be chosen to maintain the feasibility of desired tip position $(x_t^\star, y_t^\star)$ that corresponds to this value $F_e^\star$ and moves through space throughout the deployment procedure. To determine a control strategy for $\dot{w}$, it is firstly important to take a closer look at the constraints imposed by the aneurysm walls and the microcatheter's motion.

4-2 Constraint formulation

This section defines the constraints imposed by the aneurysm wall and the microcatheter. A method is proposed to efficiently compute the intersection of these polygons in task space, i.e. x and y coordinates. The resulting constraint polygon is used to assess the feasibility of the desired catheter tip position $(x_t^\star, y_t^\star)$, and thus the feasibility of desired contact force $(F_e^\star)$.

4-2-1 Catheter motion constraints

Every steerable catheter is constrained by a maximum bending angle (q_{max}) per steerable section. For the system in Figure 4-1, this implies $|q_{1,max}| := |q_{max} + q_0|$ and $|q_{2,max}| := |q_{max} + q_1|$. It has also been discussed in Chapter 3 that the catheter's configuration should maintain a single bend to assure uniqueness of the desired joint angles $(q_1^\star, q_2^\star)$ and independent control over the joint torques (τ_1, τ_2). This constrains $\Delta q_1 := q_1 - q_0$ and $\Delta q_2 := q_2 - q_1$ to have the same sign. These constraints are combined as

$$\begin{cases} 0 \leq \Delta q_i \leq q_{max} & d \leq 0 \\ -q_{max} \leq \Delta q_i \leq 0 & d > 0 \end{cases}, \quad \text{for} \quad i \in \{1, 2\}, \tag{4-4}$$

where d is an auxiliary variable that indicates whether the steerable microcatheter tip makes a clockwise ($d > 0$) or counterclockwise ($d \leq 0$) bend with respect to q_0 and is defined as,

$$d = x_t \sin q_0 - y_t \cos q_0, \tag{4-5}$$

where (x_t, y_t) is the catheter tip position as defined in Eq. (3-2). While the catheter constraints have been defined in joint space, the constraints imposed by the aneurysm wall are defined in task space. Therefore, the constraints in Eq. (4-4) are transformed into task space. For a counterclockwise bend, i.e. $d \leq 0$, this results in a non-convex constraint polygon C_{ccw} with a lower bound defined by $C_{ccw,min}$ and an upper bound defined by $C_{ccw,max}$, that is

$$\begin{aligned} C_{ccw,min} &:= \begin{cases} cs\left(\begin{bmatrix} 0 & q_1 & q_1 + q_{max} \end{bmatrix}\right)\gamma L & 0 \leq q_1 < q_{max}, \quad q_2 = q_{max} \\ cs\left(\begin{bmatrix} 0 & 0 & q_2 \end{bmatrix}\right)\gamma L & q_1 = q_{max}, \quad 0 \leq q_2 < q_{max} \end{cases}, \\ C_{ccw,max} &:= \begin{cases} cs\left(\begin{bmatrix} 0 & q_1 & q_1 \end{bmatrix}\right)\gamma L & 0 \leq q_1 < q_{max}, \quad q_2 = 0 \\ cs\left(\begin{bmatrix} 0 & q_{max} & q_2 + q_{max} \end{bmatrix}\right)\gamma L & q_1 = q_{max}, \quad 0 \leq q_2 < q_{max} \end{cases}, \end{aligned} \tag{4-6}$$

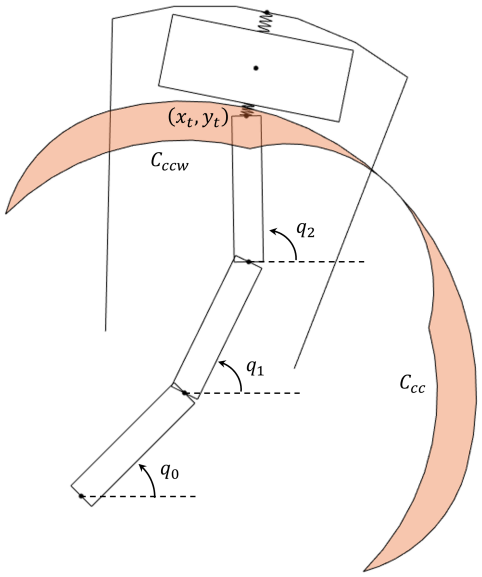

Figure 4-2: Constraints on the catheter's motion projected onto task space. The region C_{cc} indicates the constrained movement for a clockwise bend and C_{ccw} for a counterclockwise bend.

with function $cs(\alpha) \triangleq [\cos\alpha, \sin\alpha]^T$ and unitless lengths $\gamma := [\frac{1}{3}, \frac{1}{3}, \frac{1}{3}]^T$. This polygon is then rotated over the constant base direction (q_0) and translated with base displacement (w). The constraint space C_{cw} for a clockwise turn, i.e. $d > 0$, is defined by using $cs^{\perp}(\alpha) \triangleq [\cos\alpha, -\sin\alpha]^T$ instead of $cs(\alpha)$ in Eq. (4-6). The polygons C_{cw} and C_{ccw} are visualized in Figure 4-2 for a maximum bending angle of $q_{max} = \frac{\pi}{3}$ for both steerable sections. It can be observed from Figure 4-2 that, while some points are feasible from the catheter's motion perspective, not all points can be reached given the geometry of the aneurysm.

4-2-2 Aneurysm boundary constraints

The aneurysm walls impose tighter constraints on the feasible motion of the steerable catheter tip. A saccular aneurysm is considered to be convex and can be described with the polygon C_{wall}. This constraint space can be found by generating a 3D reconstruction angiogram prior to treatment (Appendix B-3). Note from Figure 4-2 that, given a constant base direction q_0, the catheter can only make a counterclockwise turn into the aneurysm. This thesis omits clockwise turns and restricts the catheter's constraint space to counterclockwise turns. This is a reasonable assumption given that the operator can manually control the roll, i.e. bending plane, of the catheter around the vector pointing in the direction of q_0. By turning the catheter's bending plane 180°, a clockwise turn becomes a counterclockwise turn. Therefore, the catheter's constraint space is redefined as $C_{cat} \triangleq C_{ccw}$. This thesis proposes to find the intersection between C_{cat} and C_{wall} by iteratively joining the vertices $C_{cat} := \{\boldsymbol{x_p}, \boldsymbol{y_p}\}$ with an edge $\mathcal{E} := \{(x_1, y_1), (x_2, y_2)\}$ of C_{wall}. The shortest, i.e. orthogonal, distance from any point in C_{cat} is computed with respect to wall edge $\mathcal{E}$, that is

$$\boldsymbol{d} = \frac{(x_2 - x_1)(y_1 - \boldsymbol{y_p}) - (x_1 - \boldsymbol{x_p})(y_2 - y_1)}{\sqrt{(x_2 - x_1)^2 + (y_2 - y_1)y}}. \tag{4-7}$$

The indices ($\boldsymbol{i}_d$) are selected for which the vector $\boldsymbol{d}$ changes sign. One can then compute the intersection points P_d with the aneurysm wall, i.e.

$$P_d = \boldsymbol{d}(\boldsymbol{i}_d) \odot \boldsymbol{n}_c + \begin{bmatrix} \boldsymbol{x_p}^T & \boldsymbol{y_p}^T \end{bmatrix}^T_{i_d}, \tag{4-8}$$

where $\boldsymbol{d}, \boldsymbol{n}_c, \boldsymbol{i}_d$ and $\odot$ are respectively the distance vector in Eq. (4-7), the orthogonal unit vector to edge $\mathcal{E}$, an index vector being either empty or containing two indices of intersection and the Hadamar product. The polygon $\{\boldsymbol{x_p}, \boldsymbol{y_p}\}$ can then be joined with edge $\{(x_1, y_1), (x_2, y_2)\}$ according to

$$C_{join} = \begin{cases} \begin{bmatrix} P_{d,1} & \begin{bmatrix} \boldsymbol{x_p}^T, \boldsymbol{y_p}^T \end{bmatrix}^T_{i_{d,1}:i_{d,2}} & P_{d,2} & P_{d,1} \end{bmatrix} & \text{sign}\left(\boldsymbol{d}(\boldsymbol{i}_{d,1}\right) < 0 \\ \begin{bmatrix} \begin{bmatrix} \boldsymbol{x_p}^T, \boldsymbol{y_p}^T \end{bmatrix}^T_{1:\boldsymbol{i}_{d,1}} & P_{d,1} & \begin{bmatrix} \boldsymbol{x_p}^T, \boldsymbol{y_p}^T \end{bmatrix}^T_{i_{d,2}:end} \end{bmatrix} & \text{sign}\left(\boldsymbol{d}(\boldsymbol{i}_{d,1}\right) \geq 0 \end{cases}, \tag{4-9}$$

where C_{join} is the intersected constraint polygon and $\text{sign}\left(\boldsymbol{d}(\boldsymbol{i}_{d,1}\right))$ indicates whether the first point of $\{\boldsymbol{x_p}, \boldsymbol{y_p}\}$ is located outside or within the aneurysm wall. This proposed strategy can be followed to iteratively update C_{join} for all wall edges defined by C_{wall}. The full routine has been described in Appendix A-2. For simplicity, this thesis assumes that C_{wall} can be fully described by a left side edge, defined by the vertices $\{(x_1^l, y_1^l), (x_2^l, y_2^l)\}$, and a right side edge, defined by the vertices $\{(x_1^r, y_1^r), (x_2^r, y_2^r)\}$, as has been illustrated in Figure 4-3. Note however, that the presented method is valid for any convex, i.e. saccular, aneurysm geometry.

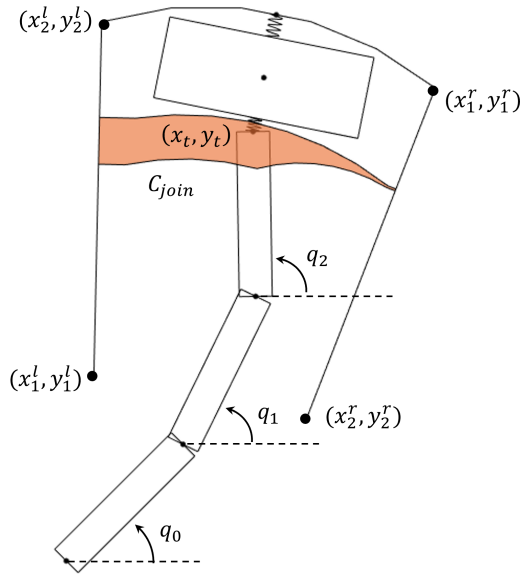

Figure 4-3: Joined catheter and aneurysm constraints.

Based on this section, several observations can be made. Firstly, note that a reference tip position $(x_t^\star, y_t^\star)$ outside of C_{join} implies that the contact force (F_e) between the coil and the aneurysm wall cannot be controlled to the corresponding reference force $(F_e^\star)$. Secondly, note that $(x_t^\star, y_t^\star)$ cannot be controlled by the operator. Then, note that the constraint space (C_{join}) moves with a base displacement (w) along the catheter base direction (q_0). Lastly, note that $\dot{w}$ is a control parameter. To conclude, C_{join} should be controlled with velocity $(\dot{w})$ to preserve the feasibility of $F_e^\star$.

4-3 Control objective

To sensibly shape the catheter base velocity ($\dot{w}$) for the first order system in Eq. (4-3), a clear control objective needs to be defined. This objective is derived based on the illustration in Figure 4-4. It can be argued that the chance of feasibility for the reference position $(x_t^\star, y_t^\star)$ is maximized when the distance from the $(x_t^\star, y_t^\star)$ to the boundaries of the constraint polygon (C_{join}) is maximal. This leads to the proposal that the centre line, i.e. $\bar{C}_{join}(x, w)$, of C_{join} should contain $(x_t^\star, y_t^\star)$ to maximize the target's distance from the boundaries of C_{join}. The centre line $\bar{C}_{join}(x, w)$ has been approximated with a 4^{th}-order polynomial by employing Matlab's `fit(x,y,'poly4')` function on a set of points in the middle of the polygon C_{join}. This line can be computed before the procedure, i.e. for $w(0) = 0$, and updated every time step based on w which moves along the constant direction q_0. The polynomial centre line is then defined as

$$\bar{C}_{join}(x, w) = a_0(x - w_x)^4 + a_1(x - w_x)^3 + a_2(x - w_x)^2 + a_3(x - w_x) + a_4 + w_y, \tag{4-10}$$

with $w_x := w\cos(q_0)$ and $w_y := w\sin(q_0)$. Correspondingly, the optimal centre line is defined as $\bar{C}^\star_{join}(x, w - \Delta w)$ where the error (Δw) is defined as the distance along q_0 between the centre line $\bar{C}_{join}(x, w)$ and the point $(x_t^\star, y_t^\star)$ lying on optimal centre line $\bar{C}^\star_{join}(x, w - \Delta w)$. Accordingly, a control objective can be defined, i.e.

$$\lim_{t\to\infty} \Delta w = 0, \quad \text{with} \quad \Delta w = w - w^\star, \tag{4-11}$$

where $w^\star$ is the desired global catheter displacement. Note that, due to coil growth, the tip reference position $(x_t^\star, y_t^\star)$ is not a constant point in space but moves with velocity $(x_t^\star, y_t^\star)'$ defined as,

$$(x_t^\star, y_t^\star)' = r_t \boldsymbol{n}_\perp, \tag{4-12}$$

where r_t is the coil's helix growth rate and $\boldsymbol{n}_\perp$ is the unit vector orthogonal to the contact plane. The coil's growth rate r_t can be derived from the coil injection rate (τ_{in}) and the aneurysm geometry (Appendix A-1), and is considered to be constant in this chapter. The vector $\boldsymbol{n}_\perp$ can be determined prior to treatment using 3D reconstruction angiography as

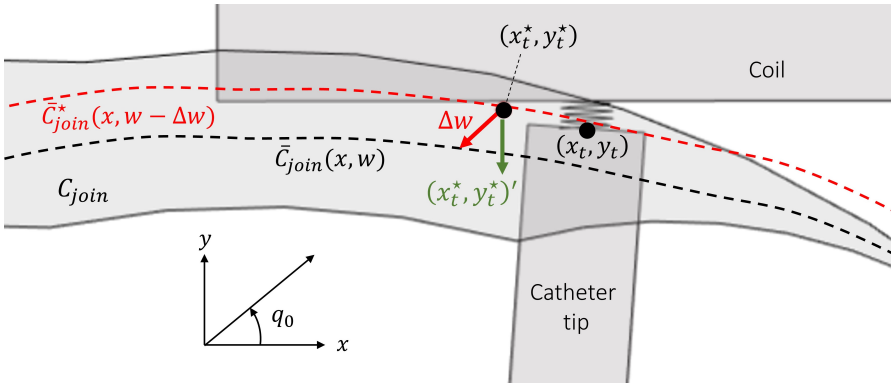

Figure 4-4: Augmented view of the constraint polygon C_{join} in Figure 4-3 and its 4^{th}-order polynomial centre line $\bar{C}_{join}(x, w)$. The optimal centre line $\bar{C}^\star_{join}(x, w - \Delta w)$ contains the position $(x_t^\star, y_t^\star)$ which moves through space with its velocity $(x_t^\star, y_t^\star)'$ defined in Eq. (4-12).

presented in Appendix B-3. It should be noted that it is a non-trivial task to directly relate the velocity vector $(x_t^\star, y_t^\star)'$ to the desired reference velocity $\dot{w}^\star$. As depicted in Figure 4-5, the nonlinear form of $\bar{C}^\star_{join}(x, w)$ yields a recursive problem to find Δw such that an exact solution is hard to find. It is thus proposed to place an upper bound on $\dot{w}^\star$ according to

$$|\dot{w}^\star| < \frac{1}{\cos(q_0)} \max_t \left[(x_t^\star(t), y_t^\star(t))'_y \right], \tag{4-13}$$

where $(x_t^\star(t), y_t^\star(t))'_y$ is the maximum y-component of $(x_t^\star, y_t^\star)$ over time. This component is then projected on the sliding direction of w, i.e. q_0. Due to the estimation of $\dot{w}^\star$, exact target tracking is not possible. However, due to low values of $\dot{w}$, one can state an alternative regulation control objective, that is

$$\lim_{t\to\infty} \Delta w \in [-\epsilon, \epsilon], \quad \text{with} \quad \Delta w = w - w^\star, \tag{4-14}$$

where ϵ denotes a small margin around $\bar{C}_{join}(x, w)$. Approximate tracking of $\bar{C}^\star_{join}(x, w^\star)$ is not necessarily a problem as closeness to $\Delta w = 0$ also implies membership of the polygon C_{join}. Just as velocity $\dot{w}^\star$, the error signal Δw cannot simply be derived. However, this signal is essential for control. Therefore, a method is proposed in the following section to efficiently approximate its value.

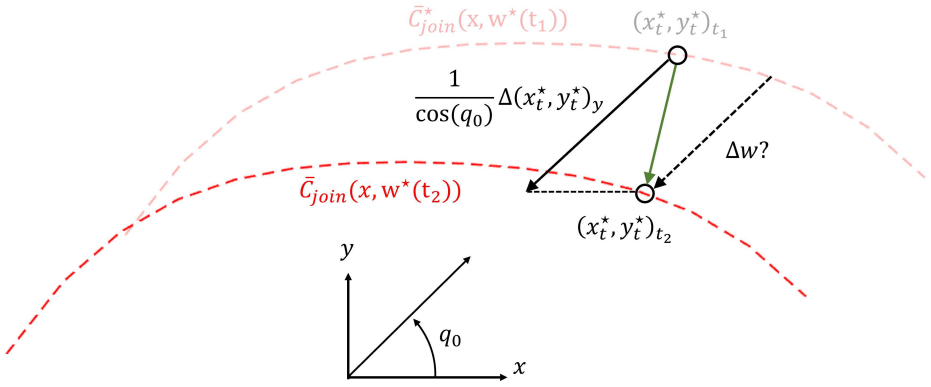

Figure 4-5: Trajectory $(x_t^\star, y_t^\star)$ with respect to the optimal curve $\bar{C}^\star_{join}(x, w^\star)$ at the time points t_1 and t_2. Due to the nonlinear nature of $\bar{C}^\star_{join}(x, w)$, vertical adjustment with $\Delta(x_t^\star, y_t^\star)$ is not sufficient. This yields a recursive problem that can hardly be solved exactly.

4-3-1 Optimization of Δw

As has been discussed in the previous section, the error signal Δw in Figure 4-4 is zero when centre line $\bar{C}_{join}(x, w)$ contains the tip reference position $(x_t^\star, y_t^\star)$. It has also been discussed that the error signal Δw cannot simple be derived, and thus should be approximated throughout the deployment procedure. The proposed optimization strategy for Δw has been illustrated in Figure 4-6. The optimization objective is to find a point (x_w, y_w) that is the intersection point of the current centreline $\bar{C}_{join}(x, w)$ with a vector pointing in the direction q_0 and intersecting $(x_t^\star, y_t^\star)$. This objective function is then stated as

$$e_y := |y_w - C_{join}(x_w, w)|, \tag{4-15}$$

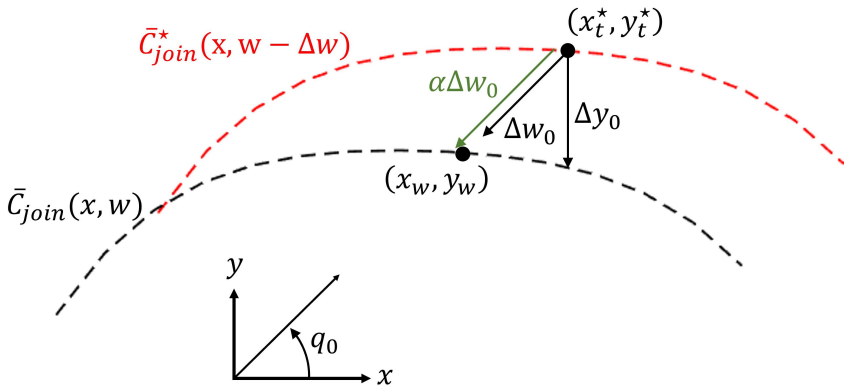

Figure 4-6: Illustration of the optimization strategy to find the error signal Δw in Figure 4-4. The objective is to find a gain α such that the vector $\alpha\Delta w_0$ spans from $(x_t^{\star}, y_t^{\star})$ to its end point (x_w, y_w) such that (x_w, y_w) lies on the polynomial centreline $\bar{C}_{join}(x, w)$.

where e_y is the vertical distance from (x_w, y_w) to the current constraint centre line $\bar{C}_{join}(x, w)$. A first guess on (x_w, y_w) can be made by computation of the following vector,

$$\Delta w_0 = R(q_0)\Delta y_0 = \begin{bmatrix} \cos q_0 & -\sin q_0 \\ \sin q_0 & \cos q_0 \end{bmatrix} \begin{bmatrix} 0 \\ \bar{C}_{join}(x_t^{\star}, w) - y_t{}^{\star} \end{bmatrix} \tag{4-16}$$

where $R(q_0)$, Δy_0 and Δw_0 are respectively a rotation matrix, the known vertical distance vector from $(x_t^{\star}, y_t^{\star})$ to polynomial centre line $C_{join}(x, w)$ and a vector pointing from $(x_t^{\star}, y_t^{\star})$ in the direction of (x_w, y_w). The first guess of (x_w, y_w) is then defined as

$$(x_w, y_w) = (x_t^{\star}, y_t^{\star}) - \Delta w_0. \tag{4-17}$$

It is then proposed to minimize the error e_y in Eq. (4-15) by multiplying Δw_0 with a gain α that is updated according to a learning rule, i.e.

$$\alpha = 1 + \sum_{n=1}^{n_{max}} \left(\frac{1}{2}\right)^n \text{sign}(\Delta w_0 e_y), \tag{4-18}$$

where n_{max} and sign(.) are the maximum number of iterations and the vector `sign` function defined as

$$\text{sign}\,(v) = \begin{cases} 1 & \begin{bmatrix} \cos q_0 & \sin q_0 \end{bmatrix} v > 0 \\ 0 & \begin{bmatrix} \cos q_0 & \sin q_0 \end{bmatrix} v = 0 \\ -1 & \begin{bmatrix} \cos q_0 & \sin q_0 \end{bmatrix} v < 0 \end{cases}, \tag{4-19}$$

where vector v is positive when it points in the positive direction over q_0 and negative otherwise. The optimization routine is repeated until $e_y < \epsilon$ with ϵ sufficiently small. The error signal Δw can then be determined according to

$$\Delta w = \text{sign}\,(\Delta w_0) \left|\left| \begin{bmatrix} x_t^{\star} \\ y_t^{\star} \end{bmatrix} - \begin{bmatrix} x_w \\ y_w \end{bmatrix} \right|\right| \triangleq \alpha\ \text{sign}\,(\Delta w_0)\, ||\Delta w_0||\,, \tag{4-20}$$

where α and Δw_0 are the optimized gain and the initial distance vector defined in Eq. (4-16). The full optimization routine to find Δw at each integration step has been described in Appendix A-3.

4-4 Control architecture

This section presents a control architecture (Figure 4-7) that drives the contact force (F_e) between the coil and the aneurysm wall to the desired reference state ($F_e^\star$) throughout a coil deployment procedure. This entails the design of a constraint preservation controller that maintains the desired catheter tip position ($x_t^\star, y_t^\star$) on a derived constraint surface, and thus preserves the feasibility of the contact force regulation objective.

The right top of the control architecture shows computations that are executed prior to treatment and stored in a local data store. This entails the measurement of q_0 and the reconstruction of a polynomial centre line $\bar{C}_{join}(x, w)$ from the constraint polygon C_{join} as described in Section 4-2. The coil's injection velocity (τ_{in}) and the force reference ($F_e^\star$) are defined by the operator. The system output of interest is the contact force (F_e). The measured feedback signals are the catheter's joint angles (q_1, q_2) and its base displacement (w). The tendon torques (τ_1, τ_2) are the inputs generated by the joint controller described in Chapter 3 to guide (q_1, q_2) to ($q_1^\star, q_2^\star$), implying convergence of F_e to $F_e^\star$. The base velocity ($\dot{w}$) is computed such that the constraint space $C_{join}(x, w)$ moves to $\bar{C}_{join}^\star(x, w^\star)$, and thus feasibility for the $F_e^\star$ is preserved. A step-by-step system routine has been described in Appendix A that corresponds to the architecture in Figure 4-7.

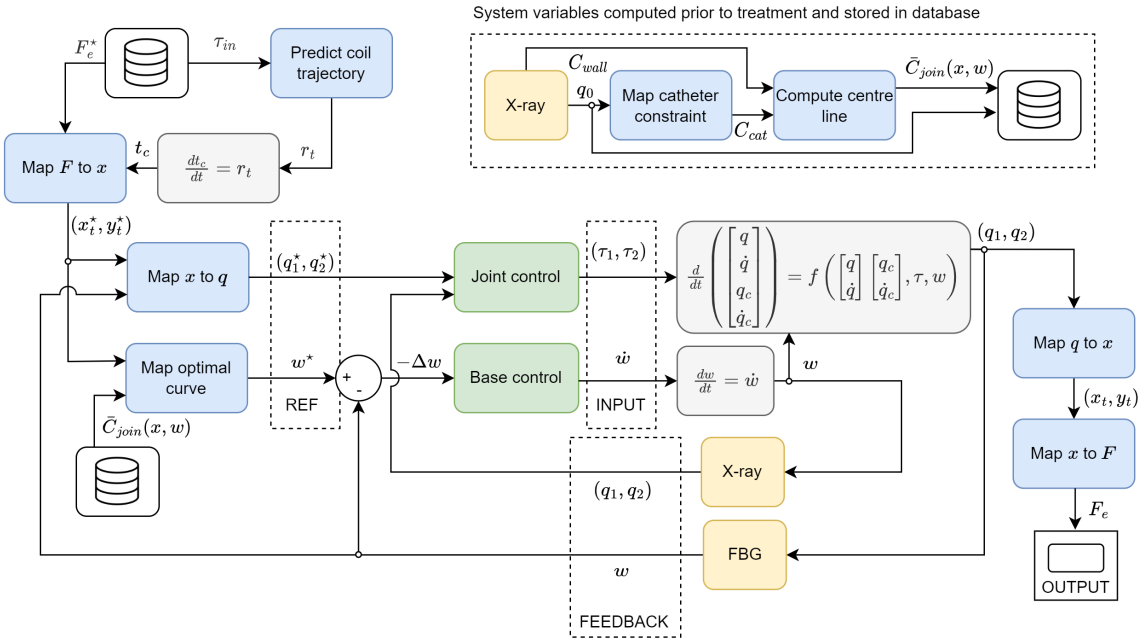

Figure 4-7: Control architecture for tension control during coil deployment in a constrained environment.

4-4-1 Controller design

Based on the objective and the error signal (Δw) defined in Section 4-3, a controller can be designed. First, the simplified case is considered where no coil deployment takes place, i.e.

$r_t = 0$, implying that the tip reference position $(x_t^\star, y_t^\star)$ is static. For this static case, it is sufficient to use the following control law,

$$\dot{w} = -\beta \, \text{sign}\left(\Delta w\right), \tag{4-21}$$

where β is a non-negative constant. Given instant control over $\dot{w}$, it is shown in Section 4-4-2 that this control law achieves the objective in Eq. (4-11), i.e. $\Delta w \to 0$. The physical interpretation of this controller is that target $(x_t^\star, y_t^\star)$ attracts curve $\bar{C}_{join}(x, w)$. A higher value of β indicates a more aggressive control action. This case can now be extended to the case where coil deployment takes place, i.e. $r_t > 0$ and tip reference position $(x_t^\star, y_t^\star)$ is moving through space according to Eq. (4-12). Since $\dot{w}^\star$ is not exactly known, chattering behaviour around $\Delta w = 0$ should be prevented. Therefore a smooth control action around $\Delta w = 0$ is considered [50], that is

$$\dot{w} = -\beta \tanh\left(\frac{4}{\epsilon}\Delta w\right), \tag{4-22}$$

where ϵ is the small margin defined in Eq. (4-14) and the factor 4 has been chosen to shape the hyperbolic tangent such that $|\dot{w}| \approx \beta$ at $|\Delta w| = \epsilon$. The resulting closed-loop system, i.e.

$$\frac{d}{dt}\left(w\right) = -\beta \tanh\left(\frac{4}{\epsilon}\Delta w\right), \tag{4-23}$$

has been illustrated as a block diagram in Figure 4-8. It is shown through stability analysis in Section 4-4-2 that this controller achieves the regulation objective in Eq. (4-11) given a lower bound on control gain β. Moreover, it should be noted that w is considered a quasi-static variable, i.e. its velocity $\dot{w}$ should remain small.

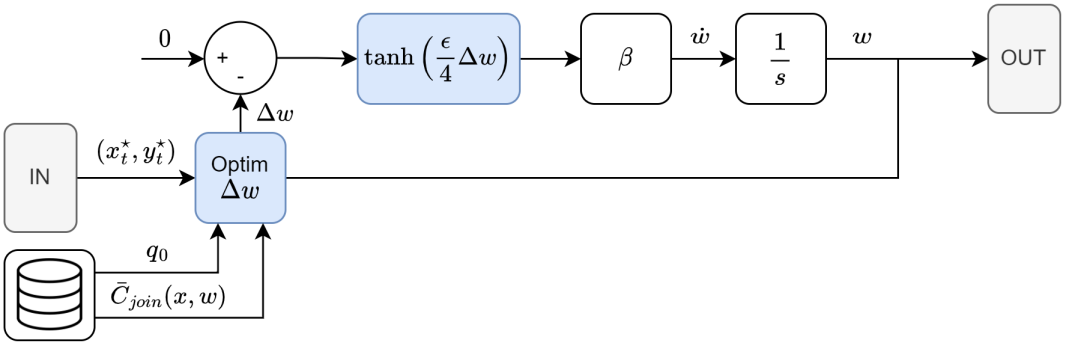

Figure 4-8: Block diagram of the first order closed-loop dynamics for the base displacement (w) as denoted in Eq. (4-23).

When β is chosen inadequately or when position $(x_t^\star, y_t^\star)$ collides with the aneurysm wall, the controller should be augmented with safety measures. For this, one can evaluate Matlab's function `inpolygon`$(x_t^\star, y_t^\star, C_{join})$ to check whether $(x_t^\star, y_t^\star)$ is a feasible target and interrupt the treatment when this property is no longer satisfied, i.e.

$$\begin{cases} \dot{w} = -\beta \tanh\left(\frac{4}{\epsilon}\Delta w\right) & (x_t^\star, y_t^\star) \in C_{join} \\ \textbf{break} & (x_t^\star, y_t^\star) \notin C_{join} \end{cases}. \tag{4-24}$$

4-4-2 Stability analysis

This section shows through stability analysis that the proposed controller in Eq. (4-24) moves the polynomial centre line $\bar{C}_{join}(x, w)$ such that it approximately contains $(x_t^\star, y_t^\star)$. This implies that the contact force (F_e) between the coil and the aneurysm wall can be asymptotically driven to its desired value $(F_e^\star)$. The following theorem states that given Δw converges to within the set $[-\epsilon, \epsilon]$, asymptotic stabilization of the contact force (F_e) between the coil and the aneurysm wall at desired force $(F_e^\star)$ follows. This section uses notions of Lyapunov stability and LaSalle's invariance principle as defined in Appendix B-1.

Theorem 4.1 Consider the systems in Eq. (4-3) with the controllers in Eq. (3-18) and in Eq. (4-22). The error of $(x_t^\star, y_t^\star)$ to the centre line of the constraint space (Δw) defined in Eq. (4-15) and the force error $(\tilde{F}_e)$ define in Eq. (3-7) are globally asymptotically stable, that is

$$|\Delta w| \to [-\epsilon, \epsilon] \implies |\tilde{F}_e| \to 0 \quad as \quad t \to \infty, \tag{4-25}$$

provided that

$$\begin{aligned}
(x_t^\star(0), y_t^\star(0)) &\in C_{join}, && (4\text{-}26)\\
(x_t^\star(t), y_t^\star(t)) &\in C_{wall} \quad \forall t \in [0, t_f], && (4\text{-}27)\\
\beta &\geq \max_t \left[r_t(t)\right] \boldsymbol{n}_y^\perp \frac{1}{\cos q_0}, && (4\text{-}28)\\
\lambda_m\{K_\Delta\} &\geq k_g \text{ and} && (4\text{-}29)\\
d, d_c &> 0, && (4\text{-}30)
\end{aligned}$$

hold, where $[-\epsilon, \epsilon]$ is a small desired set, C_{join} is the constraint polygon for tip reference position $(x_t^\star, y_t^\star)$, C_{wall} denotes the constraints imposed by the aneurysm wall, t_f is the time required to deploy a single helical coil, β is a control parameter, q_0 is the catheter's constant base direction, $\boldsymbol{n}_y^\perp$ is the y-component of the vector orthogonal to the aneurysm wall in contact, r_t is the coil's helix growth rate, $\lambda_m\{K_\Delta\}$ denotes the eigenvalues of catheter stiffness matrix K_Δ, k_g is defined in Property 4.4 and d and d_c are the damping coefficients for respectively the catheter and the coil.

Proof 4.1 Take the following Lyapunov candidate, i.e.

$$V(\Delta w) = \frac{1}{2}\Delta w^2 \tag{4-31}$$

with $\Delta w = w - w^\star$, which is a valid candidate as this function is clearly continuously differentiable, radially unbounded, positive definite for all nonzero Δw and equal to zero for $\Delta w = 0$. The time derivative of $V(\Delta w)$ takes the following form, i.e.

$$\dot{V}(\Delta w) = \frac{\partial V(\Delta w)}{\partial \Delta w}(\dot{w} - \dot{w}^\star) = \Delta w \left[-\beta \tanh\left(\frac{4}{\epsilon}\Delta w\right) - \dot{w}^\star\right], \tag{4-32}$$

using the expression for $\dot{w}$ in Eq. (4-22). When the coil does not grow, i.e. reference velocity $\dot{w}^\star$ is zero, it can be shown that $\dot{V}(\Delta w)$ is seminegative definite for any $\beta > 0$ by noting that the function $x \tanh(x)$ always has a positive sign. By invoking Lyapunov's direct method, it

is concluded that the origin is a globally asymptotically stable equilibrium of the closed-loop system in Eq. (4-23).

On the other hand, when $(x_t^\star, y_t^\star)$ is moving through space, i.e. $(\dot{w}^\star \neq 0)$, it can be verified that negative definiteness for $\dot{V}(\Delta w)$ does not hold for all values of Δw. This yields a lower bound on the control action $\dot{w}$, that is

$$\left|\tanh\left(\frac{4}{\epsilon}\Delta w\right)\right| \beta \geq |\dot{w}^\star|\,, \tag{4-33}$$

where the absolute upper bound of $\dot{w}^\star$ has been defined in Eq. (4-13), that is

$$\beta^\star := |\dot{w}^\star| = \max_t \left[r_t(t)\right] \boldsymbol{n}_y^\perp \frac{1}{\cos q_0}, \tag{4-34}$$

where $\boldsymbol{n}_y^\perp r_t$ and q_0 are respectively the vertical velocity of $(x_t^\star, y_t^\star)'$ and the direction along which $\dot{w}$ is controlled. Note that $\tanh(x)$ converges to zero for small values of x. Therefore, no choice of β exists to satisfy the expression in Eq. (4-33) for an arbitrary small value of Δw. However, note that the constraint in Eq. (4-33) reduces to

$$\beta \geq \beta^\star \tag{4-35}$$

for any $|\Delta w|$ greater than ϵ. By choosing $\beta = \beta^\star$, it can be verified that $\dot{V}(\Delta w)$ is negative definite for all values $\Delta w \notin [-\epsilon, \epsilon]$, and thus Δw at least converges to within the desired set $[-\epsilon, \epsilon]$. Given that $\beta^\star$ is an overestimation of the upper bound of $|\dot{w}^\star|$, LaSalle's invariance principle can be invoked to show that the set,

$$\Omega = \{\Delta w \in \mathbb{R}^{2n} \cap \Delta w \notin [0, \alpha] : \dot{V}(\Delta w) = 0\}, \tag{4-36}$$

consists of the points $\{0, \alpha\}$ where α is positive unknown value within the desired set $[-\epsilon, \epsilon]$. Hence, all trajectories starting outside of the level set $[0, \alpha]$ will converge to its boundary and any trajectory for Δw starting within $[0, \alpha]$ will remain within $[0, \alpha]$. Note that $\Delta w = 0$ is an unstable equilibrium, hence the trajectories converging to $\Delta w = 0$ will move within the set $[0, \alpha]$. Given that the level set $[0, \alpha]$ lies within the desired set $[-\epsilon, \epsilon]$, the trajectories of Δw converge to within the desired set $[-\epsilon, \epsilon]$, hence the reference position $(x_t^\star, y_t^\star)$ is a feasible target for the joint controller defined in Eq. (3-18). Given that the point $(x_t^\star, y_t^\star)$ is a feasible target, **Theorem 4.1** can be evoked to show that F_e is asymptotically stabilized at the desired reference $F_e^\star$. It should be noted that, at $t = 0$, $(x_t^\star, y_t^\star)$ should be a member of C_{join}, i.e.

$$(x_t^\star(0), y_t^\star(0)) \in C_{join}, \tag{4-37}$$

and the coil is of an appropriate size such that $(x_t^\star, y_t^\star)$ does not collide with the aneurysm walls C_{wall} during deployment time t_f, i.e.

$$(x_t^\star(t), y_t^\star(t)) \in C_{wall} \quad \forall t \in [0, t_f]. \tag{4-38}$$

4-5 Simulations

To validate the theoretic proof in Section 4-4-2, this section shows through numeric simulation that the control objectives in respectively Eqs. (3-13) and (4-14) are achieved. This implies that the imposed constraints are obeyed and that the contact force (F_e) between an endovascular coil and the aneurysm wall is regulated at the desired value ($F_e^\star$) during the deployment of an endovascular coil in the aneurysm dome.

This environment has been simulated according to Figure 4-1 and control has been implemented according to the architecture depicted in Figure 4-7. The parameter settings are equivalent to Table 3-1 and new parameter settings are stated in Table 4-1. Note that the desired coil-wall tension has again been chosen as $F_e^\star := 0.5F_{e,max} = -0.1$N. For clarity, the coil growth rate (r_t) is chosen to be constant and grows at 17% with respect to the coil's initial size $t_c(0)$. The control parameter β has been chosen equal to the lower bound defined in *Eq.* (4-34), that is $\beta^\star = 0.116$.

The simulation activates the force-regulating joint controller at $t = 0$ seconds. Subsequently, the deployment of new coil material starts at $t = 5$ seconds. Given the growth rate (r_t), the coil is assumed to be fully deployed at $t = 20$. According to Eq. (4-24), the procedure is interrupted when $(x_t^\star, y_t^\star)$ leaves the derived constraint polygon C_{join}. Four simulation images of a successful coil deployment procedure have been visualized in Figure 4-15. The algorithm in Appendix A-2, i.e. to create C_{join} from C_{cat} and C_{wall}, has been applied to map the coil structure within the aneurysm walls.

The system outputs, relevant to evaluate the force control objective in Eq. (3-13), are presented in Figures 4-9 to 4-11. It can be observed from Figure 4-9 that the proposed joint controller has succeeded to stabilize contact force F_e at its $F_e^\star$ throughout the coil deployment procedure. Figure 4-10 shows that $(x_t^\star, y_t^\star)$ moves with a constant rate (r_t) through space as described in Eq. (4-12). Moreover, Figure 4-11 shows that reference joint angles $(q_1^\star, q_2^\star)$ are adjusted accordingly and tracked appropriately by the joint controller.

The system outputs, relevant to evaluate the constraint space tracking objective in Eq. (4-11), are depicted in Figures 4-12 and 4-13. It can be observed from Figure 4-13 that the control action ($\dot{w}$) is smooth over the coil deployment interval $t \in [5, 20]$. Subsequently, it can be noted from Figure 4-12 that error signal Δw converges to some small value $\alpha < \epsilon$. This implies that the distance from $(x_t^\star, y_t^\star)$ to the constraint boundaries has been approximately maximized. The simulation captures in Figure 4-15 show that the procedure has been completed, i.e. C_{join} has been translated with displacement (w) such that $(x_t^\star, y_t^\star)$ remained a feasible target. To verify that the value of β has been chosen appropriately, simulations have been conducted for varying values of β, i.e. $\boldsymbol{\beta} := \{\frac{1}{2}\beta^\star, \beta^\star, 2\beta^\star\}$. The resulting errors ($\Delta w$) have been aggregated in Figure 4-14. It can be observed that an inadequate choice of β, i.e. $\beta = \frac{1}{2}\beta^\star$, results in $(x_t^\star, y_t^\star)$ moving out of the constraint polygon C_{join}, and thus requiring interruption of the procedure at $t = 9$ seconds. A more aggressive choice of β, i.e. $\beta = 2\beta^\star$ shows a slightly faster stabilization of Δw around zero. It is discussed in Section 4-6 that it is desired to choose β as small as possible.

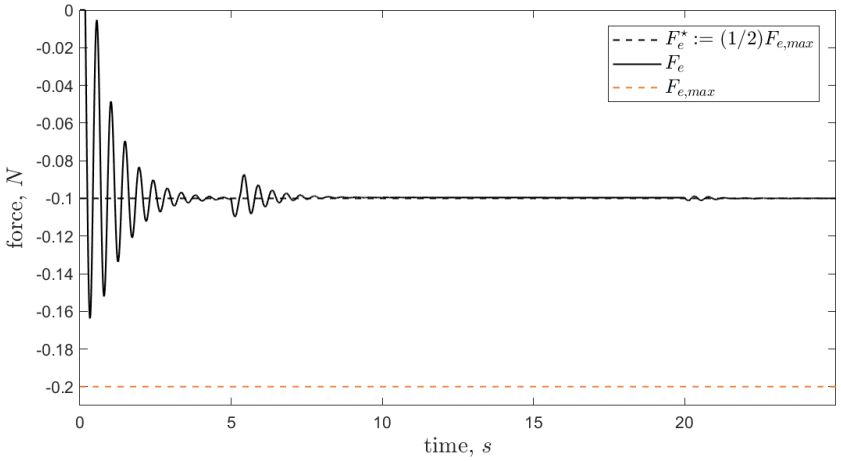

Figure 4-9: Contact force regulation between a coil and the aneurysm wall in the coil deployment case.

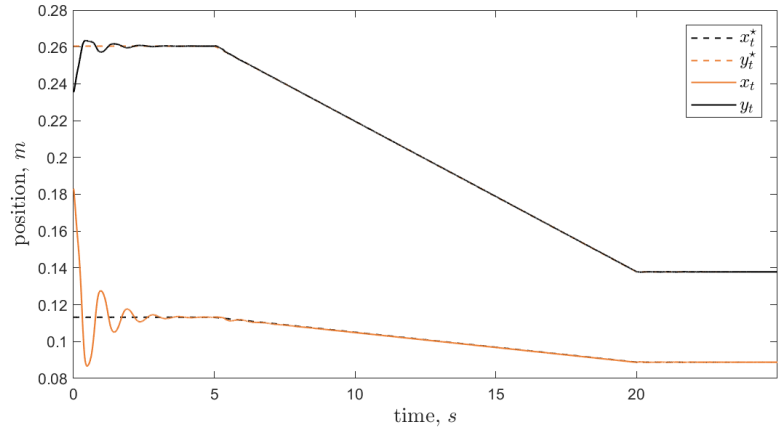

Figure 4-10: Catheter tip position regulation in the coil deployment case.

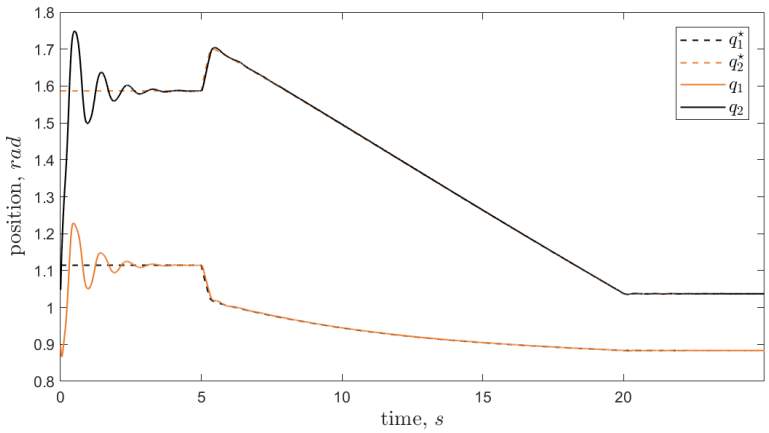

Figure 4-11: Catheter joint angle regulation in the coil deployment case.

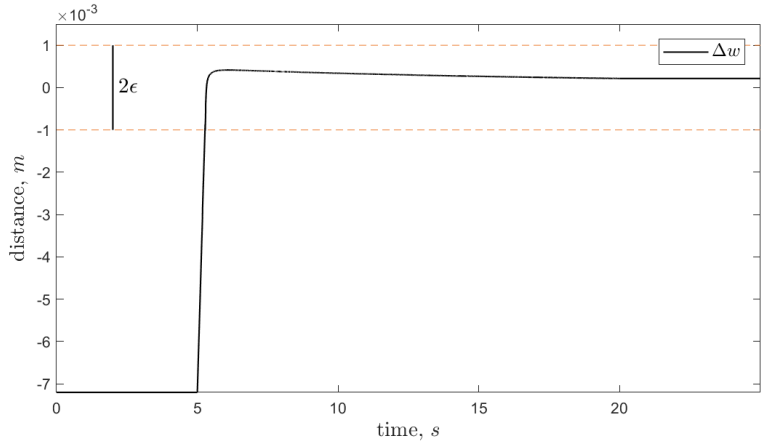

Figure 4-12: Regulation of the catheter's base displacement (w) with the error (Δw) such that the polynomially fitted centre line, i.e. $\bar{C}_{join}(x, w)$, moves to $(x_t^\star, y_t^\star)$. Control starts at $t = 5$ seconds.

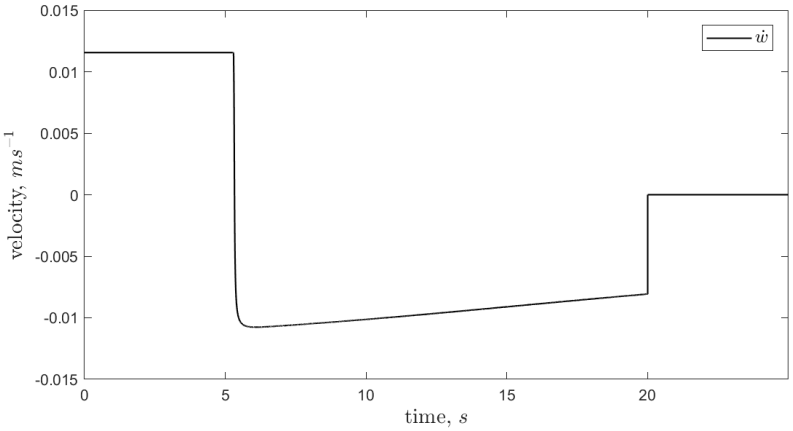

Figure 4-13: The controlled catheter's base velocity $(\dot{w})$ for the regulation of displacement (w) with error (Δw) in Figure 4-12. Control starts at $t = 5$.

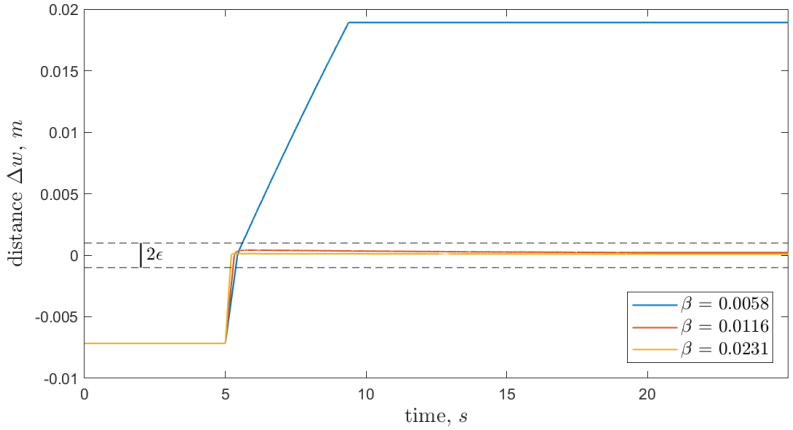

Figure 4-14: Regulation of the catheter's base displacement (w) for different choices of the control gain β, i.e. $\boldsymbol{\beta} := \{\frac{1}{2}\beta^\star, \beta^\star, 2\beta^\star\}$.

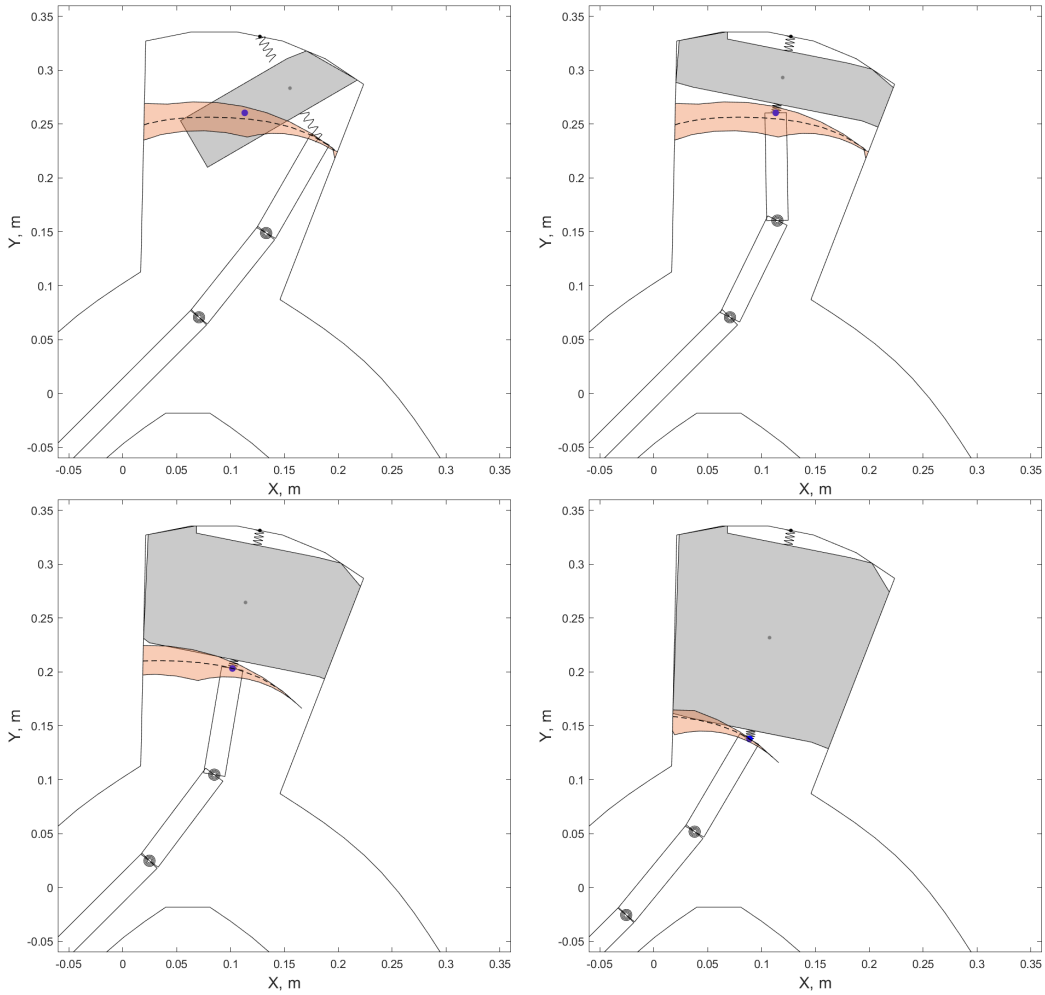

Figure 4-15: Stages of coil deployment at $t = 0$ (left top, start force control), $t = 5$ (right top, start deployment), $t = 12$ (left bottom, mid-deployment), $t = 20$ (right bottom, end of deployment).

4-6 Discussion

In conclusion, this chapter has presented a control architecture that enables regulation of the contact force (F_e) between the coil and the aneurysm wall while obeying the constraints imposed by the equipment and the environment. The presented architecture comprises an auxiliary velocity controller for the catheter's base that maximizes the feasibility of the augmented energy-shaping joint controller presented in Chapter 3. It has been shown through stability analysis and numeric simulations that the presented architecture asymptotically guides the contact force (F_e) towards its desired equilibrium $F_e^\star$ throughout the deployment procedure.

In detail, this chapter has proposed to decouple the fast joint control motions from the slow base velocities of the catheter's base, allowing for a separate controller design. The auxiliary velocity controller moves a polynomial fitted centre line, i.e. $\bar{C}_{join}(x, w)$, of the constraint

space (C_{join}) such that it approximately contains the reference tip position $(x_t^\star, y_t^\star)$. This method maximizes the distance of $(x_t^\star, y_t^\star)$ with respect to constraint boundaries, and thus preserves the feasibility of the force control objective in Eq. (3-13). Throughout this chapter, various assumptions have been made. In the following paragraphs, these modelling choices and simulation results are discussed in more detail.

To start with, it should be underlined that the control action ($\dot{w}$) serves as an auxiliary control input to the tendon torques (τ_1, τ_2) provided by the joint controller. Alternatively said, the system cannot fully rely on the base velocity ($\dot{w}$) for precise control. Ideally, the catheter would move according to one-to-one movement, i.e. the catheter's steerable tip moves forward 1 mm when the proximal base is pushed forward 1 mm. This is often not the case, as the catheter's body shifts from the lesser curves to the greater curves in the blood vessel, i.e. resulting in a slack catheter. A slack catheter stores more elastic energy. The excessive load in the system leads to the loss of fine microcatheter control. Moreover, the system can experience a sudden release of elastic energy. This causes a forward-jumping motion of the microcatheter which can induce aneurysm rupture (Section 1-1-3). The excessive load can be relieved by slowly retracting the catheter, resulting in shifts from the greater to the lesser vessel curves until one-to-one movement is restored [18]. This mechanism is the reason why $\dot{w}$ is not used in conjunction with a single degree of freedom catheter, i.e. $q := q_1$, to facilitate force control. It is argued that a slow enough retraction rate of $\dot{w}$ is the only safe way to control the catheter's base movement. This enables the use of decoupled system dynamics but also restricts the magnitude of control parameter β in Eq. (4-24). It should be noted that small deviations from $(\Delta w = 0)$ do not necessarily pose a problem as closeness to $(\Delta w = 0)$ also implies membership of the polygon C_{join}, and thus enables stabilization of the contact force (F_e) at $F_e^\star$. Therefore, it is advised to place β at its lower bound $\beta^\star$ as defined in Eq. (4-34).

It should also be mentioned that it has been assumed, in this thesis, that the procedure can be interrupted at any time. In this case, the control action in *Eq.* (4-24) guarantees the procedure's safety. However, when the microcatheter's lumen still contains part of the coil, the coil cannot be simply cut in half, and thus some action has to be taken. The most obvious action is to stop the controlled deployment procedure and let the operator take back command over the procedure. The operator can then choose to withdraw the coil, manually deploy the coil or change the catheter's bending plane.

Another assumption throughout this chapter is that catheter base movement is constrained to move along q_0. It has been discussed in Section 2-4 that the direction (q_0) is mostly determined by the shape of the vessel adjacent to the aneurysm. However, this chapter has described the retraction of the microcatheter along the vessel wall. It can be argued that the catheter's retraction would not change the base direction q_0 until the base position (x_0, y_0) has reached the closest vessel bend. It is assumed that the distance to the closest bend is sufficiently large such that the catheter can be pulled out of the aneurysm along a constant direction (q_0).

Lastly, it is important to discuss the real-time feasibility of the presented control architecture, i.e. computation of the control actions should be implemented fast enough for them to be useful. The presented control architecture has a run time of 15 seconds for a simulation time of 25 seconds. This is an indication that the presented architecture is real-time feasible. To improve the architecture's run time, one could inspect the efficiency of the separate system

components, for example, the gain update rule used in Eq. (4-18). This function iterates until the objective $|\Delta w| := |\bar{C}_{join} - \bar{C}^{\star}_{join}| < \varepsilon$ has been achieved. It has been visualized in Figure 4-16 that the error used in simulation, i.e. $\varepsilon = 1e\text{-}4$, only requires a single iteration per integration time step while a lower desired error, i.e. $\varepsilon = 1e\text{-}5$, requires at maximum five iterations per time step. Note that coil deployment starts at $t = 5$ seconds. When a lower error ε is desired, other possibly more efficient learning algorithms exist, e.g. golden section search [51].

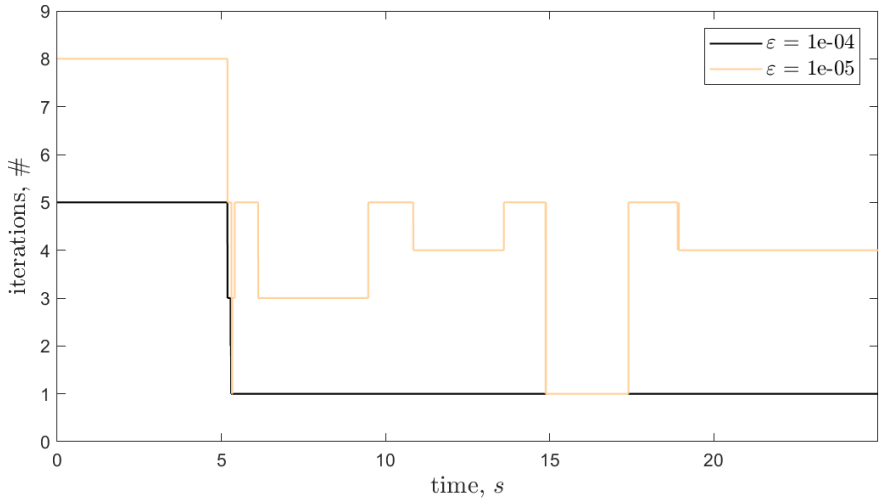

Figure 4-16: Iterations per integration step required to optimize error signal Δw with the learning rule in Eq. (4-18) until the desired error has been reached, i.e. $|\Delta w| := |\bar{C}_{join} - \bar{C}^{\star}_{join}| < \varepsilon$.

Variable	Description	Value	Unit
State parameters			
$w(0)$	Catheter displacement along q_0 at $t = 0$	0	m
$t_c(0)$	Length of coil helix at $t = 0$	0.05	m
$m_c(0)$	Coil mass at $t = 0$	0.08	kg
Coil properties			
r_t	Coil size growth rate	$\frac{1}{6}t_c(0)$	m/s
r_m	Coil mass growth rate	$\frac{1}{6}m_c(0)$	kg/s
β	Base control parameter	0.0116	-
ϵ	Convergence bound around $\bar{C}_{join}(x, w)$	1e-3	m
t_{grow}	Start time of coil growth	5	s
t_{stop}	End time of coil growth	20	s
Other parameters			
h	Integration time step	0.001	s
T	Simulation time	25	s
$F_e^{\star}$	Desired contact force	0.1	N

Table 4-1: Parameter choices for the coil deployment simulation. Parameters introduced in Chapter 3 have been stated Table 3-1.

Chapter 5

Concluding remarks

5-1 Conclusion

Preventive treatment for intracranial aneurysms with endovascular coiling is controversial due to the high risk of complications. These complications are partly caused by the current uncontrolled delivery of coils to the aneurysm. While recent developments in microcatheter design allow for improved positioning, no method has been devised to model and control the tension applied by the coil on the aneurysm wall during a coiling procedure. This thesis has aimed to come up with such a method to improve the safety of aneurysm treatment.

In Chapter 2, a new way has been presented to dynamically model an endovascular coil and its interaction with a microcatheter and the aneurysm wall throughout a coil deployment procedure. The main advantage of this model is its low computational complexity allowing real-time control computation. In Chapter 3 a control architecture has been presented that enables indirect regulation of the contact force between a coil and the aneurysm wall when no extra coil material is added to the system. This control architecture has been extended in Chapter 4 to enable regulation of the contact force between the coil and the aneurysm wall throughout a coil deployment procedure while obeying the constraints imposed by the equipment and the environment. A velocity controller for the catheter's base has been designed that maintains the desired catheter tip position $(x_t^\star, y_t^\star)$ on a derived constraint surface, and thus preserves the feasibility of the contact force regulation objective.

Theoretic proof and numeric simulations have shown that the resulting energy-shaping joint controller asymptotically stabilizes the contact force at the desired reference. This thesis provides a basis for modelling and control in future experimental validations. Therefore, this work is a promising first step in the modelling and control of robotic systems for neurovascular interventions and a step forward in the preventive treatment of intracranial aneurysms.

5-2 Recommendations

While this thesis is a promising first step in the safe treatment of intracranial aneurysms, there is still work to be done to translate the simulations to clinical application. The following paragraphs highlight the main recommendations and topics still to be addressed.

To start with, this thesis has focused its work on the control of tendon-driven steerable microcatheters. The advantage of tendon-driven actuation is its intuitive modelling and control and the fact that a higher bending degree of freedom can be achieved at small scale by separating the tip section into multiple steerable segments [28]. However, up till now, it has been a daunting task to accurately control a tendon-driven manipulator with an incredibly high length-to-diameter ratio, i.e. exceeding 1000:1 [1]. The reason for this is that slack and frictional effects aggregate along the length of the catheter. Alternative actuation mechanisms have been proposed which minimally suffer from said effects. First of two is the pneumatically-driven microcatheter tip developed by the University of California San Diego (UCSD) [1], introduced in the introduction of this thesis. While this actuation mechanism can be easily miniaturized, it will always restrict the steerable microcatheter tip to have a single in-plane bending degree of freedom. As has been shown in this thesis, two degrees of freedom are required to enable accurate in-plane force control. Alternatively, magnetic actuation mechanisms have been proposed by the Massachusetts Institute of Technology (MIT) and the Swiss the Institute of Technology Zürich (ETHZ). The advantage of magnetic steering is that no internal wiring is required, and thus no friction takes place. The design of ETHZ can achieve two-dimensional movement, however does not allow for congruent steering of both tip sections. As has been shown in this thesis, congruent control is required to enable accurate in-plane force control. To conclude, due to the current limitation of other actuation mechanisms, tendon-driven microcatheters remain the most viable option to achieve exact contact force control in intracranial aneurysms. Hence, future research should focus on the design of even smaller tendon-driven catheters which enable decoupled control of two bending sections.

Secondly, this thesis has considered direct control over the tendon torques (τ_1, τ_2) and the base velocity $\dot{w}$. It has been discussed in Section 4-6 that this is a viable assumption for control input $\dot{w}$. However, to actuate tendons, one needs to control the tendon lengths (ℓ_1, ℓ_2) that correspond to the tendon torques (τ_1, τ_2). This map has been omitted in this thesis for the reason that every catheter has different mechanical properties, hence would yield different torques based on tendon displacements. Many studies have focused on finding an accurate map between catheter lengths and tendon torques, e.g. [52], and can easily be incorporated in the presented model.

Regarding coil deployment, this thesis has considered an aneurysm shape that can be perfectly framed with a single helical coil. However, a single coil is never sufficient to fill an aneurysm. The question arises whether the presented strategy would need to be adjusted to enable the deployment of multiple coils. This is not necessarily the case. By adding a helical coil with a smaller diameter within the already deployed helical coil structure, the aneurysm would be filled appropriately. This so-called 'matryoshka' strategy has been adapted in coiling procedures [18]. The most pressing question is how to assure that a coil stays at its desired position after deployment. A theory is that, due to blood clot formation, this coil sticks to the surrounding aneurysm walls and other deployed coils. However, future experiments should verify this statement.

Another note is that this research has considered planar control of a catheter tip to enable contact force control between the coil and the aneurysm wall. This is a valid assumption given that the catheter 1) undergoes minimal torsion, 2) is not subjected to out-of-plane disturbances and 3) its bending plane is equivalent to the plane that contains the vector orthogonal to the wall ($\boldsymbol{n}^{\perp}$) and containing the contact point (x_e, y_e). It has been discussed in Section 2-4 that the bending plane, i.e. the roll of the catheter around vector q_0, can be manually adjusted by the operator to contain the force vector ($\boldsymbol{n}^{\perp}$). This enables in-plane force control. This thesis has deliberately chosen to omit catheter roll in the control architecture as it seemingly would not improve the performance of coil deployment. However, when out-of-plane disturbances are present, additional control over the roll of the catheter could be used to reject these disturbances, and could therefore be part of future work.

While the previous recommendations concern the improvement of the simulation, the most important question is what should be done to validate the proposed control architecture, and thus enable integration in the clinical workflow. For this, future research should focus on devising reliable setups to validate this work. Many works have focused on the robotic actuation of tendon-driven continuum robots [53]. Other works have focused on phantoms for aneurysms [25] or phantoms for blood vessels [54]. Future work should focus on interconnecting these systems and attaining reliable force measurements to verify the mappings proposed in Section 3-2 and the control architecture proposed in Chapter 4. After experiments have verified the model and control architecture presented in this thesis, the road is open for the first clinical implementation of a robotic system for neurovascular interventions.

Appendix A

Algorithms

This appendix presents a pseudo-code routine (Algorithm 1) to control the contact force between an endovascular coil and the aneurysm wall during coil deployment. This routine is based on the control architecture depicted in Figure A-1, as presented in Chapter 4. Operator inputs are the desired force reference $F_e^\star$, the coil deployment time t_{deploy} in seconds and the coil injection rate τ_{in} in m/s. The acquirement of feedback signals by X-ray segmentation and Fibre Bragg Grating sensors is discussed in Appendix B-3.

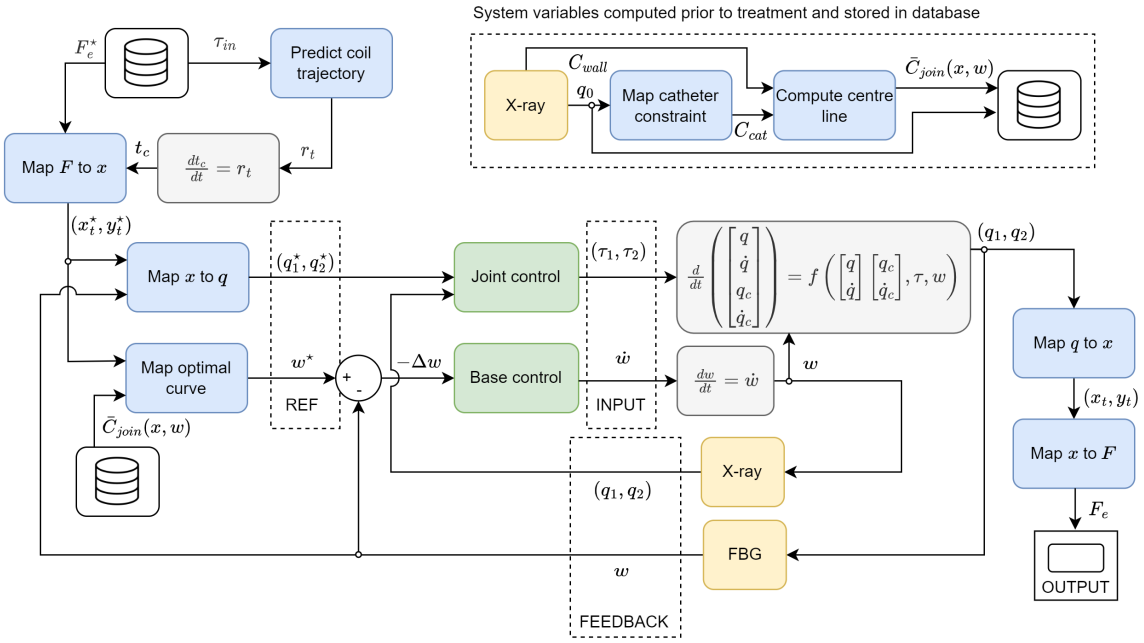

Figure A-1: Control architecture for coil deployment corresponding to Algorithm 1.

Algorithm 1 Controlled coil deployment

function DEPLOY_COIL($C_{cat}, t_{deploy}, \tau_{in}$)
  Input: $F_e^\star$ Desired contact force reference in Newton
    : $\tau_{in} \rightarrow$ Coil injection rate in m/s
    : $t_{deploy} \rightarrow$ Coil deployment duration in seconds
  Measure catheter base angle q_0 and displacement w through angiography
  Measure aneurysm geometry C_{wall} through 3D reconstruction angiography
  Determine contact point (x_e, y_e) from C_{wall}
  Compute catheter task space constraints C_{cat} from q_0 ▷ Eq. (4-6)
  Join catheter constraints C_{cat} with wall constraints C_{wall} ▷ Algorithm 3
  Assert $(x_t^\star, y_t^\star) \in C_{join}$ ▷ Eq. (4-24)
  Compute centre line $\bar{C}_{join}(x, w)$ of C_{join} ▷ Eq. (4-10)
  Compute growth rate of coil's helix length based on τ_{in} ▷ Algorithm 2
  while $t < t_{deploy}$ **do**
    Measure w through real-time fluoroscopy
    Measure (q_1, q_2) through fibre Bragg gratings
    Integrate t_c from r_t ▷ Eq. (4-3)
    Compute $(x_t^\star, y_t^\star)$ from $F_e^\star$ ▷ Eq. (3-9)
    Compute $(q_1^\star, q_2^\star)$ from $(x_t^\star, y_t^\star)$ ▷ Eq. (3-12)
    Update C_{cat} with w
    Update C_{join} from C_{cat} and C_{wall} ▷ Algorithm 3
    Assert $(x_t^\star, y_t^\star) \in C_{join}$ ▷ Eq. (4-24)
    Approximate displacement error Δw ▷ Algorithm 4
    Compute tendon torques τ from $\{(q_1^\star, q_2^\star), (q_1, q_2)\}$ ▷ Eq. (3-18)
    Compute catheter base velocity $\dot{w}$ from Δw ▷ Eq. (4-22)
    Compute F_e from (q_1, q_2) ▷ Eqs. (3-2) and (3-16)
    Output: F_e
  end while
end function

The presented workflow applies several algorithms which have been designed throughout this thesis. Appendix A-1 presents the pseudo-code for the `predict_coil_trajectory`(.) algorithm. This algorithm adapts a geometric coil deployment algorithm from literature to estimate the growth rate (r_t) of the coil's helix length (t_c) based on the coil injection rate (τ_{in}). Appendix A-2 presents the `join_constraints`(.) algorithm which has been proposed in Chapter 4 to efficiently join an arbitrary constraint polygon with a convex constraint polygon to a single constraint space C_{join}. Lastly, Appendix A-3 presents the pseudo-code for the `optimize_deltaw`(.) algorithm which has been shown in Chapter 4 to appriximate the distance Δw between the current centre line of the constraint polygon C_{join}, i.e. $\bar{C}_{join}(x, w)$ and the desired centre line $\bar{C}^\star_{join}(x, w^\star)$ and is used for control of the catheter base.

A-1 Geometric coil deployment modelling

This appendix presents an adjusted version of the geometric coil deployment algorithm proposed by Patel et al. [27]. This algorithm represents an endovascular coil with a number of n_{coil} virtual segments. At each iteration, a new head segment h_i rotates with an angle $\Delta\theta$ according to the preshape of the coil. When a collision with the aneurysm wall is detected, the head segment rotates until a feasible path has been found. Wall vertices $\mathcal{V}$ and their corresponding wall faces $\mathcal{F}$, described as $\mathcal{F}_{i,j}(x,y,z) = a_{i,j}x + b_{i,j}y + c_{i,j}z - d_{i,j} = 0$, can be determined through 3D reconstruction angiography prior to the procedure. To efficiently determine collisions, firstly vertices in $\mathcal{V}$ are detected that lie within a potential colliding distance w_{col} of the coil head segment h_i, that is,

$$\mathcal{V}^f = \{v \in \mathcal{V} | \, ||h_i - v|| < w_{col}\}, \tag{A-1}$$

with $\mathcal{V}^f$ the filtered set of vertices. Wall faces $\mathcal{F}$ are selected corresponding to the filtered vertices in $\mathcal{V}^f$. Then the orthogonal plane distances are computed with respect to the coil's head h_i, that is

$$d_{\mathcal{F}} = \begin{bmatrix} h_i & 1 \end{bmatrix} F_{i,j}. \tag{A-2}$$

If any collision is detected for the real collision distance $d_{col} < w_{col}$, the segment should rotate with $\Delta\theta$. This thesis proposes to adjust Patel's algorithm for helical coil deployment in a saccular aneurysm with a non-constant diameter. The angle φ, i.e. the winding ratio of the coil, is related to the average rate of change of angle θ over the last n_{prev} coil segments, i.e.

$$\varphi = \alpha \frac{1}{n_{prev}} \sum_{k=i-n_{prev}}^{n_{prev}} \Delta\theta_k, \quad \text{if} \quad i > n_{prev}, \tag{A-3}$$

with $\Delta\theta_i := \theta_i - \theta_{i-1}$, α some factor and n_{prev} the number of iterations to average over. At each iteration, the head coil segments then rotates according to,

$$h_i = h_{i-1} + R(\varphi)R(\theta)\overrightarrow{v}, \quad \text{with} \quad v = \begin{bmatrix} \Delta\ell & 0 & 0 \end{bmatrix}, \tag{A-4}$$

with $R(.)$ a counterclockwise rotation matrix and $\overrightarrow{v}$ the coil's direction vector pointing in the positive x-direction with $\Delta\ell$ the length of a single virtual coil segment. This strategy enables realistic geometric modelling of helical endovascular coils in saccular aneurysms. The routine `predict_coil_trajectory`(.) has been depicted in pseudo-code in Algorithm 2. By computation of vector φ, one can derive the growth rate r_t of the coil's helix length through,

$$r_t(t_i) = \sin(\varphi_i)\tau_{in}, \quad \text{with} \quad \tau_{in} = \frac{n_{coil}\Delta\ell}{t_{deploy}}, \tag{A-5}$$

with τ_{in} the coil injection rate in m/s, $r_t(t_i)$ the growth rate of the helical endovascular coil at time t_i in m/s, t_{deploy} the time taken to deploy the coil, $\Delta\ell$ the length of a virtual coil segment. Growth rate $\boldsymbol{r}_t$ is the input to the coil deployment model in Eq. (4-3).

Algorithm 2 Geometric coil deployment algorithm

function PREDICT_COIL_TRAJECTORY($\Delta\theta, h_0, \Delta\ell, n_{coil}, \mathcal{F}, \mathcal{V}, d_{col}, w_{col}, i_{max}$)
  Input : $\Delta\theta \rightarrow$ Coil's helix preshape
  : $h_0 \rightarrow$ Start point of coil deployment
  : n_{coil} Number of virtual coil segments in coil
  : $\Delta\ell \rightarrow$ Virtual coil length
  : $\mathcal{V} \rightarrow$ Aneurysm wall vertices
  : $\mathcal{F} \rightarrow$ Aneurysm wall faces to vertex
  : $d_{col} \rightarrow$ Collision distance
  : $w_{col} \rightarrow$ Potential collision distance
  : $i_{max} \rightarrow$ Maximum number of path search iterations
  Initialize coil direction vector as $\overrightarrow{v} = [\Delta\ell \quad 0 \quad 0]$
  Initialize coil structure with $h = [h_0 \quad h_0 + \overrightarrow{v}]$
  for $i = 2$ **to** the number of virtual coil segments n_{coil} **do**
    Set collision Boolean C_{col} to True
    Initialize iterator k=1
    while Boolean C_{col} is True or iterator k is less than i_{max} **do**
      Increase k with 1
      Compute distance vector $d_{\mathcal{V}}$ between coil head h_i and wall vertices $\mathcal{V}$
      Extract filtered vector $\mathcal{V}^f$ from $\mathcal{V}$ based on $d_{\mathcal{V}} < w_{col}$ ▷ Eq. (A-1)
      if $\mathcal{V}^f$ is empty **then**
        Set collision Boolean C_{col} =False
      end if
      for Vertex v in V_f **do**
        Compute distance vector $d_{\mathcal{F}}$ from h_i to faces around v ▷ Eq. (A-2)
        if Any $d_{\mathcal{F}}$ is smaller than collision distance d_{col} **then**
          Rotate θ with $\Delta\theta$
          Update coil head orientation with θ ▷ Eq. (A-4)
          Set collision Boolean C_{col} to True
          Break the loop
        else
          Set collision Boolean C_{col} to False
        end if
      end for
    end while
    if Iterator k exceeds i_{max} **then**
      Stop deployment simulation as the coil is stuck
    end if
    Rotate θ with $\Delta\theta$
    if i is greater than n_{prev} **then**
      Rotate φ based on the average the last n_{prev} values for θ ▷ Eq. (A-3)
    end if
    Append new head segment to coil structure ▷ Eq. (A-4)
  end for
  Compute the growth rate vector $\boldsymbol{r}_t$ along the coil's helix length ▷ Eq. (A-5)
  return $\boldsymbol{r}_t$
end function

A-2 Constraint joining

This appendix presents the routine `join_constraints`(.) to efficiently join an arbitrary constraint polygon with a convex constraint polygon. The routine iteratively computes the intersection of the non-convex constraint polygon with an edge from the convex polygon. The joining routine with a single edge has been described in Section 4-2-2. The full routine has been depicted in pseudo-code in Algorithm 3. In this thesis, this routine is used to compute the intersection C_{join} of the aneurysm wall C_{wall}, i.e. a convex polygon consisting of the vertices of a saccular, i.e. sac-like shaped, aneurysm, with the non-convex catheter constraints C_{cat}. The joined space C_{join} is used to evaluate whether $(x_t^\star, y_t^\star)$ is a feasible target for the joint controller presented in Chapter 3. The routine `join_constraints`(.) has also been used in simulation to map the 2D helical coil structure within the aneurysm walls.

Algorithm 3 Joining algorithm convex and non-convex polygon

function JOIN_CONSTRAINTS(C_{convex}, C_{in})
  Input : $C_{convex} \rightarrow$ Vertices of convex constraint polygon
    : $C_{in} \rightarrow$ Vertices of arbitrary constraint polygon
  Extract vertices $\{\boldsymbol{x_p}, \boldsymbol{y_p}\}$ from C_{in}
  for Edge $\mathcal{E}$ in C_{convex} **do**
    Extract coordinates $\{x_1, x_2, y_1, y_2\}$ from edge $\mathcal{E}$
    Compute the unit vector $\boldsymbol{n}$ orthogonal to edge $\mathcal{E}$
    Compute the distance vector d from $\{\boldsymbol{x_p}, \boldsymbol{y_p}\}$ to edge $\mathcal{E}$ ▷ Eq. (4-7)
    Extract indices i_d for which vector d changes sign
    if i_d is empty **then** ▷ i_d is either empty or $\mathbb{R}^2$
      return C_{in}
    else
      Compute intersection points p_c with edge $\mathcal{E}$ ▷ Eq. (4-8)
      Update C_{in} with p_c ▷ Eq. (4-9)
      return C_{in}
    end if
  end for
end function

A-3 Optimization of Δw

This appendix presents the routine `optimize_deltaw(.)` to efficiently compute the offset between the current centre line $\bar{C}_{join}(x, w)$ of the constraint polygon C_{join} and the desired centre line $\bar{C}^{\star}_{join}(x, w^{\star}$ that contains the desired tip reference position $(x_t^{\star}, y_t^{\star})$. It has been argued in Section 4-3 that bringing Δw close to zero maximizes the feasibility of $(x_t^{\star}, y_t^{\star})$. The single approximation of Δw has been described throughout Section 4-3-1. The optimization objective is to find a gain α such that $\Delta w = \alpha \Delta w_0$ with Δw_0 and initial guess on vector Δw. The routine for a single approximation has been depicted in pseudo-code in Algorithm 4. This approximation is updated according to Algorithm 1.

Algorithm 4 Offset computation from $\bar{C}_{join}$ to $\bar{C}^{\star}_{join}$

function OPTIMIZE_DELTAW($\bar{C}_{join}(x, w), (x_t^{\star}, y_t^{\star}), q_0, w$)
  Input : $(x_t^{\star}, y_t^{\star}) \rightarrow$ Reference position for catheter tip
    : $q_0 \rightarrow$ Constant direction of catheter base
    : w Displacement of catheter base along q_0
    : $\bar{C}_{join}(x, w) \rightarrow$ Centre line of constraint space C_{join} computed for $w = w(0)$
  Make initial guess of vector pointing from $(x_t^{\star}, y_t^{\star})$ to $\bar{C}_{join}(x, w)$ along q_0 ▷ Eq. (4-16)
  Make initial guess of the point (x_w, y_w) on $\bar{C}_{join}(x, w)$ ▷ Eq. (4-17)
  Compute the error e_y from (x_w, y_w) to $\bar{C}_{join}(x, w)$ ▷ Eq. (4-15)
  Initialize iterator i at 1
  Initialize gain α_0 at 1
  Initialize update factor for α at $\frac{1}{2}$
  while Error $|e_y| > \varepsilon$ and iterator $i < i_{max}$ **do**
    Update gain $\alpha_i = \alpha_{i-1} + \text{ sign}\,(e_y \Delta w_0)\,\delta$ ▷ Eqs. (4-18) and (4-19)
    Increase iterator i with 1
    Divide factor δ with 2
    Update guess on $(x_w, y_w) = \alpha \Delta w_0 + (x_t^{\star}, y_t^{\star})$ ▷ Eq. (4-16)
    Update error e_y based on (x_w, y_w) ▷ Eq. (4-15)
  end while
  Compute Δw from (x_w, y_w) and $(x_t^{\star}, y_t^{\star})$ ▷ Eq. (4-20)
  return Δw
end function

Appendix B

Complementary material

The appendix provides complementary material. Appendix B-1 provides the notions of Lyapunov stability and LaSalle's invariance principle which are used in the stability analysis of the designed controllers in Chapters 3 and 4. Appendix B-2 gives an introduction in passivity and passivity based control for controller design in Chapter 3. Appendix B-3 gives an overview of sensing methods to retrieve feedback signals for the control architectures in Figures 3-3 and 4-7.

B-1 Stability

This appendix follows the work by Khalil et al. [55] to provide notions of Lyapunov stability and LaSalle's invariance principle. Consider the autonomous system

$$\dot{x} = f(x), \tag{B-1}$$

where f is a locally Lipschitz function defined over a domain $D \subset \mathbb{R}^n$. Suppose $f(\bar{x})$ to be an equilibrium point of $f(x)$, i.e. $f(\bar{x}) = 0$. This equilibrium points is assumed to be placed at the origin, i.e. $\bar{x} = 0$. This is without loss of generality because any equilibrium point can be shifted to the origin via a change of variables, i.e. $y = x - \bar{x}$, such that

$$\dot{y} = \dot{x} = f(y + \bar{x}) = g(y), \text{ with } g(0) = 0. \tag{B-2}$$

An equilibrium point is stable if all solutions starting at nearby points stay nearby. Otherwise it is unstable. It is asymptotically stable if all solutions starting at nearby points not only stay nearby but also tend to the equilibrium point as time approaches infinity.

B-1-1 Lyapunov stability

Lyapunov showed that certain functions, named Lyapunov functions, could be used to determine the stability of an equilibrium. Let such a function, i.e. $V(x)$, be a continuously

differentiable real-valued function defined in a domain $D \subset \mathbb{R}^n$ that contains the origin. The derivative of $V(x)$ along the trajectories of $\dot{x} = f(x)$ is given given by

$$\frac{\partial V(x)}{\partial x} f(x). \tag{B-3}$$

If $\dot{V}(x)$ is negative, $V(x)$ will decrease along the solution of $\dot{x} = f(x)$. This observation leads to Lyapunovs stability theorem:

Theorem B.1 *Consider the locally Lipchitz function in Eq.* (B-1) *defined over a domain* $D \subset \mathbb{R}^n$ *which contains the origin and* $f(0) = 0$. *If a continuous differentiable function can be defined such that*

$$\begin{aligned} V(0) = 0 \quad V(x) > 0 \text{ for } x \neq 0 \text{ and } x \in D, \\ \dot{V}(x) \leq 0 \text{ for all } x \in D, \end{aligned} \tag{B-4}$$

then the system $f(x)$ *is stable around the origin. If* $\dot{V}(x)$ *is only zero for* $x = 0$ *we have asymptotic stability. If the function* $V(x)$ *is radially unbounded, i.e.*

$$|x| \to \infty \implies V(x) \to \infty, \tag{B-5}$$

and $D = \mathbb{R}^n$, *we have global asymptotic stability of the origin.*

There is no systematic method for finding Lyapunov functions, however, in mechanical systems Lyapunov candidates may resemble energy functions. A classic radially unbounded Lyapunov function is

$$V(x) = x^T P x, \text{ with } P > 0. \tag{B-6}$$

B-1-2 LaSalle's invariance principle

In some cases, a Lyapunov function is chosen whose derivative $\dot{V}(x)$ along the trajectories of the system is negative semidefinite, i.e. $\dot{V}(x)$. If it can be established that no trajectory can stay identically at points where $\dot{V}(x)$ =0, except at the origin, then the origin is asymptotically stable. This idea follows from LaSalle's invariance principle:

Theorem B.2 *Consider the locally Lipchitz function* $f(x)$ *in Eq.* (B-1) *defined over a domain* $D \subset \mathbb{R}^n$ *which contains the origin and* $f(0) = 0$. *Let* $V(x)$ *be a continuously differentiable positive definite function defined over* D *such that* $\dot{V}(x) \leq 0$ *in* D. *Let* $S = \{x \in D | \dot{V}(x) = 0\}$ *and suppose that no solution can stay identically in* S, *other than the trivial solution* $x(t) = 0$. *Then the origin is an asymptotically stable equilibrium point of* $\dot{x} = f(x)$. *Finally, if* $D = \mathbb{R}^n$ *and* $V(x)$ *is radially unbounded, then the origin is globally asymptotically stable.*

Note that a set a set M is positively invariant when a solution belongs to M at some time instant, then it belongs to M for all future time. Both equilibrium points and limit sets are invariant sets.

B-2 Passivity-based control

This appendix gives a short introduction of the notions of passivity and passivity-based control, following the work of Ortega et al. [31]. In passive systems the rate at which the energy flows into the system is not less than the increase in storage. In other words, a passive system cannot store more energy than is supplied to it from the outside, with the difference being the dissipated energy, i.e.

$$\underbrace{H(t)}_{available} = \underbrace{H(0)}_{initial} + \underbrace{\int_0^t u(\tau)y(\tau)d\tau}_{supplied} - \underbrace{\int_0^t F(\dot{q}(\tau))d\tau}_{dissipated}, \tag{B-7}$$

where $H := V + T$ is the total energy or storage function of the system, uy is the power delivered from an external source and $F(\dot{q})$ is a dissipative function. Euler Lagrange systems define passive maps with a storage function defined as their total energy. In recent years passivity, and more specifically feedback passivation, has been used to reformulate the fundamental problem of feedback stabilization of nonlinear systems. A specific passivity-based control action is energy-shaping plus damping injection technique introduced to solve state-feedback set point regulation problems in fully actuated robotic systems by Takegaki and Arimoto [41]. The design comprises an energy shaping stage where the potential energy of the system is modified in such a way that the "new" potential energy function has a global and unique minimum in the desired equilibrium and a damping injection stage where the dissipation function is modified to ensure asymptotic stability. This follows from the following theorem:

Theorem B.3 *Consider an n-degrees of freedom fully-actuated EL system with no internal damping nor external forces described by*

$$D(q)\ddot{q} + C(q,\dot{q})\dot{q} + g(q) = Mu, \tag{B-8}$$

where $q \in \mathbb{R}^n$ is the state vector and $u \in \mathbb{R}^m$ the vector of control inputs, $D(q)$ the inertial matrix, $C(q,\dot{q})$ denoting the Coriolis forces of the system and $g(q)$ denoting the gravity of the system. Let the state-feedback law be given as

$$u = \frac{\partial V_c}{\partial q}(q) - \frac{\partial F_c}{\partial \dot{q}}(\dot{q}), \tag{B-9}$$

where the function $V_c(q)$ is such that the potential energy of the closed-loop system.

$$V_d(q) := V(q) + V_c(q), \tag{B-10}$$

has a unique global minimum at $q = \bar{q}$ and is radially unbounded, as defined in Eq. (B-5)*, with respect to $\tilde{q} := q - \bar{q}$. The dissipation function $F_c(\dot{q})$ satisfies*

$$\frac{\partial F_c}{\partial \dot{q}}(0) = 0 \quad \text{and } \dot{q}^T \frac{\partial F_c}{\partial \dot{q}}(\dot{q}) > 0,\ \forall \dot{q} \neq 0. \tag{B-11}$$

Under these conditions, the equilibrium $(q,\dot{q})^T$ is globally asymptotically stable.

Note that when the system is already full internally damped, we do not necessarily need a derivative action. However, an additional damper can be useful to reduce the overshoot of the system.

B-3 Sensing methods

The steerable microcatheter tip model, as derived in Section 2-1, requires feedback on the catheter's configuration and the environment's geometry to reliably employ a control strategy. Reconstruction of the aneurysm geometry is commonly done prior to treatment using rotational angiography [43]. This 3D angiogram, shown in Figure B-1a, serves as the workspace for the catheter and gives information on coil selection [18]. As has been discussed in Section 1-1-2, the steerable catheter tip can be visualized using X-ray guidance (Figure B-1c). The disadvantage of this imaging technique is that the catheter tip becomes harder to visualize when the procedure advances as it cannot be distinguished from the radio-opaque coils. The base of the steerable tip, however, often remains outside of the aneurysm sac, and thus can be sensed throughout the procedure. This thesis proposes to integrate Fibre Bragg Grating (FBG) sensors in the shaft of the steerable catheter tip to reconstruct the shape of the catheter when invisible on X-ray. A fibre Bragg grating, illustrated in Figure B-1b, experiences strain when the catheter is bent. Reflected light signals, originating from a periodic pattern of external laser light, combine coherently into one large reflection at a particular wavelength. This wavelength is used to determine the strain or curvature of the FBG. The FBG sensors are a viable choice because they are highly sensitive to strain, can easily be miniaturized to a diameter of 0.15mm and have previously been used in medical equipment [32, 56, 57]. Placing an FBG sensor at every virtual joint of the pseudo-rigid body model is sufficient to retrieve the shape, hence tip position, of the steerable catheter tip.

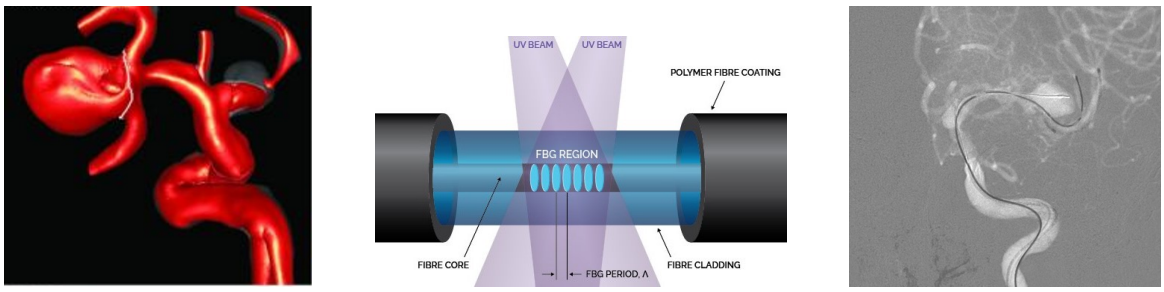

(a) 3D reconstruction of intracranial aneurysm [43].

(b) Fibre Bragg grating sensor [56].

(c) Catheter visible on X-ray guidance [5].

Figure B-1: Medical sensing methods of the catheter and intracranial aneurysm shape.

Bibliography

[1] T. Gopesh, J. H. Wen, D. Santiago-Dieppa, B. Yan, J. S. Pannell, A. Khalessi, A. Norbash, and J. Friend, "Soft robotic steerable microcatheter for the endovascular treatment of cerebral disorders," *Science Robotics*, vol. 6, 8 2021.

[2] B. G. Thompson, R. D. Brown, S. Amin-Hanjani, J. P. Broderick, K. M. Cockroft, E. S. Connolly, G. R. Duckwiler, C. C. Harris, V. J. Howard, S. C. C. Johnston, P. M. Meyers, A. Molyneux, C. S. Ogilvy, A. J. Ringer, J. Torner, American Heart Association Stroke Council, Council on Cardiovascular and Stroke Nursing, Council on Epidemiology and Prevention, American Heart Association, and American Stroke Association, "Guidelines for the management of patients with unruptured intracranial aneurysms: A guideline for healthcare professionals from the american heart association/american stroke association.," *Stroke*, vol. 46, pp. 2368–400, 8 2015.

[3] X. Huang, G. Yan, Z. Qin, and G. Zhu, "To clip or to coil for unruptured intracranial aneurysm?: A protocol of randomized controlled trial.," *Medicine*, vol. 100, p. e24692, 3 2021.

[4] Medical Advisory Secretariat, "Coil embolization for intracranial aneurysms: an evidence-based analysis.," *Ontario health technology assessment series*, vol. 6, pp. 1–114, 2006.

[5] C. B. Luo, F. C. Chang, C. J. Lin, and W. Y. Guo, "A coil placement technique to treat intracranial aneurysm with incorporated artery," *Journal of the Chinese Medical Association*, vol. 81, pp. 255–261, 3 2018.

[6] Radboud University Medical Centre, "Wat is een hersenaneurysma?." https://www.radboudumc.nl/patientenzorg/aandoeningen/aneurysma-in-de-hersenen/wat-is-een-hersenaneurysma, 2022.

[7] Wikipedia, "Intracranial aneurysm." https://en.wikipedia.org/wiki/Intracranial_aneurysm, 2022.

[8] A. Ringer and R. Tackla, "Aneurysm clipping | Cincinnati, Ohio Mayfield Brain & Spine." https://mayfieldclinic.com/pe-clipping.htm, 2021.

[9] Antwerp University Hospital, "Bijcoiling van een hersenaneurysma." https://www.uza.be/behandeling/bijcoiling-van-een-hersenaneurysma, 2022.

[10] M. T. Lawton and G. E. Vates, "Subarachnoid hemorrhage," *New England Journal of Medicine*, vol. 377, pp. 257–266, 7 2017.

[11] J. Hu, H. Albadawi, B. W. Chong, A. R. Deipolyi, R. A. Sheth, A. Khademhosseini, and R. Oklu, "Advances in biomaterials and technologies for vascular embolization," *Advanced Materials*, vol. 31, p. 1901071, 8 2019.

[12] A. Ringer and R. Tackla, "Aneurysm coiling, stenting & flow diversion | Mayfield Brain & Spine Cincinnati, Ohio." https://mayfieldclinic.com/pe-coiling.htm, 2021.

[13] D. O. Wiebers, "Unruptured intracranial aneurysms: natural history, clinical outcome, and risks of surgical and endovascular treatment," *The Lancet*, vol. 362, pp. 103–110, 7 2003.

[14] R. R. Slazas, "Embolic coil delivery system with mechanical release mechanism, us7901444b2," 9 2011.

[15] C. S. Eddleman, B. G. Welch, A. Z. Vance, K. L. Rickert, J. A. White, G. L. Pride, and P. D. Purdy, "Endovascular coils: properties, technical complications and salvage techniques," *Journal of NeuroInterventional Surgery*, vol. 5, pp. 104–109, 3 2013.

[16] J. White, C. Ken, H. Cloft, and D. Kallmes, "Coils in a nutshell: A review of coil physical properties," *American Journal of Neuroradiology*, vol. 29, pp. 1242–1246, 8 2008.

[17] S. M. M. J. Sarayi, R. J. Damiano, P. Patel, G. Dargush, A. H. Siddiqui, and H. Meng, "A nonlinear mechanics-based virtual coiling method for intracranial aneurysm," 9 2020.

[18] A. M. Spiotta, R. D. Turner, M. I. Chaudry, and A. S. Turk, *Management of Cerebrovascular Disorders*. Springer International Publishing, 2019.

[19] Y. Kim, E. Genevriere, P. Harker, J. Choe, M. Balicki, R. W. Regenhardt, J. E. Vranic, A. A. Dmytriw, A. B. Patel, and X. Zhao, "Telerobotic neurovascular interventions with magnetic manipulation," *Science Robotics*, vol. 7, 4 2022.

[20] J. Friend and G. Tilvawala, "This bioinspired steerable catheter for brain surgery is the first of its kind - UC San Diego | YouTube." https://www.youtube.com/watch?v=TDOH3KO_-94, 2021.

[21] F. G. de Barros Pontes, V. Vasconcelos, J. C. Baptista-Silva, and E. M. da Silva, "Treatments for unruptured intracranial aneurysms," *Cochrane Database of Systematic Reviews*, 4 2019.

[22] Y. K. Ihn, S. H. Shin, S. K. Baik, and I. S. Choi, "Complications of endovascular treatment for intracranial aneurysms: Management and prevention.," *Interventional neuroradiology : journal of peritherapeutic neuroradiology, surgical procedures and related neurosciences*, vol. 24, pp. 237–245, 6 2018.

[23] Y. K. Park, H.-J. Yi, K.-S. Choi, Y.-J. Lee, and H.-J. Chun, "Intraprocedural rupture during endovascular treatment of intracranial aneurysm: Clinical results and literature review," *World Neurosurgery*, vol. 114, pp. e605–e615, 6 2018.

[24] E. Orrù, L. Roccatagliata, G. Cester, F. Causin, and L. Castellan, "Complications of endovascular treatment of cerebral aneurysms," *European Journal of Radiology*, vol. 82, pp. 1653–1658, 10 2013.

[25] T. Oishi, K. Takashima, K. Yoshinaka, K. Yu, M. Ohta, K. Mori, and N. Toma, "Evaluation of effect of aneurysm model material on coil contact force and catheter movement," *Journal of Biomechanical Science and Engineering*, vol. 17, pp. 21–00261, 2022.

[26] M. H. Babiker, B. Chong, L. F. Gonzalez, S. Cheema, and D. H. Frakes, "Finite element modeling of embolic coil deployment: Multifactor characterization of treatment effects on cerebral aneurysm hemodynamics," *Journal of Biomechanics*, vol. 46, pp. 2809–2816, 11 2013.

[27] P. Patel, S. M. M. J. Sarayi, D. Chen, A. L. Hammond, R. J. Damiano, J. M. Davies, J. Xu, and H. Meng, "Fast virtual coiling algorithm for intracranial aneurysms using pre-shape path planning," *Computers in Biology and Medicine*, vol. 134, p. 104496, 7 2021.

[28] P. Rao, Q. Peyron, S. Lilge, and J. Burgner-Kahrs, "How to model tendon-driven continuum robots and benchmark modelling performance," *Frontiers in Robotics and AI*, vol. 7, 2 2021.

[29] C. D. Santina, C. Duriez, D. R. POC, and C. D. Santina, "Model based control of soft robots: A survey of the state of the art and open challenges," 2021.

[30] M. T. Chikhaoui and J. Burgner-Kahrs, "Control of continuum robots for medical applications: State of the art," ACTUATOR 2018; 16th International Conference on New Actuators, 2018.

[31] R. Ortega and A. Loria, *Passivity-based Control of Euler-Lagrange Systems*. Springer, 1998.

[32] P. Dupont, N. Simaan, H. Choset, and C. Rucker, "Continuum robots for medical interventions," *Proceedings of the IEEE*, pp. 1–24, 2022.

[33] J. Burgner-Kahrs, D. C. Rucker, and H. Choset, "Continuum robots for medical applications: A survey," *IEEE Transactions on Robotics*, vol. 31, pp. 1261–1280, 12 2015.

[34] P. Berthet-Rayne, K. Leibrandt, K. Kim, C. A. Seneci, J. Shang, and G. Z. Yang, "Rolling-joint design optimization for tendon driven snake-like surgical robots," *IEEE International Conference on Intelligent Robots and Systems*, pp. 4964–4971, 12 2018.

[35] X. Hu, A. Chen, Y. Luo, C. Zhang, and E. Zhang, "Steerable catheters for minimally invasive surgery: a review and future directions," *Computer Assisted Surgery*, vol. 23, pp. 21–41, 1 2018.

[36] T. G. Thuruthel, Y. Ansari, E. Falotico, and C. Laschi, "Control strategies for soft robotic manipulators: A survey," *Soft Robotics*, vol. 5, pp. 149–163, 4 2018.

[37] H. J. Su, "A pseudorigid-body 3r model for determining large deflection of cantilever beams subject to tip loads," *Journal of Mechanisms and Robotics*, vol. 1, pp. 1–9, 5 2009.

[38] S. Huang, D. Meng, X. Wang, B. Liang, and W. Lu, "A 3d static modeling method and experimental verification of continuum robots based on pseudo-rigid body theory," *IEEE International Conference on Intelligent Robots and Systems*, pp. 4672–4677, 11 2019.

[39] H. Vallery and A. L. Schwab, *Advanced dynamics, Delft University of Technology*. 3rd ed., 2017.

[40] C. D. Santina, R. K. Katzschmann, A. Biechi, and D. Rus, "Dynamic control of soft robots interacting with the environment," pp. 46–53, IEEE, 4 2018.

[41] R. Kelly, "Pd control with desired gravity compensation of robotic manipulators: A review," 1997.

[42] E. Corral, R. G. Moreno, M. J. G. García, and C. Castejón, "Nonlinear phenomena of contact in multibody systems dynamics: a review," *Nonlinear Dynamics*, vol. 104, pp. 1269–1295, 4 2021.

[43] J. Cebral, X. Duan, B. Chung, C. Putman, K. Aziz, and A. Robertson, "Wall mechanical properties and hemodynamics of unruptured intracranial aneurysms," *American Journal of Neuroradiology*, vol. 36, pp. 1695–1703, 9 2015.

[44] A. Kolipaka, V. S. P. Illapani, W. Kenyhercz, J. D. Dowell, M. R. Go, J. E. Starr, P. S. Vaccaro, and R. D. White, "Quantification of abdominal aortic aneurysm stiffness using magnetic resonance elastography and its comparison to aneurysm diameter," *Journal of Vascular Surgery*, vol. 64, pp. 966–974, 10 2016.

[45] C. Ott, *cartesian impedance control of redundant and flexible-joint robots*. 2008.

[46] A. Bajo and N. Simaan, "Hybrid motion/force control of multi-backbone continuum robots," *The International Journal of Robotics Research*, vol. 35, pp. 422–434, 4 2016.

[47] S. Chiaverini, B. Siciliano, and L. Villani, "Force/position regulation of compliant robot manipulators," *IEEE Transactions on Automatic Control*, vol. 39, pp. 647–652, 3 1994.

[48] P. Corke, "Inverse kinematics for a 2-joint robot arm using geometry | robot academy." https://robotacademy.net.au/lesson/inverse-kinematics-for-a-2-joint-robot-arm-using-geometry/, 2019.

[49] G. Gerboni, P. W. J. Henselmans, E. A. Arkenbout, W. R. van Furth, and P. Breedveld, "Helixflex : bioinspired maneuverable instrument for skull base surgery," *Bioinspiration & Biomimetics*, vol. 10, p. 066013, 12 2015.

[50] N. Kapoor and J. Ohri, "Integrating a few actions for chattering reduction and error convergence in sliding mode controller in robotic manipulator," 2013.

[51] J. Kiefer, "Sequential minimax search for a maximum," *Proceedings of the American Mathematical Society*, vol. 4, p. 502, 6 1953.

[52] M. Khoshnam and R. V. Patel, "Robotics-assisted control of steerable ablation catheters based on the analysis of tendon-sheath transmission mechanisms," *IEEE/ASME Transactions on Mechatronics*, vol. 22, pp. 1473–1484, 6 2017.

[53] J. Back, L. Lindenroth, K. Rhode, and H. Liu, "Three dimensional force estimation for steerable catheters through bi-point tracking," *Sensors and Actuators A: Physical*, vol. 279, pp. 404–415, 8 2018.

[54] C. Chautems, A. Tonazzini, D. Floreano, and B. J. Nelson, "A variable stiffness catheter controlled with an external magnetic field," pp. 181–186, IEEE, 9 2017.

[55] H. Khalil, *Nonlinear control*, vol. 406. Pearson, global edition ed., 2015.

[56] Smart-Fibres, "Fbg technology description." https://www.smartfibres.com/technology, 2022.

[57] FBGS, "Fbg principle." https://fbgs.com/technology/fbg-principle/, 2022.

Glossary

List of Acronyms

SAH	Subarachnoid Haemorrhage
IA	Intracranial Aneurysm
UIA	Unruptured Intracranial Aneurysms
IAR	Intraprocedural Aneurysm Rupture
TE	Thromboembolic Event
PRB	Pseudo-rigid Body
CoM	Centre of Mass
FBG	Fibre Bragg Grating
UCSD	University of California San Diego
Erasmus MC	Erasmus University Medical Center
MIT	Massachusetts Institute of Technology